# Dealloying Induced Stress Corrosion Cracking

by

Shaofeng Sun

A Dissertation Presented in Partial Fulfillment
of the Requirements for the Degree
Doctor of Philosophy

Approved November 2012 by the
Graduate Supervisory Committee:

Karl Sieradzki Chair
Hanqing Jiang
Pedro Peralta

ARIZONA STATE UNIVERSITY

December 2012

ABSTRACT

Dealloying induced stress corrosion cracking is particularly relevant in energy conversion systems (both nuclear and fossil fuel) as many failures in alloys such as austenitic stainless steel and nickel-based systems result directly from dealloying. This study provides evidence of the role of unstable dynamic fracture processes in dealloying induced stress-corrosion cracking of face-centered cubic alloys. Corrosion of such alloys often results in the formation of a brittle nanoporous layer which we hypothesize serves to nucleate a crack that owing to dynamic effects penetrates into the un-dealloyed parent phase alloy. Thus, since there is essentially a purely mechanical component of cracking, stress corrosion crack propagation rates can be significantly larger than that predicted from electrochemical parameters. The main objective of this work is to examine and test this hypothesis under conditions relevant to stress corrosion cracking.

Silver-gold alloys serve as a model system for this study since hydrogen effects can be neglected on a thermodynamic basis, which allows us to focus on a single cracking mechanism. In order to study various aspects of this problem, the dynamic fracture properties of monolithic nanoporous gold (NPG) were examined in air and under electrochemical conditions relevant to stress corrosion cracking. The detailed processes associated with the crack injection phenomenon were also examined by forming dealloyed nanoporous layers of prescribed

properties on un-dealloyed parent phase structures and measuring crack penetration distances.

Dynamic fracture in monolithic NPG and in crack injection experiments was examined using high-speed ($10^6$ frames $s^{-1}$) digital photography. The tunable set of experimental parameters included the NPG length scale (20-40 nm), thickness of the dealloyed layer (10-3000 nm) and the electrochemical potential (0.5-1.5 V). The results of crack injection experiments were characterized using the dual-beam focused ion beam/scanning electron microscopy. Together these tools allow us to very accurately examine the detailed structure and composition of dealloyed grain boundaries and compare crack injection distances to the depth of dealloying.

The results of this work should provide a basis for new mathematical modeling of dealloying induced stress corrosion cracking while providing a sound physical basis for the design of new alloys that may not be susceptible to this form of cracking. Additionally, the obtained results should be of broad interest to researchers interested in the fracture properties of nano-structured materials. The findings will open up new avenues of research apart from any implications the study may have for stress corrosion cracking.

ACKNOWLEDGEMENTS

I would like to particularly thank Professor Karl Sieradzki, my supervisor, for his guidance and inspiration on my research. His patience and great efforts to lead me into the scientific world are highly appreciated. I wish to thank Dr. Steven Klein, my collaborator and friend, who has offered invaluable help with the high speed digital camera. I also would like to thank Dr Newman Roger and his student, Nick Senior for their discussion and suggestions of this work. I greatly appreciate Dr Lei Tang for her friendship and guidance of electrochemistry.

I am grateful to Dr Zhengquan Liu for his detailed training in SEM. Tam Gordon and Grant.Baumgardner's advice and help on operating FIB machine is deeply acknowledged. Their help has greatly improved my skills. I need to thank James Maker from the mechanical machine shop for the great help in instrument design and sample machining. I also want to thank my lovely and helpful lab mates, Xiaoqian Li, Qing Chen and Nelish Badwe. With their company, my research life is more enjoyable. I am indebted to Dr. Fritz Friedersdorf for his previous work on stress corrosion cracking of binary noble alloys. His research gave me a lot of instructions. Finally, I would like to thank my husband and parents for their support and encouragement in this journey.

TABLE OF CONTENTS

Page

CHAPTER Page

LIST OF TABLES

Table Page

LIST OF FIGURES

Figure Page

Figure Page

Figure Page

Figure Page

Figure Page

# Chapter 1

# INTRODUCTION AND BACKGROUND

## 1.1 Basic theory of Dealloying

Dealloying is an electrochemical corrosion process during which one or several elements are selectively dissolved from an alloy at rates based on their electrochemical activity. It can result in the formation of a nanoporous structure which is mainly composed of the more-noble alloy components. A prototypical dealloyed porous structure is shown in Figure 1.1. The dealloying phenomenon has a long history of being used by early goldsmiths to enhance surfaces of their artifacts (*1*). Today, dealloying is primarily studied as a corrosion process. It is believed to play an important role in various forms of stress corrosion cracking and corrosion fatigue in different alloy systems, like brasses (*2*) and stainless steel (*3*).

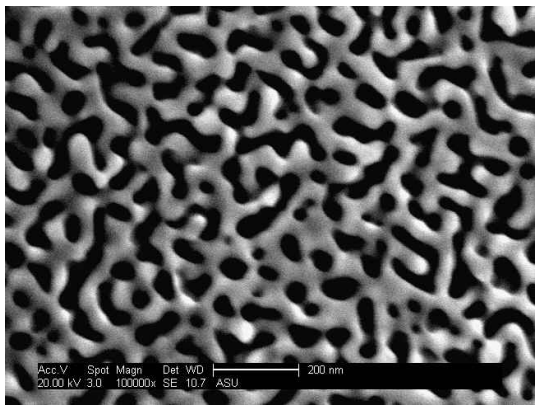


Figure 1.1 NPG formed through selective dissolution of $Ag_{67}Au_{33}$ in concentrated nitric acid for 30 minutes and annealed at 300ºC for 10 minutes.

Since dealloying is an electrochemical process, the study of alloy polarization behavior is one of the key tools for understanding it. A general overview of the alloy polarization behavior of binary alloys was first proposed by Pickering (*4*) . He noted that a passive-like behavior exists for certain binary alloy systems, $A_pB_{1-p}$, where A is the more active component and p is the atomic composition of the A element(s). The characteristic behavior of these alloys illustrated by Pickering is shown in Figure 1.2. In this figure, curve (4) represents the electrochemical behavior of elemental metal A; Curve (3b) shows the dissolution of element B. Curve (1) (2) (3a) represent behavior of alloys with different B compositions showing different an "a" region (a limited current region), which is suppressed by a surface layer of more noble metal B. Above a specific potential, defined as the critical potential, $E_c$, the polarization behavior transitions from a to b and the rate of dissolution of A increased sharply with the concomitant formation of porosity. This critical potential marks the onset of bulk dealloying. Dealloying regions of a and b are referred as Type I and that containing regions of a and c referred to Type II. When the content of B increases or the dealloying overpotential difference between A and B decreases, type II dissolution is more likely to occur. The maximum content of B at which dealloying occurs, NB*, is called the dealloying threshold and is expected for all binary alloy systems that follow Type I dissolution.

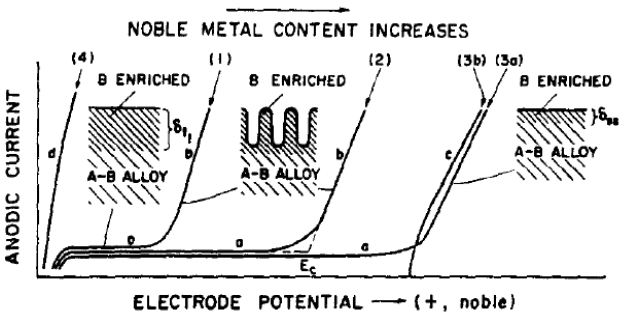


Figure 1.2. Schematic illustration of polarization behavior of binary A-B alloys (*4*)

The dealloying threshold and critical potential are two of the most important factors needed to be addressed for a general theory of dealloying and porosity formation. Binary alloys that exhibit continuous solid solubility, such as Ag-Au alloys or Cu-Au alloys, are model systems for studying these behaviors. This is because Au is relatively stable in most electrolytes and the electrochemical dissolution current density only corresponds to the Ag or Cu dissolution flux from the alloy surface and bulk. The phase diagrams for Ag-Au alloys and Cu-Au alloys are shown in Figure 1.3 and 1.4.

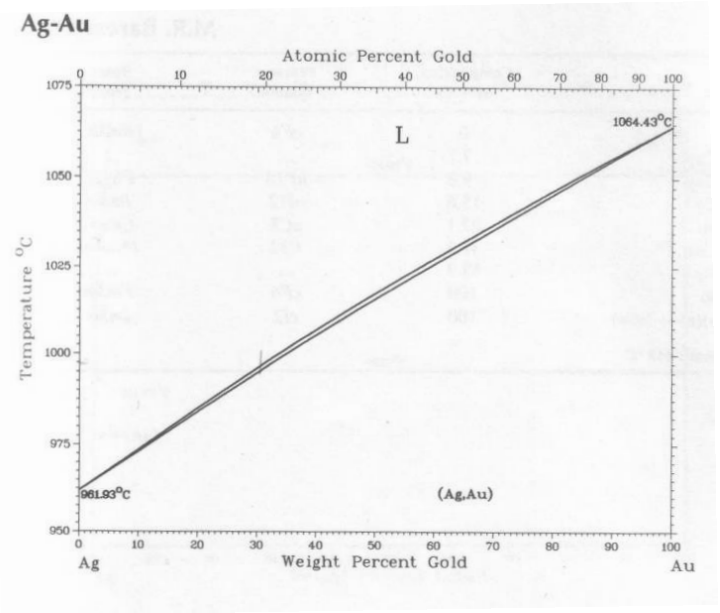


Figure 1.3. Phase diagram of Ag-Au, showing complete solid solubility between silver and gold above 900°C (*5*)

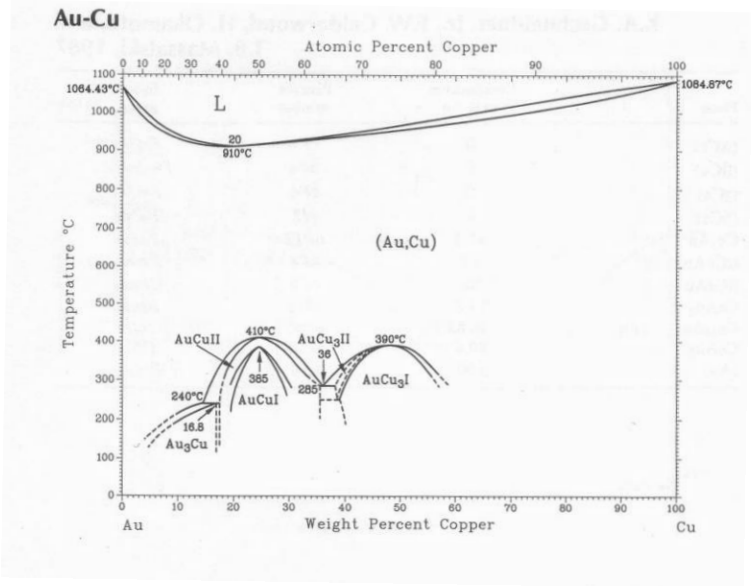


Figure 1.4 Phase diagram of Cu-Au, showing ordered phases that form in the solid state: AuCu, $Au_3Cu$ and $AuCu_3$ (*5*)

Dealloying is believed to involve the notion of percolation (*6–8*). Consider an alloy $A_pB_{1-p}$, where A is the more active component. Sieradzki and Newman (*8*) claimed that for selective dissolution to occur, there should be continuous connected pathways of element A throughout the structure of the solid. This pathway would provide continuous dissolution of element A and penetration of electrolyte into the solid bulk without the need for diffusive mass transport in the bulk of solid. The size of these connected clusters of element A depends on the crystal structure and alloy composition. The conventional site percolation threshold as defined in percolation theory (*9*) for f.c.c solid is ~ 20%, above which, component A percolates. In other words, on the percolation backbone each A atom should have at least two other A atoms as nearest neighbors, so in the $A_pB_{1-p}$ binary f.c.c alloy system, the composition of A should be greater than 20% to ensure the possibility of selective dissolution.

At the percolation threshold, the backbone has a minimum diameter equal to that of atom A. As composition of A increases, the mean diameter of this percolation backbone, ξ, also increases. There are also "fatter" regions on the backbone but percolation of these fatter regions or large clusters on the backbone does not occur. Wagner et.al suggested that below the critical potential, these larger sizes of clusters are attacked resulting in the noble metal accumulation and surface passivation; at and above the critical potential the average-size clusters on percolation backbone is attacked (*10*). This average length-scale on backbone sets

the instantaneous length scale of the bi-continuous structure that forms during selective dissolution. The approximate diameter, ξ, is well described by one dimensional percolation theory:

$$\xi = \frac{1+p}{1-p}a \qquad (1.1)$$

Where a is the nearest neighbor spacing (*11*, *12*).

Sieradzki et. al indicated that the dealloying threshold and dealloying tendency are directly linked to the differences in equilibrium metal/metal ion potentials among the constituent elements in the alloys (*8*). For alloy systems of $A_pB_{1-p}$, in which a large anodic overpotential of element A can be applied without dissolution of B, A could be dissolved from highly coordinated terrace sites in the alloy surface resulting in bulk 3-dimensional dealloying and nanoporosity formation. Under these conditions, in theory, the dealloying threshold should be close to the site percolation threshold. If one component is extremely reactive, selective dissolution can occur through second-nearest neighbors leading to a slight lowering of the dealloying threshold with respect to classical site percolation threshold. For example, Cu-Al has a dealloying threshold below $p_c$, while Cu-Zn is close to the site percolation threshold in f.c.c lattice. For alloy systems which have moderate difference in elemental reactivity, dissolution of the more reactive elements is restricted to low coordination sites such as kinks, corresponding to a 2-dimensional layer-by layer form of dealloying. In such alloy systems (e.g., Ni-Fe), the

concentration of the more reactive components must be increased to around 60-70% to obtain dealloying. Deviations of dealloying thresholds from classical percolation thresholds can also occur owing to surface diffusion of the more noble metal constituents. The percolation model of dealloying explains the sharp dealloying threshold which is inexplicable by bulk diffusion models (*4*).

As discussed in Pickering's paper, during a potentiodynamic sweep of binary alloys, a passivation behavior is observed until a critical potential is reached, above which, a sharp current increase will occur and a bicontinuous structure with associated finite length scale will be formed. Sieradzki (*11–13*) has studied $E_{crit}$ in detail and in earlier papers argued that it results from a competition between dissolution of the less noble component causing surface roughening (potential dependent), and capillary driven surface diffusion of the more noble component (potential independent) causing surface smoothening. He derived an equation including a kinetic term of surface roughening through silver dissolution and gold surface diffusion smoothening. More recently, Sieradzki and Erlebacher suggested that only thermodynamic parameters controlled the critical potential in the Ag-Au system (*13*). This conclusion was based on dissolution experiments involving Ag-Au multilayers. These multilayers were examined in cross-section for Ag dissolution as a function of the multilayer wavelength. A thermodynamic analysis of the free energy change of Ag layer dissolution allowed them to derive an equation relating

the critical potential for dissolution to the interface energies and the length scale of the Ag layer. They also examined data using Kinetic Monte Carlo (KMC) simulations and using the thermodynamic model they could express the critical potential in terms of the KMC parameters:

$$V_{crit} = \frac{8aE_b}{\sqrt{2}\xi} - \frac{kT}{nq}\ln a_{Ag} \qquad (1.2)$$

where a is the near-neighbor spacing in the lattice, $E_b$ is the bond energy, n is the number of charges transferred per cation formation, $a_{Ag}$ represents the atomic fraction of Ag in the alloy and q the elementary charge. The resultant fit of the critical potential versus alloy composition yielded a value for $E_b$ within a few percent of the input bond energy in the KMC simulation. Through their analysis, it can seen that the kinetic smoothening effect was negligible, which means that the critical potential does not depend on surface diffusion smoothening.

Dealloying is a pattern formation process. There are several parameters needed to be considered during this process: mass transport through the electrolyte, surface diffusion, and the kinetics of dissolution. If the rate-limiting step is in the phase that is growing, perturbations exponentially decay. If the rate limiting step is in the phase that is shrinking, perturbations exponentially grow (*14*). Usually, the mass transport through the electrolyte (growing phase) has a stabilizing influence (*15*) and mass transport through the bulk of alloy is a very slow process, so the morphology determining process is mainly at the interface

region between the alloy and the electrolyte. Historically, some attempts (*16*) have been made to describe the dealloying mechanism atomically, but only recent developments in understanding of dealloying mechanism through Monte Carlo simulations using Ag-Au alloy have given us a better view of it. Through Monte Carlo simulation, Sieradzki et al. (*8*)showed that for randomly packed Ag and Au atoms, two processes were needed to produce the morphology above the critical potential: silver dissolution and gold surface diffusion. The driving force for the latter part is the high curvature of the initial porosity (Gibbs-Thomas effect) resulting in the coarsening of the structure to reduce the surface energy. Later on, Erlebacher (*17*) included more realistic kinetic parameters for silver and gold diffusion and silver dissolution in the KMC model. The rate of dissolution and diffusion was based on nearest neighbor bond breaking. Dissolution (above the critical potential) and passivation (below the critical potential) were both examined and were able reproduce the surface evolution process. A dissolution cartoon extracted from a simulation is shown in Figure 1.5.

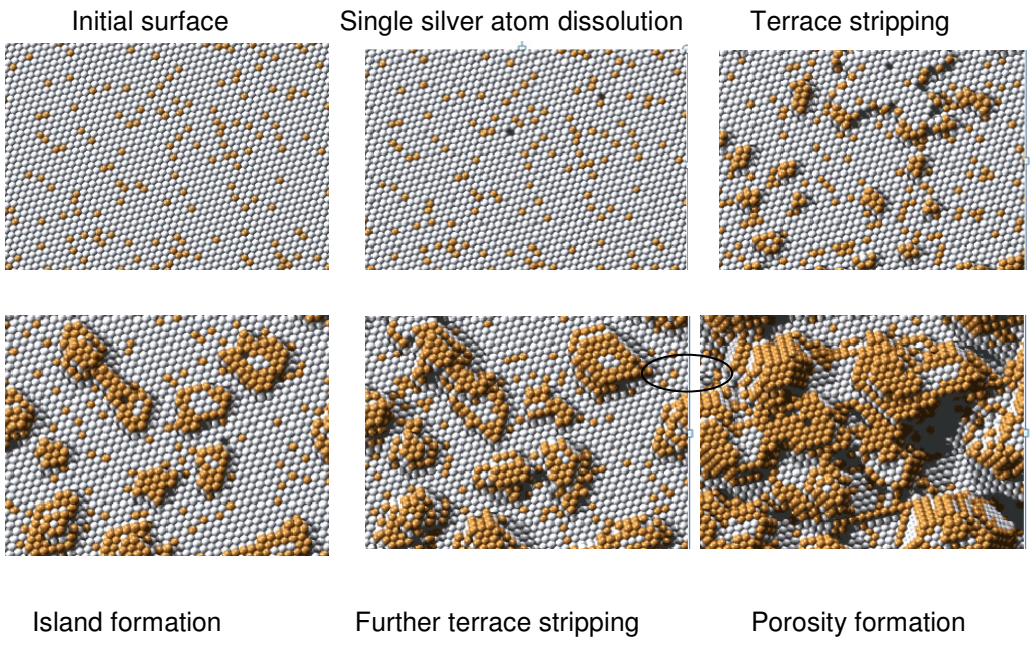


Figure 1.5. Porosity evolution based on KMC simulation by J. Erlebacher (unpublished) (*18*)

The simulation is initiated with the dissolution of a single silver atom from a terrace site, which is rate determining. The atoms that coordinate the newly created surface vacancy, having fewer lateral nearest neighbors, are more susceptible to dissolution at a higher rate than that of the initial dealloying step. Above the critical potential, most of the Ag clusters with average size $\xi$ or larger will be dissolved almost simultaneously. The first layer of terrace is thus largely stripped of silver, leaving gold adatoms without lateral coordination. These gold adatoms have high surface diffusivity due to their low coordination states and diffuse to agglomerate into islands before the next layer is dissolved. Once the silver atoms from the exposed undealloyed regions dissolve, more gold atoms are left over and diffuse to the gold clusters left from previous layer dealloying. This will

continue to form undealloyed regions and expose them to electrolyte. At the initial stages of dealloying, these gold clusters are gold rich at their peaks and of alloy composition at the bases. These clusters get undercut and more surface area will be created. Finally porosity will evolve through this process.

Below the critical potential, The KMC simulation reveals that silver dissolution is a much slower process and only Ag clusters at the step edges or clusters larger than average size were dissolved. The remaining gold atoms were dragged along the moving step edges. After a few layers of dissolution, these gold atoms dragged along the edges form large enough regions to passivate the surface and essentially stop continuous dissolution.

Due to the high interfacial area of nanoporous structure, it is unstable thermodynamically and will undergo rearrangement throughout its life to reduce its surface free energy. The kinetics of coarsening is controlled by the surface diffusion. The experimental pore size-time evolution data gives $t^{1/4}$ coarsening kinetics, which fits well with Charkraverty's surface diffusion model (*19*), in which the coarsening process is considered as detachment of atoms from islands, diffusion across the metal surfaces and coalescence with other islands. The smaller ligaments contribute more to the surface energy than larger ones. The driving force to eliminate the smaller ones is therefore much larger. The resultant effect of coarsening

of nanoporous structure is growth of both ligaments and pore channel, as presented in Figure 1.6 (*20*).

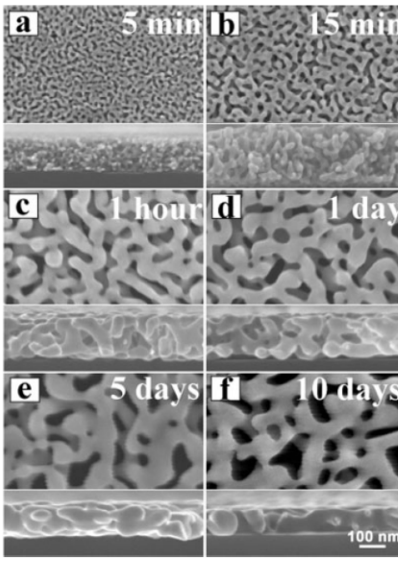


Figure 1.6. SEM images of $Ag_{65}Au_{35}$ (top view and cross section) with continual immersion in concentrated nitric acid (samples were totally dealloyed at around 5minutes) show obvious structure coarsening. The scale bar on f applies to all images, which were taken at the same magnification (*20*).

## 1.2 Mechanisms of stress corrosion cracking

Stress corrosion cracking can be understood as material (usually ductile) failure in a brittle way (intergranular or transgranular fracture) due to the combined effects of a non cyclic tensile stress and a corrosive environment. The environment is usually aqueous and materials are often metallic. A large amount of research has been conducted on this problem because of its importance from an engineering point of view. Understanding how the stress corrosion cracking occurs in different systems can help us decide the suitability of materials, give life predictions and improve the design of these systems under different conditions. Currently a variety of mechanisms have been proposed to describe stress corrosion cracking, including slip dissolution, hydrogen embrittlement, adsorption, surface mobility and film -induced cleavage. A general overview of these models, including their predictions and applicability to given stress corrosion systems is given by Kelly et, al (*21*).

In the large varieties of materials and environment for stress corrosion cracking, some researchers have developed experimental techniques to decouple stress and corrosion effects for certain material-environment systems (*21*, *22*) . With judicious choice of these materials, environment and techniques, a deeper understanding can be reached and a specific mechanism can be studied. Previous researches (*23*, *24*) have shown binary noble alloys are suitable systems to be used to study stress corrosion cracking. The film induced cracking model which will be

discussed in detail has been proved to be a likely mechanism for SCC of noble metal alloys (*21*, *25–29*).

In the following, we will discuss three typical models that were proposed to explain the stress corrosion cracking phenomenon. First, the theory of slip dissolution with its limitations and relation to film induced cracking model is presented. The surface mobility model is then discussed and finally, the film induced cracking model with a discussion of recent work and progress will be introduced.

In the slip dissolution model, also called film rupture mechanism, it is assumed that cracking occurs solely due to localized anodic dissolution at the crack tip. The stress only provides localized plastic strain to rupture a protective film and expose fresh metal at the crack tip to the electrolyte. The dependence of stress corrosion crack velocity on current density in some material-environment systems provides the strongest evidence for the operation of this mechanism (*30–33*). In this model, the maximum crack velocity can be related to the crack tip dissolution rate by Faraday's law (*32*):

$$v = \frac{i_{ct} M p}{n \rho F} \qquad (1.3)$$

Where v -maximum crack velocity; $i_{ct}$ –crack tip dissolution rate; M -the average atomic weight of the alloy; p- atomic fraction of the material that is dissolved; n- the number of equivalents; ρ-density of the dissolved element; and F- Faraday's constant (*33*, *34*).

Although slip dissolution model can explain some cases of intergranular SCC, it fails to account for the discontinuity of crack propagation, the special features of transgranular SCC surfaces and in some systems, the extremely high crack velocities. Acoustic emissions, current transients and crack arrest markings all show that transgranular SCC occurs in a discontinuous manner (*2*, *23*, *35*). Fracture surfaces have been observed to be cleavage-like and have opposite sides that can match and interlock with each other (*35*). In noble-metal alloy systems, the intergranular crack velocity can be extremely high, e.g. 0.1-10mm/s; the current density required for this velocity would be many $A/cm^2$, which is impossible owing to ohmic and diffusional limitations.

Some research conducted on binary noble alloys has already demonstrated that crack propagation is not simply due to dissolution and can be achieved under conditions where no simultaneous anodic dissolution occurs (*21*, *22*, *27*). In the film induced cracking model, anodic dissolution is required, but its continual presence for crack propagation is unnecessary. The role of dissolution is only to produce a thin film which has special properties and can induce cleavage behavior under the action of stress. The detailed discussion on this model will be addressed later.

The second model to be discussed here is the surface mobility model, which was proposed to be an almost universal mechanism that can explain hydrogen-, liquid metal- and solid metal embrittlement and brittle stress corrosion cracking (*36*, *37*). In this mechanism, the environmental

effect is to produce a low melting point surface compound that enhances the surface diffusivity under stress. Thus as in diffusional creep surface vacancies are injected into the highly stressed crack tip region causing the crack propagation process. According to Galvele's analysis, the driving force for the vacancy movement is the vacancy concentration difference between stress-free crack walls and the highly stressed crack tip. He described the equilibrium vacancy concentration at the crack tip based on Nabarro's theory for creep (*38*), which gives the equilibrium vacancy concentration of a flat surface under a normal stress:

$$C = C^0 \exp(\frac{\sigma a^3}{kT}) \qquad (1.4)$$

Where $C^0$ is the equilibrium vacancy concentration on an unstressed flat surface; $a^3$ is the volume change due to the formation of a vacancy; T temperature in degrees K and k the Boltzmann constant. This C is assumed as the equilibrium vacancy concentration at the crack tip in Galvele's analysis and crack tip atoms have to travel certain distance L to the stress free crack walls. With the above assumptions and equation (1.4), Galvele gave the crack propagation rate (c.p.r) simply as the product of vacancy flux and the atomic volume:

$$c.p.r = \frac{D_s}{L}[\exp(\frac{\sigma a^3}{kT}) - 1] \qquad (1.5)$$

Where $D_s$ is the surface self-diffusion coefficient; L the diffusion distance of the adatoms or vacancies (estimated as $10^{-8}$m); σ elastic stress on the crack tip.

In the above analysis and derivation conducted by Galvele, several serious technical errors were pointed out by Sieradzki and Friedersdorf (*39*). First, the surface of the crack tip is a free surface and would not carry any normal stresses. Galvele's analysis of equilibrium vacancy concentration at the crack tip was therefore entirely untenable. Also, due to the existence of fine curvature at the crack tip, his negligence of capillary effects would be a serious flaw. The energetic movement of an atom (via vacancy movement) from a region (like crack tip) to another region with different curvature should be considered. Finally, the use of diffusion equations from concentration gradients, rather than chemical potentials (to include stress and curvature effects) was described as yet another source of error. Sieradzki considered simplified hemi-cylindrical crack tip geometry and used chemical potentials which include stress and curvature effects to derive the equilibrium vacancy concentration on the crack:

$$kT\ln(\frac{c_v}{c_v^0}) = \Delta\mu = -\frac{\sigma_{yy}^{\ 2}}{2E}\Omega + \gamma\kappa\Omega \qquad (1.6)$$

Where $c_v^0$ is the equilibrium vacancy concentration on an unstressed solid surface; Δμ is the chemical potential difference of vacancies with respect to an unstressed surface; $\sigma_{yy}$ the resolved stress at the surface of the

crack tip; $\gamma$ interfacial free energy and $\kappa$ the curvature of the crack tip. The second term on the r.h.s of this equation reflects the curvature effect on the chemical potential. This chemical difference is the driving force for the vacancy flux from the crack flank to the crack tip. The crack velocity was derived as:

$$V_n = \frac{2D_s N_s \Omega^2}{kT\pi r^2}\left(\frac{\sigma_{yy}}{2E}^2 - \gamma\kappa\right) \qquad (1.7)$$

Where $N_s$ is the number of lattice sites per unit area and r is the crack tip radius. The above equation shows us that only the second order stress contributes to the velocity, not the first order stress proposed by Galvele. Sieradzki got the crack velocity of ductile f.c.c metals around 14 orders of magnitude smaller than what Galvele estimates with the assumption that $\sigma_{yy}$=E/1000, $\gamma$=0.5 J/m$^2$ and E=10$^{11}$ Pa. This means that the surface mobility model is not applicable for ductile noble alloys.

The film induced cracking model was proposed by Sieradzki and Newman (*2*, *6*) to explain the brittle behavior of ductile metals during stress corrosion cracking based in part of the work conducted by Edeleadu and Forty on α-brass and similar binary noble alloys (*23*). A basic description of this theory is that brittle cracks, generated in a thin surface layer or film with different mechanical, chemical and structural properties from the substrate, can be dynamically injected in the un-attacked alloy substrate for some distance even if the substrate is a

normally ductile face centered cubic material. These thin layers or films can be oxides, nitrides, chlorides or nanoporous materials. More specifically for binary noble alloys, this film is a nanoporous layer formed by selective dissolution. The role of the environment is to produce this particular layer, while that of the stress is to nucleate a crack with high enough speed so as to be injected into the underlying base material. The important parameters that affect the "cleavage" behavior are the film substrate misfit, film thickness, film ductility and degree of interfacial bonding or coherency. After crack injection into the semi-brittle or ductile substrate, it will arrest under various conditions:

1. Restraining effect of unbroken ligaments connecting the crack faces.
2. Stopped by preexisting or deformation-generated defects.
3. Crack bifurcation.
4. Exhaustion due to the concomitant emission of dislocations during the cleavage process.

In this model, the role of stress and environment is decoupled. The dealloying and mechanical process can then occur at different times from one another and by repetition of these two processes final failure is reached. A quantitative estimation of the crack jump distance was given by Sieradzki and Newman (*6*) based on exhaustion due to dislocation emission. A relationship between initial crack velocity and crack jump distance in the substance was established.

Some research has been conducted to verify this mechanism. The phenomena of the discontinuous cracking and correlated acoustic emission and current transients (*2*) during stress corrosion cracking of α-brass or copper single crystals gave the earliest evidence for Sieradzki and Newman to propose this model. Newman firstly decoupled the effects of stress and the corrosive environment for α-brass in ammonia solution by freezing the dealloyed α-brass in liquid nitrogen (*22*). No brittle fracture was observed when the sample was dried in air before being fractured. In an ammonia solution, adsorption of ammonia was believed to reduce surface mobility and therefore quench the coarsening of the porosity. Indications were shown that intergranular SCC was also brittle. Although the earliest success in observing cleavage events and testing FIC was achieved with α-brass, Ag-Au or Cu-Au alloys were shown to be even more suitable for studying this mechanism considering the control of the electrochemical dealloying process, the acquisition of different dealloying thicknesses, exclusion of unnecessary side reactions and chemical stability of dealloyed thin films in air. Studies on Cu-Au alloys in 0.6 M NaCl (*26*, *27*) and Ag-Au alloys (*21*, *25*) have indicated the applicability of FIC to both intergranular and transgranular cracking and reversibility of the embrittlement by an aging process. Chen et. al (*26*, *27*) showed that the electrochemical contribution to the SCC of Cu-30Au in 0.6M NaCl is the same for both IGSCC and TGSCC and the mode of fracture is determined by the magnitude of the applied stress when samples were dealloyed and

stressed simultaneously. In Kelly's work (*21*), interfacial capacitance was used after the dealloying to verify the surface coarsening process and the effect of coarsening of the dealloyed layer on the intergranular fracture of Ag-Au thin foils in 1M $HClO_4$ . Saito et.al (*25*) demonstrated the relationship further between aging potential & time and the fracture behavior of Ag-20at%Au alloy in 1M$HClO_4$. The coarsening rate of the porosity, which was accelerated by addition of chloride and retarded by pyridine, controlled the fracture mode of tested samples. Friedersdorf and Sieradzki (*28*) showed that for Ag-Au alloys dealloyed in $HClO_4$+$AgClO_4$, the intergranular crack penetration depth ($C_d$) is linearly proportional to the dealloyed layer depth (t) and a parameter m, defined as the ratio between $C_d$ and t, reflected the susceptibility of dealloyed Ag-Au to film induced cracking. This gave support to the film induced cracking mechanism. For gold alloys, intergranular cracking was more prone to be initiated in most of experiments due to the selective attack along grain boundaries in the dealloyed layer. This motivated Barnes et.al (*29*) to use thin Ag-Au thin wires with "bamboo" structure to achieve transgranular cleavage failure with very low stress. The role of the dealloyed layer quality on the crack injection was firstly reported. With optimization of the quality of the dealloyed layer through lowering the dealloyed potential and increasing reaction temperature, complete intergranular crack can even be injected after aging in deionized water for 5 minutes.

While most of examples discussed above used Ag-Au alloys to study crack injection, the most well known and studied is referred to the ductile/brittle transition (DBT) in steels, which is analyzed to be initiated by cracking of brittle carbide particles (*40*). The stress field from a group of piled-up dislocations at a carbide/ferrite interface causes cracking of carbide with suitable size and below the DBT temperature the micro crack is dynamically injected into the more ductile ferrite phase resulting in macroscopic sample failure. Such kind of event depends on local stress, the size of the carbide and temperature. Lin et al. (*41*) described this behavior as a dynamic fracture process that analyzed the statistical likelihood of having suitably sized carbide within a process zone and the temperature and strain rate dependence of plastic flow in ferrite. The physics of this relates to plastic dissipation of the kinetic energy of a moving crack in the ductile phase. Here it is assumed that the energy dissipated by plastic processes is much greater than the associated intrinsic surface energy. The size of the plastic zone ahead of the moving crack shrinks with increasing crack velocity causing a decrease in the fracture toughness of the ductile phase (*42*). Even above the DBT temperature this process can result in significant injection events of microcracks (in the order of grain size) in to the interior of ferrite grains. In analogy to the problem described above, film induced cleavage model a brittle dealloyed layer serves to initiate a dynamically moving crack that then arrests owing to kinetic energy dissipation after propagating in a

cleavage mode for some distance (in the of order micron) into the ductile un-dealloyed parent-phase material. In electrolyte the layer reforms at the arrested crack tip and the process repeats.

More modern examples of cleavage in f.c.c solids can be seen in the fracture behavior of some multilayers. Cleavage of copper layers in Cu/Nb and Cu/Zr multilayers has been observed (*43*). Another example of cleavage in copper is reported from spallation experiments where apparently owing to dynamic effects micron-sized brittle cracks have been observed (*44*). Finally, experiments conducted by NIST group (*45*) give one more example of crack injection and cleavage in an f.c.c metal. These experiments involved the electroplating of a brittle Rh layer (~2 microns in thickness) on to a Ni sample. Then the samples were vacuum annealed to bake out any hydrogen that may have entered the Ni sample during Rh plating. On loading, cracks initiated in the brittle Rh layer and penetrated into the Ni substrate to distances of ~ 0.5-1 um; similar to that observed (spacing between crack arrest markings) in transgranular DISCC.

## 1.3 Mechanics of NPG

### 1.3.1 Mechanical properties of NPG

As mentioned above, porous layers formed by selective dissolution can cause SCC in alloys. Also, due to special characteristics of NPG, like bi-continuous structure with high surface area and tunable length scales, it has become a very promising material for numerous applications, e.g. biosensors (*46*), catalyst (*47*) and actuators (*48*). To have a better

understanding of the porous structure and to optimize its geometry, mechanical properties of NPG need to be investigated.

Au is a ductile metal, but NPG can behave in a brittle manner. Li and Sieradzki (*49*) were the first to report a micro structural length scale dependent ductile-brittle transition using three point bending tests. At that time it was assumed that the plastic behavior of the gold ligaments was size-independent so that this behavior was interpreted as a statistical "sample-size" effect. However, the intrinsic size effect must play an important role in the ductile-brittle response of NPG based on recent research on the plastic behavior of gold (*50*). Today it is well known that sample dimensions have big influence on the mechanical properties of a solid. The yield strength of dislocation free metal whiskers can be as high as the theoretical shear strength of a solid. The compression testing of focused ion-beam machined (FIB'd) single crystal nickel pillars (*51*) showed that over a range of 40um to 5um diameter samples, there is a gradual increase of the yield stress until the physical size limitations is reached, where 5 um diameter samples display large strain bursts upon yielding. Interpretation of these results is given that sample size affects the ability of dislocation multiplication or the number of dislocation sources.

The ligaments of nanoporous dealloyed structures can be considered to be dislocation free (*52*, *53*). There are around $10^{11}$ nanoscale ligaments per square millimeter in NPG structures while for well annealed metals the density of dislocations is around $10^{3}$~$10^{5}$ per square millimeter. The strong

image force acting on the dislocation in the ligament also helps to remove mobile dislocations. As we know, the image force on a grown-in dislocation is inversely proportional to its distance from the free surface. For the distance in the order of ligament size, the image force is larger than friction stress and therefore pulls the dislocation out of the ligament. If the surface acts as a dislocation source, like a Frank-Reed source, the dislocation needs to be bowed out of the surface. The stress needed to activate this source is given by: $\sigma=Gb/l$, where l is ligament size, G shear modulus and b burger vector. So the stress needed to activate a dislocation source would be on the order of G/10 with b around 0.3nm and ligament sizes of 3-10 nm, approaching the theoretical strength of materials.

The above theoretical analysis is verified by recent mechanical tests conducted on NPG materials. Firstly nano-indentation tests (*54–56*) have obtained yielding stress of NPG approaching the theoretical yield strength of gold, which is in the order of 1.5-8 GPa. Biener et al. (*54*) were the first to introduce the usage of instrumented nanoindentation into testing plastic yielding and flow of NPG. A mean hardness of 145(±11) MPa and a Young's modulus of 11.1(±0.9) MPa for 100 nm nanoporous structure was obtained and with the assumption that $\sigma_y$ equals hardness, yield stress of NPG is obtained using the Gibson-Ashby (*57*) scaling laws for porous foams:

$$\sigma = 0.3\sigma_s(\frac{\rho_{ns}}{\rho_s})^{3/2} \quad (1.8)$$

Where $\sigma_s$ and $\rho_s$ is the yield stress and density of solid material, $\rho_{ns}$ is the density of NPG. The yield strength of the solid Au is in the order of 1.8 GPa. Hakamada et.al demonstrated that the yield stress of NPG increased as the ligament size decreased (*55*). As-dealloyed structure exhibited yield stress around 1 GPa. Hodge et al. (*56*) performed nanoindentation tests on NPG with relative density ranging from 20% to 42% and ligament sizes from 10 to 900 nm. At the nanoscale, the yield strength depended on both the relative density and the ligament length scale. Using scaling equations, they calculated the ligament yield strength follows $L^{-1/2}$ with the ligament size. In addition to nanoindentation tests, FIB machined micro pillar compression tests were also employed. Volkert et al. (*58*) studied the stress strain behavior of FIB machined micro pillars of NPG with column aspect ratio between 2 to 3 and ligament size at 15nm. With scaling law, the ligament Young's modulus was predicted between 7 and 11 GPa, which is in good agreement with the modulus obtained from nanoindentation test (*54*), and the yield strength was around 1.5 GPa for 15 nm ligaments. Recent investigation (*59*) shows that NPG exposure to FIB may cause grain boundary cracking and ligament coarsening. As a result, the mechanical properties of NPG may be modified with FIB machining. Motivated by this issue, Jin et al. conducted compression tests on millimeter-sized NPG samples to remove the

influence of possible artifacts from machining (*60*). The compression test result gave yield strength value for ligament is around one order of magnitude smaller from that of the nanoindentation and micro pillar compression tests. For example, for 55 nm the ligament yield strength is only around 190 MPa. Another interesting finding in their experiment is that the sample deformed homogenously, which is quite different from conventional low density foam local deformation behavior. They argued that in NPG yielding of individual ligaments is a cooperative process owing to the coherent lattice (i.e., individual ligaments within a grain have the same crystallographic orientation) and pore structure. Thus, shear processes can be transmitted across pores from ligament to ligament which differentiates this behavior from that of free-standing wires or pillars. As shown in Figure 1.7, on a microscopic scale they argue for the presence of dislocation cores within the pores in analogy with Frank's so-called hollow-core dislocations. However, this argument seems fundamentally flawed to us because if the Burgers circuit is taken as a loop surrounding the pores defining the ligament, there is no net dislocation content with the sheared ligament. Thus it is believed that the behavior of ligaments within NPG structures can be explored by examining the behavior of similarly sized wires or pillars. The intrinsic size effect on yielding must be an important aspect of plasticity in NPG structures in either case.

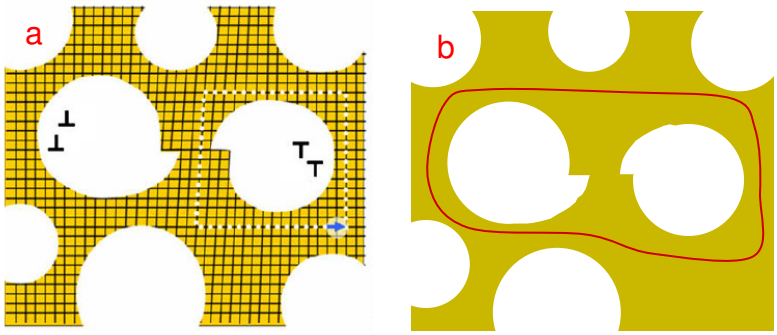


Figure 1.7. Shear failure of NPG ligame... and "pore-channel" dislocations. a. Jin et al's. representation of ligament shear in a coherent porous structure showing the passage of two lattice dislocations and the corresponding closure failure of the Burgers circuit (white dots) (*60*). b A Burgers circuit (red line) taken around the entire sheared ligament showing no closure failure.

Because results interpretation is more complicated for compression tests which make materials more compact during tests, tensile and bending tests have also been performed to study the mechanical properties and fracture behavior of NPG. Biener et al. (*61*) completed one set of these experiments using a three-point bending instrument on NPG prepared by electrochemical dealloying. Macroscopic brittle failure of NPG was due to the internal network structure rather than ligament brittleness. During bending of NPG with ligament sizes around 100nm, fracture propagated from tension side to compression side and the specimen showed no macroscopic plastic deformation. Microscopically, necking features on some ligaments revealed ductile fracture. Void like defects produced along silver enriched grain boundaries were the origins of crack nucleation sites due to local stress enhancement. Ligaments connecting these sites were the first to rupture and necking was observed. This

means that microscopically, NPG is a ductile material despite its macroscopic brittle behavior. For annealed samples which have a ligament size ~1 um, the overall fracture morphology does not change except that very large degree of plastic deformation of individual ligaments by slip was detected. Annealing was attributed to the network strengthening through diffusion to eliminate those void-like defects.

The nanoporous structure is analogous to the random fuse network analyzed by Kahng et al. (*62*). Macroscopic brittle behavior can be expected for network with a narrow ligament strength distribution even if individual ligaments are ductile. Therefore, the brittle fracture of the nanoporous structure is only triggered by rupture of the weakest ligaments. The changing of critical ligament failure mechanism indicates that dislocation activity is suppressed by the nanoscale structure. Lee et al. (*63*, *64*) measured the elastic modulus and yield stress of double clamped beams of NPG made from Ag-Au leaf with ligament sizes ranging from 20 to 40 nm. The elastic modulus was about 9 GPa for $\rho_{ns}$ =0.35 and the yield strength was about 111 MPa. The corresponding ligament stress based on scaling laws is around 1.45 GPa, which agrees well with other mechanical tests. Strong evidence also shows typically brittle fracture with localized plastic deformation in individual ligaments.

Since small ligament size NPG has a high surface to volume ratio, the plastic response of NPG would be sensitive to alterations of the surface chemistry. Such behaviors have often been termed Rehbinder effects (*65*).

Only one recent investigation is known exploring this behavior in monolithic NPG (*66*). Figure 1.8 reproduces results of that study pertaining to our work herein and shows compression test results for 20nm ligament size NPG in 1M perchloric acid. The plastic flow behavior of NPG is extremely sensitive to its surface condition that is controlled by the applied electrochemical potential. At a voltage of ~ 1.4 V (SHE) there is a monolayer of oxide on the NPG surface, which results in higher flow-stress and more brittle behavior of NPG than that at ~ 1.0 V. At this lower voltage there is a low-density full coverage perchlorate adlayer on the NPG surface (*67*). Furthermore, by cycling between these potentials, the flow stress was “reversibly” tuned by larger than a factor of two. More remarkably, the flow stress behavior was essentially retained for dry samples treated at these two potentials. Since densification of compression necessarily result in densification, more pronounced brittle response of NPG would be expected for similar treatments under tensile loading. These results provide important evidence for us to study dynamic fracture in NPG under conditions relevant to SCC.

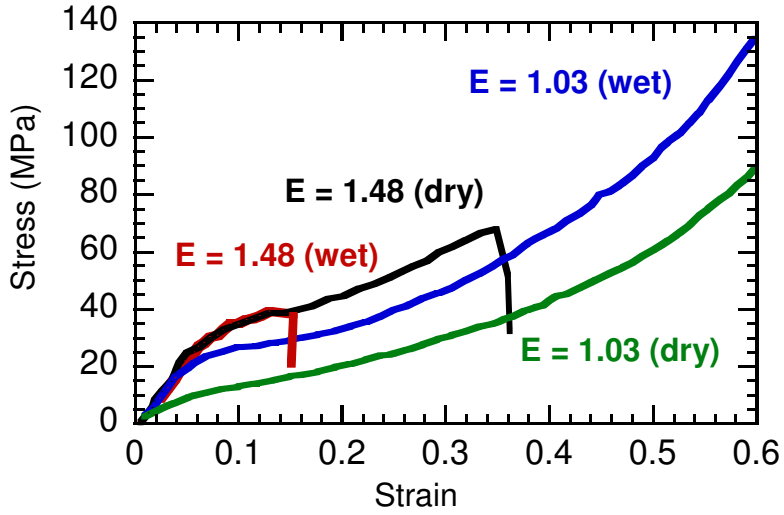


Figure 1.8. Compression of nominal 20 nm length scale monolithic NPG in dry and wet state. The dried samples were removed from electrolyte under potential control and dried for 8-9 days. At 1.48 V (NHE) there is a surface oxide on the NPG ligament surfaces while at 1.03 V the surface is covered with an adsorbed perchlorate adlayer. The lower yield strength in the dry 1.03 V sample resulted from coarsening during drying. Note that the oxide covered dried sample did not undergo measurable coarsening (*67*).

How does NPG fracture? For an individual ligament, fracture occurs by a shear process, i.e., at a sufficient level of stress, plastic shear is initiated within the ligament and separation occurs via conventional dislocation induced block-on-block sliding (*49*). As has been analyzed theoretically or based on recent results of size-dependent Au pillar compression experiments, it is possible that for small enough ligament sizes the stress level required to initiate this block-on-block sliding may be near to the theoretical shear strength of gold (*68*). While individual ligaments of NPG fail by a shear process, it would be argued that at small

enough ligament size the macroscopic behavior of monolithic NPG will be "brittle" and so able to support dynamic fracture. To date, even the static fracture properties (e.g., fracture toughness) of this type of solid has not been examined and taken together with a study of dynamic fracture.

### 1.3.2 Crack dynamics in NPG

In order to assess the role of crack dynamics in the FIC mechanism, a detailed understanding of crack dynamics in homogeneous solids is essential. For example, we need information on the following:

- How does the initial crack velocity in a brittle solid depend on stress (or stress intensity)?
- How does the crack velocity depend on crack length (or time); i.e., is there a crack tip equation of motion?
- What are the strain rates at the tip of an advancing brittle crack?

Over the last 20 years there has been considerable progress in understanding crack dynamics that address some of these issues (*69*–*71*). For example, for a dynamic elastic crack in a semi-infinite solid, the crack velocity depends only on the instantaneous value of the stress intensity (*72*, *73*). Nevertheless a number of important issues remain open such as the magnitude of crack terminal velocities and the effects of finite sample size. A number of different analytical approaches have been used to examine these issues but they all result in nearly identical results for crack velocity versus crack length. Accordingly, the simplest approach that we

will review is based on an energy balance formulation first derived by Mott (*74*).

The Griffith criterion of the critical stress for crack propagation uses the energy balance concept which indicates that the surface energy increase due to the crack extension is balanced by the strain energy change during crack propagation. This criterion has successfully explained the critical stress for fracture initiation in solids. Below the critical stress, the system only possesses potential energy; above the critical point, the system posses both potential and kinetic energy. Mott (*74*) included a kinetic energy term into the energy balance concept similar to that of Griffith to analyze the energetics of the crack propagation process. His theory predicts a terminal velocity of a crack dependent on the material parameters: Young's modulus and density. Roberts and Wells (*75*) modified this by considering only a small region around the crack tip and obtained a terminal velocity of 0.38 $V_L$ ($V_L$ is the longitudinal sound velocity in solid). In Mott's approach, the mechanical energy release rate, G, is a term defined based on the work done on the solid by the external force, W and the strain energy of the solid, $E_{el}$,

$$G = \frac{1}{b}\frac{d(W - E_{el})}{da} \tag{1.9}$$

Where a is the crack length and b is the crack width. Mott set G equal to the surface energy term R, plus the derivative of the crack kinetic energy

relative to the crack length, $\frac{1}{b}\frac{dE_{ke}}{da}$. Considering all energies per unit crack thickness and using the linear elastic result of $\Delta W = 2\Delta E_{el}$ (constant load boundary condition), the following relation is derived:

$$G = \frac{d(E_{el})}{da} = 2\gamma + \frac{dE_{ke}}{da} \qquad (1.10)$$

Where γ is the energy required to create a new surface of unit length as the crack propagates. Based on linear elastic theory, the magnitude of the elastic strain energy change is the same for both constant load and constant displacement boundary conditions. Mott made two assumptions to solve the above equation so as to obtain a relationship between crack velocity and crack length. The first one is the calculation of $\frac{dE_{ke}}{da}$ using the static or equilibrium value of $E_{el}$ from a continuum mechanics formulation. Therefore, $E_{el}$ can be represented as:

$$E_{el} = \frac{\pi L^2 \sigma^2}{E} \qquad (1.11)$$

Where E is Young's modulus of the solid and σ is the applied stress. The second assumption is that the energy consumption rate depends on both crack velocity and crack length because the kinetic energy involves both of them. It can then be expressed as:

$$E_{KE} = \frac{1}{2}\frac{k\rho v_c^{\,2} L^2 \sigma^2}{E} \qquad (1.12)$$

Where k is undetermined constant, ρ is the density of the solid, $v_c$ is crack velocity and L is crack length. Based on equation (1.11) and (1.12) and the Griffith criterion, a relationship between crack velocity and crack length is given as:

$$v_c = (\frac{2\pi E}{k\rho})^{1/2}(1-\frac{L_0}{L}) \qquad (1.13)$$

When L >> Lo, crack velocity reaches a terminal velocity of (2πE/kρ) ½.

In comparison to Mott's prediction, Freund (*76–78*) used a different formulation also based on continuum mechanics and a stress intensity approach. In his derivation, an explicit relationship for an energy flux quantity F is obtained as:

$$F = \frac{d}{dt}[W-(E_{el}+E_{KE})] = v_c G_F = \frac{v_c A(v_c) K^2(v_c,l)}{E} \qquad (1.14)$$

Where $A(v_c)$ is an analytic relation depending on $v_c$, and $K(v_c,l)$ is a dynamic stress intensity factor evaluated by Freund and valid near the crack tip. An approximate form for $A(v_c)k^2(v_c)$ is derived as follows by writing $K(v_c,l)$ as $k(v_c)K(0,l)$ where $K(0,l)$ is static stress intensity:

$$A(v_c)k^2(v_c) \approx (1-\frac{v_c}{v_R}) \qquad (1.15)$$

where $v_R$ is the Rayleigh wave velocity. For a system with only surface energy consumed, conservation of energy gives the following result:

$$F = v_c R = v_c 2\gamma \tag{1.16}$$

and

$$A(v_c)\frac{k^2(v_c)K^2(0,l)}{E} \approx (1-\frac{v_c}{v_R})\frac{K^2(0,l)}{E} = 2\gamma \tag{1.17}$$

By substituting $K = \sigma\sqrt{\pi l}$ into above equation together with the Griffith criterion, we can get:

$$v_c = v_R(1-L_0/L) \tag{1.18}$$

Freund result of Equation of 1.18 is in the same form as that obtained in equation 1.13 although their basis assumptions are different. Mott took assumption of quasi-static equilibrium values of the work and strain energy terms, while Freund gave explicit evaluation of the non static contributions to these terms. Energy flow term as a consequence of equation 1.17 shows that the product of crack velocity dependence and crack length dependence is a constant, therefore, if crack velocity is constant at any time, the evaluation of dynamic stress intensity factor must be wrong as $K^2(0,l)/E$ must also be a constant, which violates basic definition of static stress intensity factor. Consequently, both in Freund and Mott's formation, a constant crack velocity within a finite range of

crack length L is not allowed. However, some experimental results (*79*) as well as some computer simulations have demonstrated constant crack velocities over a range in the stress intensity factor of about 2. In addition, the shape of crack velocity vs crack length curves from computer simulation or experiments is different from theoretical analysis. The crack velocity approaches a constant value much faster than predicted from Mott or Freund's analysis.

Brittle crack dynamics in a material like NPG is further complicated by a number of issues involving the nanoporous ligament size, the heterogeneous microstructure and the corresponding complicated stress state that the variously oriented ligaments experience even under nominal uniaxial load conditions.

# Chapter 2

## EXPERIMENTAL PROCEDURE

Two main types of experiments have been conducted on Ag-Au alloys to study the role of dealloyed nanostructures and dynamic fracture in dealloying induced stress corrosion cracking phenomena. One set of experiments referred to as crack injection involved forming a thin nanoporous layer on polycrystalline Ag-Au alloys in neutral electrolyte and applying load on the dealloyed samples under various conditions to cause intergranular fracture. Dynamic tensile loading and bending methods have been used for crack injection. After crack injection, specimens were examined with the dual-beam FIB tool to obtain high resolution images of crack cross sections. The composition at the crack walls was also analyzed with analytical microscopy techniques to verify that no dissolution occurred at crack walls lying within nominally un-dealloyed substrate. The other series of experiments was centered on dynamic fracture in monolithic nanoporous gold as a function of length scale and electrochemical condition. A number of these experiments were also performed on dry nanoporous gold samples in laboratory air. Mechanical bending in a specially designed teflon cell and tensile loading on micrometer controlled vise have been used to induce dynamic fracture. The crack velocity during dynamic fracture was measured with a Phantom high speed digital camera which can capture up to one million frames per second.

Ag-Au alloys supplied by Gold fellow Company were used for crack injection experiments and preparation of crack free nanoporous gold. These alloys were heat treated at 900 ℃ for 24 hours. All alloys were fabricated from 99.999% purity stock. In Table 2.1, the alloys used are listed, including their composition, supplier, heat treatment after special machining processes and before dealloying. The composition of the Ag-Au alloys was verified using energy dispersive x-ray spectroscopy (EDS). The EDS analysis was performed on a Nova 200 equipped with Thermo Scientific Noran EDS system.

Table 2.1. Alloys used in this study: composition, producer, heat treatment and usage

| Alloy | at% Comp.(EDS) | Analysis | Heat treatment | Producer | Usage |
|---|---|---|---|---|---|
| AgAu70/30 | 68.9/31.1 | EDS | a | Good fellow | Crack injection |
| AgAu72/28 | 72.9/27.1 | EDS | a | Good fellow | Monolithic nanoporous gold |

a. Sand to 4000 grit finish, Alumina powder polished (5 um-0.3 um-0.05 um). Held in between quartz plates and annealed @900 ℃ for 24hours.
   Bending tests: thickness surface polished; Tensile test: side surface polished

The AgAu70/30 alloy was used for crack injection experiments; AgAu72/28 alloy was used for preparation of crack free nanoporous gold and crack dynamics experiment. Both alloys were EDM cut into a

rectangular shape with different sizes and AgAu72/28 samples with different size notches introduced by EDM wire cutting, were cleaned with acetone and rinsed with de-ionized water prior to heat treatment. After heat treatment, specimens were furnace cooled.

## 2.1 Crack Injection Experiments

### 2.1.1 Electrochemical Dealloying

To study film induced cleavage phenomenon, a thin nanoporous layer needs to be formed on the surface of Ag-Au alloys. Snyder's result (*80*) has shown that dealloying of Ag-Au alloys in silver nitrate electrolyte at 1.4-2.0 V vs NHE can produce very fine and stable porosity, which is desired for our experiments. We chose 0.1M $AgNO_3$ solution, which was prepared from reagent grade $AgNO_3$ and de-ionized water, as the electrolyte for electrochemical dealloying with the control of Gamry electrochemical working station.

Potential dynamic scans were run to examine corrosion behavior of polycrystalline Ag-31at%Au in 0.1M $AgNO_3$. The annealed specimens were rectangular in shape, 1.5 cm ×0.5 cm×0.06 mm and cleaned with acetone then rinsed with de-ionized water before use. Copper tape was used for electrical connection and specimens were masked with nail polish that was electrically insulating so that only a fixed area of specimen was exposed to electrolyte. The nail polish was left to dry for over 3 hours. Then specimens were placed in a standard three-electrode cell, with one counter electrode of platinum wire and one reference electrode of

Mercury/ Mercurous Sulfate. The platinum wire was cleaned with concentrated nitric acid and sulfuric acid and then $H_2$ flame annealed. A Gamry electrochemical work station was used to perform polarization scans. The scan rate was usually10 mV/s.

The polarization curves allowed us to determine the beginning of bulk dissolution and the suitable dealloying potential regime for our specific alloy composition. With the desired dealloying potential, a thin layer of nanoporous gold was generated by chronoamperometry (constant potential dealloying) on each specimen for crack injection experiments. The constant dealloying potential was determined from the polarization curve of Ag-31at%Au in 0.1M $AgNO_3$. The dimension of specimens used for crack injection experiments is 1.5 cm ×0.5 cm×0.06 mm and these specimens were loaded into respective experimental setups for dealloying and subsequent crack injection tests for tensile loading crack injection method and the hand bending method.

Due to the formation of a thin layer of silver oxide with high potential dealloying, only a rough estimate of dealloying time based on the dealloying current density and predetermined dealloying depth was given for each test according to

$$Q = \frac{tF\rho Anp}{at.wt} \tag{5.1}$$

where t is dealloyed film thickness; Q the total charge passed during dealloying; F, Faraday's constant, at.wt, atomic weight, ρ, the density of

the alloy, A the area of the working electrode, n ther number of equivalents and p the atomic fraction of silver in the alloy.

2.1.2 Crack Injection

2.1.2.1 Dynamic Tensile Loading

The advantage of dynamic tensile loading test is uniform straining. To conduct this tensile loading experiment, a specific loading jig was designed and fabricated to ensure electrochemical dealloying and dynamic loading can both be achieved. This device is mainly composed of 4 parts: an aluminum stage, Teflon beaker, grips, and a long stainless steel rod with weights. An image of this system is provided below:

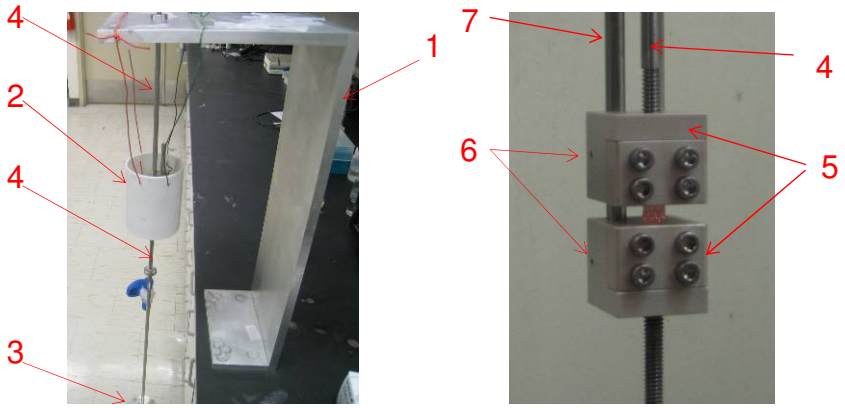


Figure 2.1. Dynamic tensile loading device for crack injection 1- Aluminum Stage used to hold teflon cell; 2- Teflon cell for electrochemical dealloying of test specimens; 3-Aluminum plate to hold loading weight; 4- Long stainless steel rods used to hold and connect peek grips. 5-Peek Grips used to hold Ag-Au specimens. 6-Side screws on grips used to control free movement of specimen grips on the short stainless steel rods. 7-Short stainless steel rods used to connect specimen clips and ensure alignment and free movement.

For this test, fully annealed specimens were treated as described above. Copper tape was used for electrical connection and the samples were masked with nail polish at the interconnection area to ensure electrical insulation. The sample length between two clips was exposed to electrolyte and kept to be 5 mm for dynamic loading tests. The sample was first mounted into the two grips with side screws tightened to ensure no stress was applied to the specimen during loading in the jig. The two grips with top stainless steel rods screwed in were then placed into Teflon beaker and the bottom stainless steel rod connected to Al plate was screwed into the bottom peek grip through a hole at the bottom center of Teflon beaker. A stainless steel nut and Teflon o-ring was used to prevent leakage of electrolyte. A platinum wire, pretreated as described above and one silver wire, etched by diluted nitric acid, were then put into Teflon beaker. With the control of Gamry electrochemical station, specimens were dealloyed for prescribed time to obtain estimated dealloying depth. The planned experiments were to stop dealloying after obtaining certain dealloying depth, then wait for certain period of time and apply impact loading to fracture test samples. During the dealloying process, a small stress arising from teflon cell, electrolyte and stainless steel rod was on the specimen because side screws on the both grips were loose. Such a small stress during dealloying caused three of the test specimens to fracture during the dealloying process (stress-corrosion). The fractured time varied from 20 seconds to 90 seconds. Three other test samples

were impact fractured after dealloying and subjected to wait for 5 to 90 seconds. After fracture, the specimen was removed from the cell and rinsed by de-ionized water for the following SEM and FIB analysis.

2.1.2.2 Hand Bending

The second strategy for crack injection is direct hand bending of the dealloyed specimens. This method is more straightforward and much easier to control because no special instrument needs to be designed.

The hand bending tests were conducted on the Ag-Au alloy with the same composition, geometry and heat treatment as the dynamic loading tests. The specimens were pretreated as described previously in the dynamic loading test and then dealloyed as a working electrode in a normal glass beaker containing one counter electrode of platinum wire and one reference electrode of silver wire. The dealloying potential was same as the dynamic fracture test. After a thin layer of porous structure on the surface of Ag-Au alloys was generated, two methods were used for specimen coarsening before crack injection by direct hand bending: one was in the electrolyte without potential control; the other ex-situ (out of electrolyte in DI water and in air). Coarsening times from 1 to 40 minutes were chosen to examine the effect of ligament coarsening on the ability of the porous layer to inject cracks into the un-dealloyed parent phase substrate. Coarsened specimens were held at both ends and bent by hand.

The fracture surfaces and cracks near the fracture surfaces produced by dynamic impact loading or cracks produced by bending with hands were analyzed with SEM, EDX and FIB (focused ion beam) milling techniques. This post fracture analysis gave the failure mode of the fracture surface and crack penetration depth in the dealloyed layer and parent phase bulk material. In order to more clearly differentiate the dealloyed and un-dealloyed regions, all these specimens were annealed at 200 ℃ for 10 minutes in air before analysis to facilitate the delineation of dealloyed layers from un-dealloyed parent phase.

2.1.3 Crack milling experiments (FIB milling)

2.1.3.1 Introduction to focused ion beam technique

Focused ion beam machining, also known as FIB, is a technique first developed in the early 1970s used particularly in the semiconductor and materials science fields for site-specific analysis, deposition, and ablation of materials. A FIB setup uses a focused beam of ions to provide four basic functions: milling, deposition, implantation and imaging.

Mostly used are Liquid-metal ion sources (LMIS), especially gallium ion sources. Gas field ion or plasma sources are also available. In a Gallium LMIS, gallium metal is placed in contact with a tungsten needle and heated. Gallium wets the tungsten, and a large electric field causes ionization and field emission of the gallium atoms. Source ions are then accelerated to high enough energies, and focused onto the specimen through lenses. LMIS can provide ion beam sizes less than 100nm in

diameter and high current density close to 1 A/cm$^2$. Therefore, a modern FIB can be operated at low beam currents for imaging with a spot size on the order of a few nanometers or high beam currents for site specific sputtering and milling down to few nanometers.

As the gallium (Ga+) ion beam hits the specimen surface, Ions and solids will interact with each other and several processes occur simultaneously. A small amount of material is sputtered out and the surface is left as either secondary ions ($i^+$ or $i^-$) or neutral atoms ($n^0$). The ion beam also produces secondary electrons (e-). The signal from the sputtered ions or secondary electrons is collected to form an image. At low beam currents, very little material is sputtered and 5 nm imaging resolution can be achieved. At higher primary currents, a great deal of material can be removed by sputtering, allowing precision milling of the specimen down to a sub micrometer scale[68]. Besides the imaging and milling function, an FIB tool can also be used to deposit material[69]. When a gas, such as platinum nonenyl (Pt ($C_9H_{17}$)) is introduced to the vacuum chamber and allowed to be chemisorbed onto the specimen, the scanned ion beam will help decompose this precursor gas into volatile and nonvolatile components. The latter, such as platinum, is left on the surface as a deposition layer, which can work as a sacrificial layer to protect the underlying work piece from being destroyed during ion beam sputtering. Tungsten, carbon, and gold can also be deposited on the substrate surface. This technique can be used to improve electron beam imaging by

depositing a conductive layer. The ion beam induced deposition process is shown in Figure 2.2.

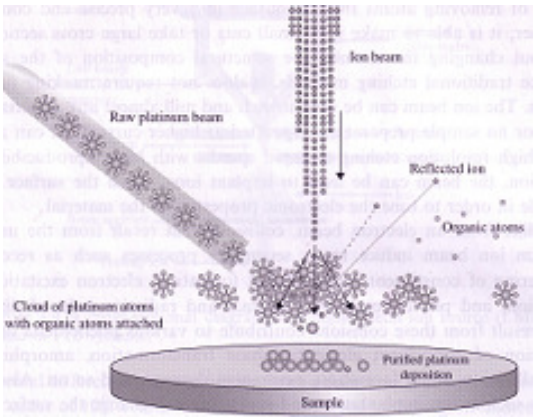


Figure 2.2. A schematic diagram of an ion beam induced deposition process (*81*)

The FIB can be incorporated in a system with both electron and ion beam columns, allowing the same feature to be investigated using either of the beams. The Nova 200 Nanolab system used for this research is a dual-beam system. The ion beam and electron beam are at 52 degrees apart. A sketch for the specimen and beams distribution during viewing and milling process is shown in Figure 2.3. The user can switch between the two beams for quick and accurate navigation and milling. The milling process can be monitored with a high-resolution electron beam to prevent any unwanted modification or damage of very small features. Besides providing non-destructive imaging, the electron beam can also be used for lithography and deposition on a nanoscale. The deposition mechanism is almost the same as ion beam deposition mechanism except that ions are

changed to electrons. The dual-beam systems can offer a wide range of nano-machining, lithography and specimen preparation for various characterization techniques, like TEM.

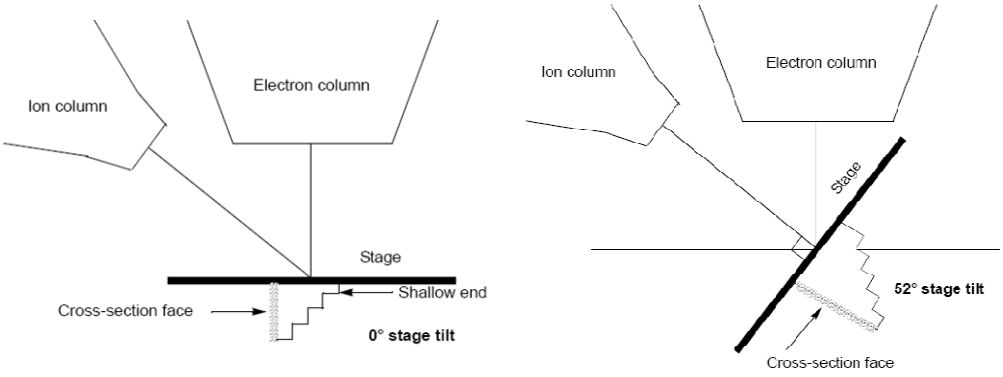


Figure 2.3. Specimen & beams distribution during $0^0$ viewing (left) and $52^0$ milling (right) (*82*)

2.1.3.2 FIB milling on crack injected Ag-Au alloys

Why were FIB and dual-beam technologies chosen to detect cracks in the crack injected Ag-Au alloys?

As discussed above, the dual-beam system is a powerful tool for site-specific analysis, especially in the field of metals research. The deposition function can provide a sacrificial layer of platinum to protect the specimen surface from destructive sputtering. This is the first important point for the FIB milling experiment because the delicate nanoporous surfaces can be easily destroyed by direct ion beam milling. With a protected surface, it is easy to detect the sharp separation between the dealloyed layer and underlying parent phase bulk alloy. In addition, for Ag-Au alloys, the grain

boundaries can be rich in silver due to segregation, so preferential grain boundary penetration during dealloying is a very prevalent phenomenon. Previous research on FIC did not provide clear evidence to exclude the possibility that grain boundary penetration by dealloying caused fracture. FIB and dual-beam techniques solve these issues easily. FIB milling can provide very smooth cross sections of any crack. At the same time, high-resolution electron beam imaging can offer images with magnification up to 500, 000, so detailed features down to a few nanometers around cracks can be observed.

In this part of experiment, high resolution SEM was first used to image the top surface of stressed specimens to locate certain wide cracks (as shown in Figure 2.4). After location of a desired crack, an electron beam induced platinum layer was firstly deposited on the surface and worked as the first protection layer for further ion beam imaging and platinum deposition. The two layers of platinum deposited with electron and ion beams are shown and illustrated in the following SEM image of one FIB milled crack (Figure 2.5). High-resolution images of the crack cross sections provided the dealloyed layer and crack penetration depth.

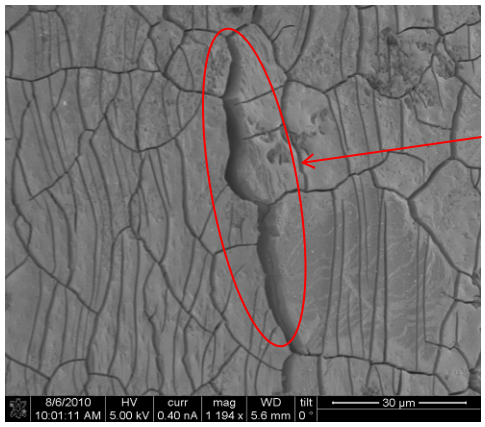


Figure 2.4. SEM image of a wide-open intergranular crack on the top surface of Ag-Au alloy that was dealloyed and then stressed for crack injection. These open cracks were selected for FIB milling.

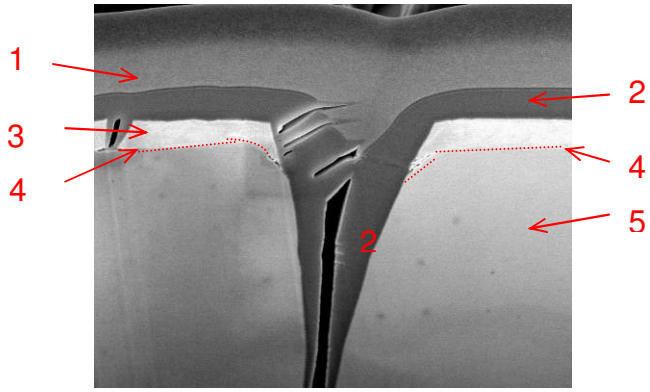


Figure 2.5. An SEM image of one FIB milled crack with electron beam and ion beam induced platinum deposition layers on specimen top surface. 1- Ion beam induced Pt deposition layer; 2- Electron beam induced Pt deposition layer; 3- Dealloyed layer; 4- Obvious boundary between dealloyed and undealloyed layers; 5- Undealloyed bulk.

2.1.3.3 Composition analysis along the crack walls using the analytical microscopy.

Compositional analysis along the crack side walls was conducted by energy dispersive X-ray analysis incorporated in the Nova 200 FIB system to verify no dissolution occurring at crack walls lying within the un-dealloyed parent phase and give more evidence of grain boundary crack penetration across the dealloyed layer into the un-dealloyed parent phase. The analysis was conducted preferentially along milled crack walls.

First, suitable cracks were chosen for FIB milling. After confirmation of the crack penetration across the dealloyed layer, a special fiducial mark using FIB milling technique was put around the crack to help locate the crack easily for the composition analysis. Then, the specimen was fractured through dynamic loading to further open the cracks and then conduct compositional analysis along the grain boundary crack walls.

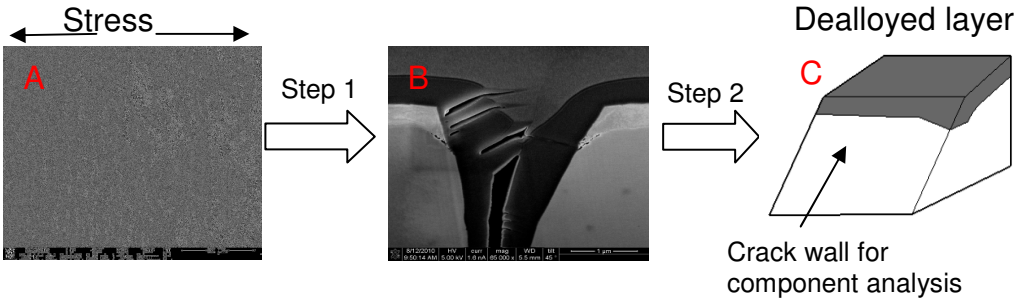


Figure 2.6. Flow chart of component analysis on cracks that penetrate through the dealloyed layer. A- Crack chosen for FIB milling. B- FIB milled crack cross section to confirm crack penetration across dealloyed layer. C- Sketch of opened crack walls for compositional analysis.

## 2.2 Dynamic Fracture in Monolithic NPG

Dynamic fracture experiments of monolithic crack-free NPG were performed in air (specimen in a dry state) and electrolyte through both 3-point bending and uni-axial tension under low displacement rate loading. The dynamic fracture of crack free NPG is discussed in two major parts: bending tests and tension tests. For both tests, preparation and handling of pre-notched crack free nanoporous gold is one of the most important experimental issues. Two methods were used to put notches in AgAu alloy samples: End milling and Electrical discharging machining technique (EDM). The end milling method yields a ~250 um wide notch and was only used for dynamic fracture experiments in air. The EDM method used 30 um wire and can generate a ~30-50 um wide notch; therefore EDM was used for most tests. The Phantom high speed digital camera was used to observe crack propagation and measure crack propagation speed.

### 2.2.1 Preparation of Crack Free NPG

As reported by other researchers (*60*, *83*), crack free NPG can be prepared through constant potential dealloying methods at low dealloying current density. In order to obtain crack-free NPG there are two essential requirements: no residual or external stress applied on the specimen and low dealloying rates. In this research, crack free NPG was prepared by dealloying AgAu alloy at very low current density (~1 $mA/cm^2$) under constant potential control (1.2 V vs NHE) in 1M $HNO_3$ .

First, the polarization behavior of Ag-28%Au alloy in 1M $HNO_3$ was examined by potential dynamic scan to determine appropriate dealloying potential. The annealed specimen for polarization test was rectangular shape, 1.5 cm ×0.5 cm×0.06 mm and prepared in the same way for dynamic scan as the crack injection experiment. The dynamic scan was run in a standard three-electrode cell, with one counter electrode of platinum wire and one standard mercury-mercury sulfate reference electrode. The scan rate for potential dynamic scan was 5 mV/s.

Based on the polarization curve, at 1.16 V (vs. standard hydrogen electrode), the dealloying current density was ~ 1 $mA/cm^2$. Two potentials were examined for preparation of crack free NPG: 1.16 V and 1.2 V. To avoid any stress, a Au thin film (deposited by electron beam on mica) was used as a substrate for samples (1.0 cm ×0.2 cm×0.06 mm) and very thin gold wire was wound around the sample in order to provide good electrical contact. Dealloying was complete when the current decayed to a few $\mu A$ $cm^{-2}$. Figure 2.7 shows the experimental setup used to determine dealloying potential for preparation of crack free NPG samples. This setup has also been used to prepare monolithic NPG in the following tensile tests using the micrometer controlled vise. For bending tests, NPG samples were dealloyed in the specially designed detachable cell, which is described in detail below.

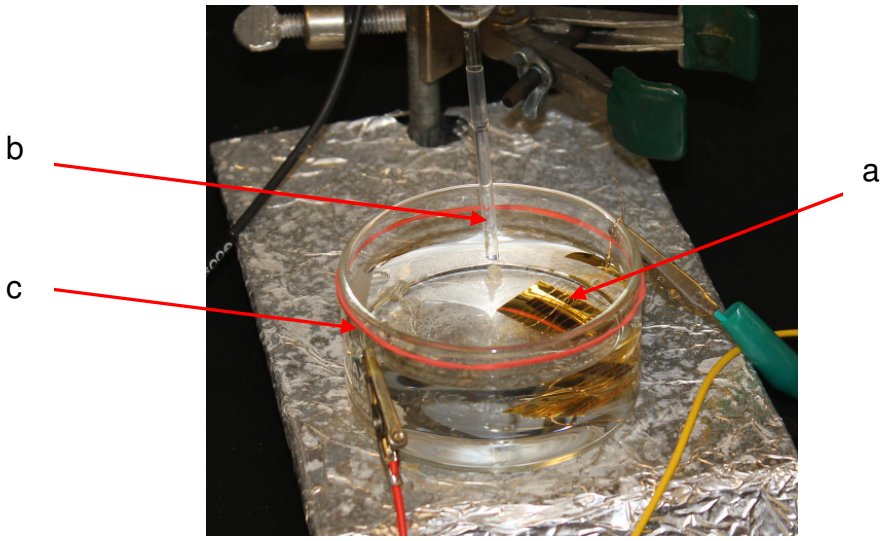


Figure 2.7. Experimental set-ups for determination of dealloying potential to prepare crack free NPG samples. a - AgAu sample on Au thin film as working electrode; b- MSE reference electrode; c- Pt wire as counter electrode.

The NPG sample after dealloying process was then soaked in nanopure water for over 1 hour to remove residual acid in the nano-pores, and then dried in air for 24 hours to let the porous structure coarsen up and become less brittle for subsequent tests. The NPG surface was examined with SEM to check the integrity of the structure and its composition was examined with EDS. These samples were then carefully mounted on to the test jig for corresponding bending and tensile tests.

### 2.2.2 Dynamic Fracture in Air

#### 2.2.2.1 Bending Tests in air

The Phantom v12.1 complimentary metal-oxide-semiconductor (CMOS) camera was used for study of the dynamic fracture of nanoporous gold for both bending and tensile tests. It incorporates a proprietary CMOS imaging sensor. This CMOS sensor allows us to capture 6242 frames per second at a maximum resolution of 1280x800 and 1000000 frames per second at reduced resolution (128 x 8) with 20 um per pixel size. For bending tests, the bottom surface of NPG sample is examined in dynamic fracture, so an inverted Nikon 2000 optical microscope was used together with the high-speed digital camera. With the assistance of the microscope at 40x magnification, the camera can capture features to 0.5 um. This insures reasonably precise crack velocity measurements. The higher the magnification of the inverted microscope, the clearer the sample bottom surface and the higher the resolution (lower of camera rate) required to increase the field of view. In the dynamic fracture experiments, the field of view should include whole sample width to observe crack propagation, therefore the magnification of inverted microscope and camera resolution or camera rate needs be balanced to observe crack propagation with highest accuracy and fast frame rates. The camera recording rate is determined by camera resolution, which also determines each image size. The quantity of images recorded at different resolutions is determined by the camera memory and each image size.

Another important parameter for the velocity measurement is the number of post trigger images. When the camera is started, it starts to record images but all these recorded images are not saved in the camera until it is triggered. The total post trigger images determine the number of images to be saved after the instant that camera is triggered and therefore the pre-trigger images to be saved based on camera memory. Because crack propagation is fast by the time the naked eye observes the occurrence of crack motion in the computer window screen the crack propagation event has already completed. To ensure capturing the whole crack propagation process, the number of post trigger images is usually set to be small and most of images recorded before triggering of camera are saved. If crack was estimated to be too fast, the post trigger images can be set to be 1, so almost all images that occur before triggering camera will be saved.

The whole experimental setup for the acquisition of crack propagation images during bending tests is shown in Figure 2.8. In this system, the light signal from specimen is first transmitted through an inverted microscope to CMOS camera and then changed to an electronic signal, which is recorded by the camera. In the connected computer system, the recorded information is then converted into images for further study.

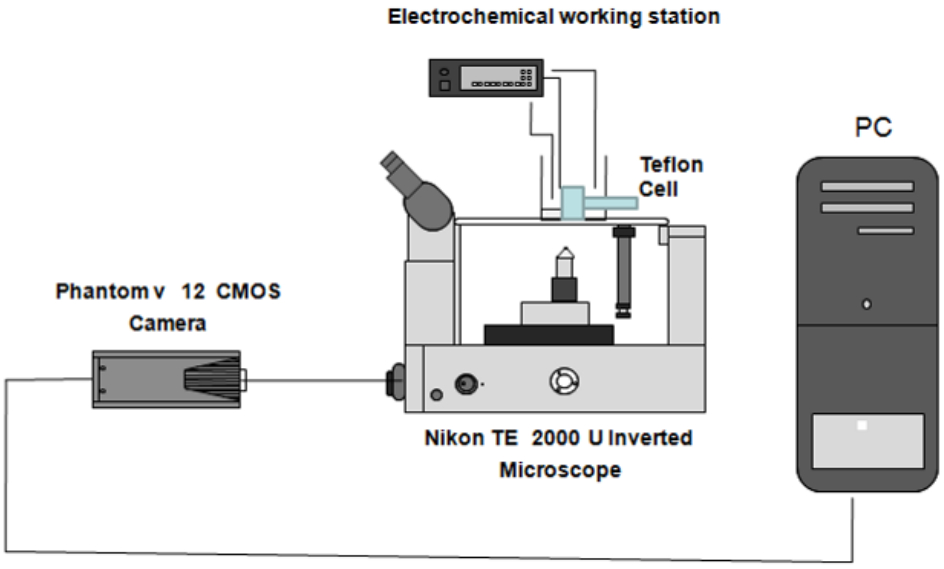


Figure 2.8. Basic experimental setup for dynamic fracture of NPG in bending

In the above experimental setup, a special Teflon cell (as shown in Figure 2.9) was designed to conduct bending tests on monolithic crack-free NPG samples. This cell is composed of 5 parts: main Teflon cell body, detachable internal cell with 10 mm internal diameter and 3 trenches milled inside, a plastic plate used to hold Teflon cell body, a stainless steel rod for load application which is threaded into the Teflon cell. Additionally a stainless steel wedge was slid into the cell along trench 3 and held by the stainless steel rod. This wedge was used to contact the sample and insure uniform bending across the sample width. In the detachable cell, two “1 by 1” millimeter trenches along the inner cell wall were used to center and hold the NPG sample in the middle of the cell. The screw rod

with 0.5 mm pitch threads was used to displace the wedge and apply load to the test specimen.

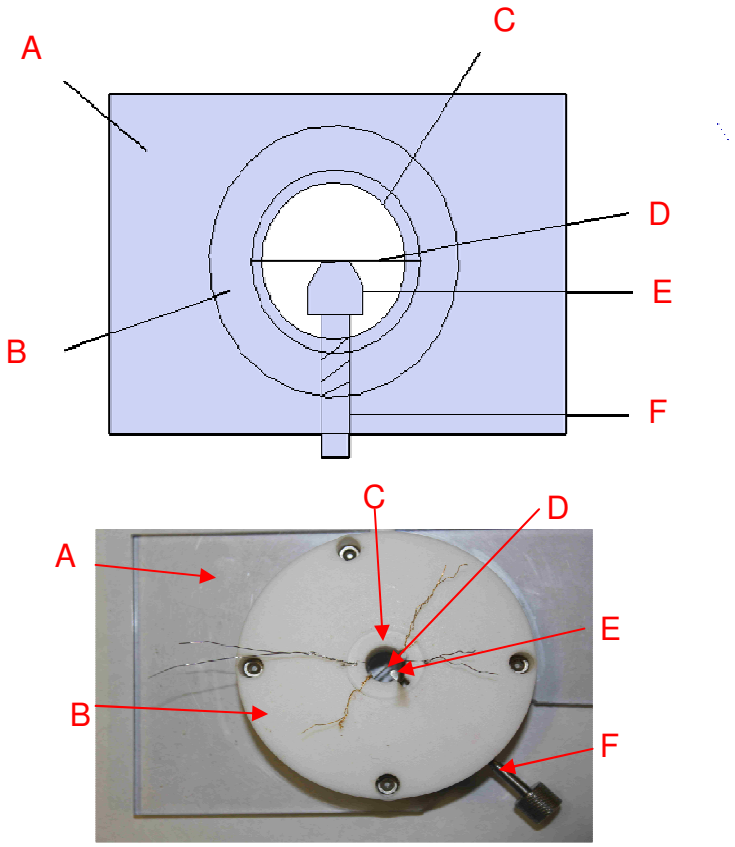


Figure 2.9. Sketch and photograph of straining and dealloying Teflon cell for bending tests. A- Plate for holding teflon cell. B- Main teflon cell body. C- Detachable internal teflon cell. D- Test specimen. E- Stainless steel wedge F- Stainless steel rod used to screw in the stainless steel wedge.

Pre-notched bending specimens with nominal dimensions 3 mm (width) x 12 mm (length) x 256 um in thickness were EDM cut from the original Ag-28at%Au sheet. End milling was first used to generate rectangular notch on one side surface of specimens for bending tests in air. The notch on test specimens (Figure 2.10) with width of 260 um extended across the 3 mm width of the specimen to a depth of ~ 30-40 um.

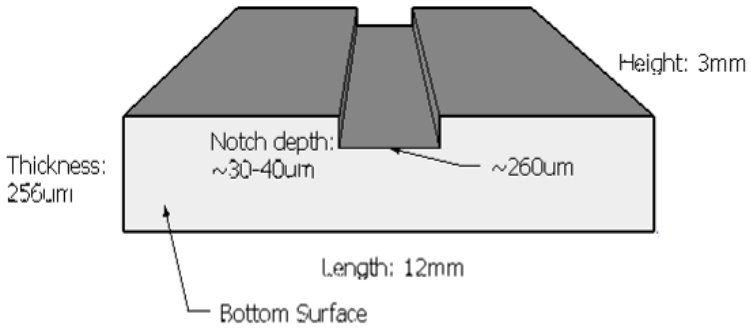


Figure 2.10. Sketch of pre-notched AgAu alloys for bending tests in air.

These notched specimens were mechanically polished at bottom surfaces as described in Table 1, ultrasonically cleaned in acetone for 20 minutes and then annealed in air at 900 $^{o}$C for 24 hours to completely remove any residual stress. Due to the special Teflon cell for bending test, these fully annealed specimens were dealloyed in the detachable cell to prepare crack-free monolithic NPG samples and avoid direct handling of these samples. As shown in Figure 2.11, the specimen was carefully slid into trench 1 and 2 with 0.005" Au wires wound around for electrical conduction. Pt wires were made into rectangular shape and used to hold the specimen from sliding out of the Teflon cell. The specimen in the Teflon cell was then dealloyed at 1.16 V (NHE) until potential dropped to a few uA, rinsed with deionized water and dried in air for 24 hours as described above. Before transferring the Teflon cell into the main Teflon body, the platinum wire was removed and Teflon cell was held horizontally and pushed slightly into the main Teflon body with 0.13 mm thick cover

glass attached by carbon tape to the bottom of the cell body. The trench 3 in the detachable cell was aligned in the same line of the stainless steel rod so that the screw rod can also be screwed into the detachable Teflon cell.

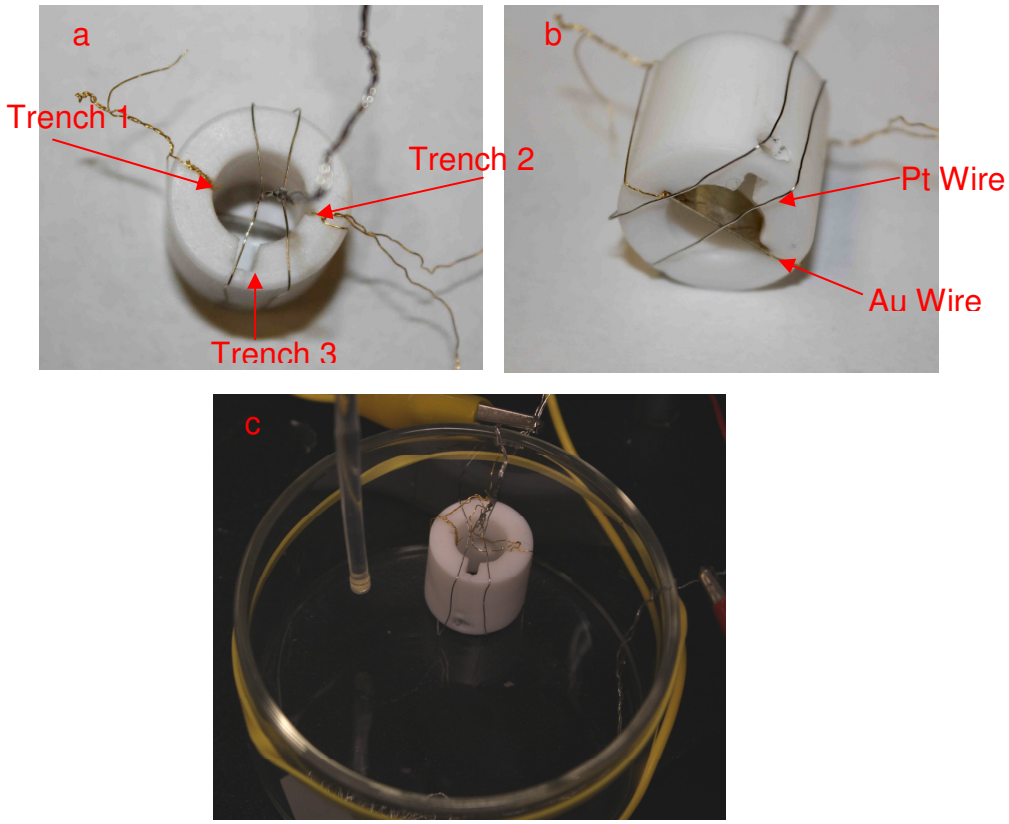


Figure 2.11. Loading Strategy of fully annealed Ag-Au alloy specimens in the detachable Teflon cell for electrochemical dealloying.

After the stainless steel wedge was slid along trench 3 into the internal Teflon cell, the screw rod was rotated across the main Teflon body into the detachable Teflon cell until mating with the stainless steel wedge. The stainless steel wedge was held tightly during screwing the stainless

rod into it. The whole Teflon system was then transferred to the stage of inverted microscope. To completely include the 260 um wide notch, whole sample thickness and also give some buffer space for stainless steel wedge in the computer image window, the magnification of the microscope was set at 4X and the camera resolution was set at 128 by 96 (corresponding to 4.34 us per frame) for the velocity measurement. The post trigger images were set at 4000 and total saved images in camera at this resolution was 417,177. The camera resolution, corresponding camera rate and total images camera saves and post trigger images set for the dynamic fracture experiments of NPG are included in Table 2.2.

Table 2.2 Detailed camera parameters employed in dynamic fracture of NPG samples

| Dynamic test type | Camera Resolution | Camera Speed | # of images saved in camera | # of Post-trigger images |
|---|---|---|---|---|
| Bending tests in air | 128×96 | 4.34 | 417177 | 4000 |
| Bending tests in electrolyte | 128×32 | 1.91 | 1042944 | 4000 |
| Tensile tests in air and electrolyte | 208×48 | 3.45 | 417177 | 1 |
| | 208×64 | 4.34 | 347648 | 1 |

After adjusting the cell position on the stage and the arrangement of the light source (fiber optic dual gooseneck lighting system) so as to get the most ideal image of the bottom surface, the whole Teflon cell was then taped on to the microscope stage. To initiate a crack in the sample, the stainless steel wedge was slowly screwed into the sample by controlling the stainless steel rod and the camera was triggered right after

observation of sample being fractured along EDM notch. Most of the images (413,177 images corresponding to 1.8 s) before triggering of camera were saved and crack initiation only occurred microseconds earlier than triggering of camera, so the whole crack propagation process was completely saved in camera. After the experiment, the saved images were replayed for detection of crack initiation and then selected images were stored on the computer. Two tests under same conditions were run to obtain the crack propagation process. In this test, used camera speed was faster than the crack propagation speed. Therefore precise crack propagation speed was calculated as the following equation 2.2:

$$V = \frac{L}{v} \qquad (2.2)$$

$V$ -- Crack propagation speed; $L$ --Crack propagation length within each frame; $v$ --camera frame rate

The fracture surfaces of the test specimens were examined with SEM.

2.2.2.2 Tensile Tests in air

In order to significantly increase the sample dimension over which we could measure crack velocity we also employed tensile specimens of order 4 mm in width. This sample configuration is also more consistent with geometries assumed in theoretical analysis of dynamic fracture. For these test we employed a top-view binocular microscope with magnification ranging from 0.65 to 5 X. The monolithic NPG samples contained a 800 um deep notch. A micrometer controlled steel vise was

designed to load tensile stress. This vise is mainly composed of three parts: a stationary stage, a movable stage and micrometer. The top surfaces of the two stages were ground to be flat and at the same height. Figure 2.12 shows the sketch of the whole test system.

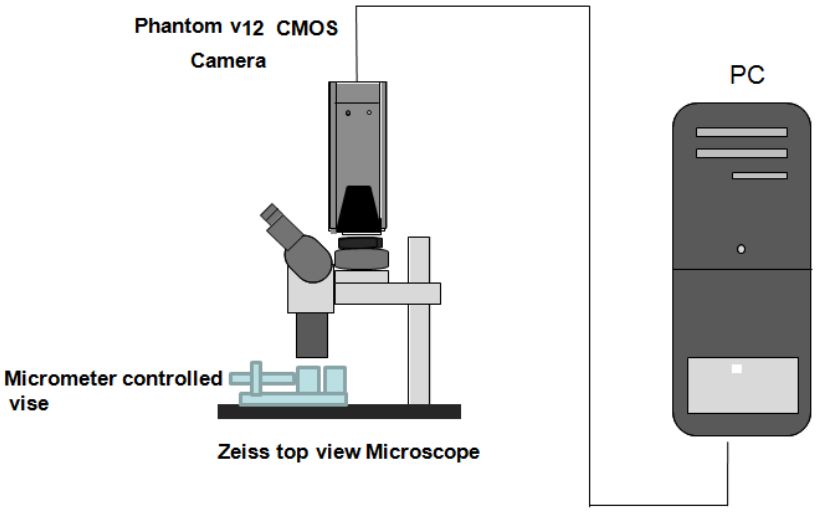


Figure 2.12. Basic experimental setup for dynamic fracture of NPG in tensile tests.

For tensile tests in air, AgAu alloy specimens of nominal dimensions 4 mm (width) x 1 cm (length) x 130 um in thickness were cut from original 127 um thick Ag-28at%Au sheet. A 30-50 um wide and 800 um deep notch was cut along the width direction with a 30 um EDM wire. These specimens were mechanically polished on the side surfaces (as shown in Figure 2.13) as mentioned in Table 1, ultrasonically cleaned in acetone and then annealed in air in the same way as that for bending test specimens. Crack free NPG specimens were prepared from these pretreated AgAu specimens as described in section 2.2.1. After the

specimens were dried in air for 24 hours, they were epoxy-glued at both ends onto the stages with around 3 mm gap in between. EDM notch was in the middle of the gap and aligned perpendicular to the micrometer. The only concern that we had using this test protocol relates to potential cracking of the specimen within the glued regions. In this regard ancillary experiments and SEM characterization were performed with a variety of glue types. Test results showed that epoxy glue only caused a few cracks around the glue region during the cure time (around 20-30 minutes) and was chosen for our tensile tests. After epoxy glue cured and hardened for over 30 minutes, the vise was placed under the top view optical microscope for the tensile test. Because sample width is extended from 256 um to 4 mm compared to the bending tests, the magnification of microscope was set at 1X to increase the field of view. Meanwhile EDM notch was decreased from 260 um to 50 um and the camera resolution was set at 208 x 64 (corresponding to 4.34 us per frame) for the velocity measurement. The image length for the sample increased but the image width decreased, therefore the camera rate still remained at the same value for this test. Owing to the expected faster crack propagation post trigger images were set to 1. The sample was fractured by quick rotation of the micrometer and the camera was triggered right after the observation of the crack in the computer. The fracture surface of the test specimens were examined with SEM.

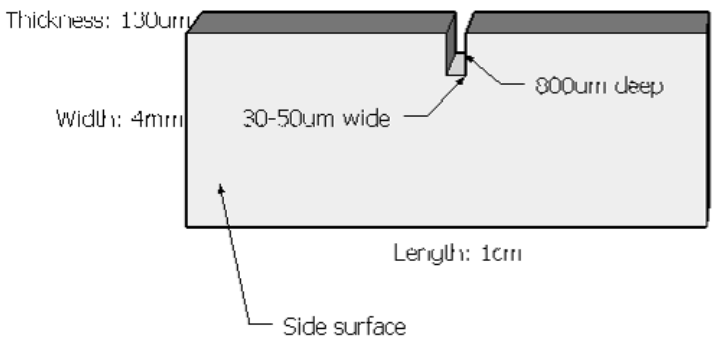


Figure 2.13. Sketch of pre-notched AgAu alloy for tensile test in air. Side surface was mechanically polished.

### 2.2.3 Dynamic Fracture in Electrolyte

Dynamic fracture of monolithic crack free NPG was also conducted in electrolyte under potential control to study how electrochemical potential affects dynamic fracture.

#### 2.2.3.1 Bending Tests in Electrolyte

We employed the same experimental setup as shown in Figure 2.8 for bending test of NPG specimens in electrolyte. The initial end milling method used for bending tests in air to put a notch on AgAu specimens generates too wide a notch and limits the camera speed that can be used, as higher crack velocities under potential control were expected. Therefore, test specimens for bending tests in electrolyte were EDM notched with much narrower wire (~30 um) to provide a 30-50 um wide and 50 um deep notch. The specimen dimension and the dealloying strategy to make crack free NPG were the same as that in bending test in

air. After dealloying of the AgAu specimen the Teflon cell was taken out of the electrolyte, rinsed with DI water, then carefully transferred to the main cell body, which was sealed at the bottom with 0.13 mm thick cover glass. 1M $HNO_3$ + 0.001M $AgNO_3$ was used as electrolyte and was put into the detachable cell until the sample was fully immersed. The electrolyte was made from reagent level of 70% concentrated nitric acid and silver nitrate. The whole Teflon cell system was placed on the inverted microscope stage and a voltage of 1.20 V (NHE) was applied to the NPG sample. The total time for the NPG after dealloying was stopped and before the potential was applied was around 30 minutes. The magnification of the inverted microscope was set at 4X. With a much narrower notch, the resolution of the camera is decreased to 128 by 32 with camera rate being increased to 1.91 us/frame**.** The total number of images that could be saved was 1,042,944. The post trigger images were also set at 4000. The crack initiation and image capture process was the same as that in the bending tests in air. The potential of silver wire reference electrode was measured in comparison with MSE before and after the tests. Its potential drifted by ~ 1 mV within one hour. After the crack speed measurement, the specimen was taken out of electrolyte, rinsed with DI water. The fracture surface and pore size was examined with SEM. The total time after removal of potential control and before SEM examination was around one hour. Equation 2.1 was also used to calculate crack propagation speed.

2.2.3.2 Tensile Tests in Electrolyte

Tensile tests under potential control in electrolyte were run to examine dynamic fracture of NPG. Various potentials have been examined for this study. The same experimental setup as the tensile test in air was employed. In addition, a rectangular Teflon cell was designed to work as an electrochemical cell that was mounted between the two stages of the steel vise. Figure 2.14 shows the sketch of this experimental configuration.

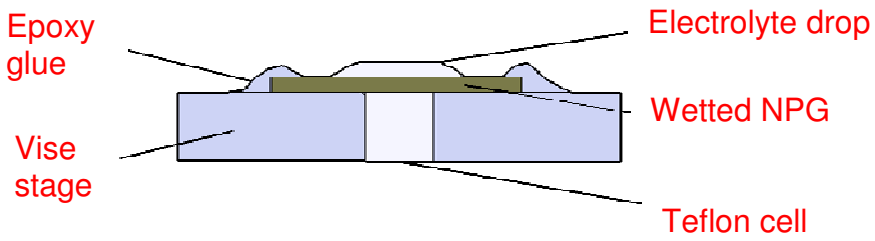


Figure 2.14. Sketch of how nanoporous gold being arranged on micrometer controlled vise and wetted by electrolyte.

In this scheme, the samples were imbibed with electrolyte as shown in Figure 2.14. Before conducting tensile tests, cyclic voltammetry between 0 V and 1.5 V (NHE) were run on NPG and Au thin film samples in order to confirm that the test protocols resulted in samples fully imbibed with electrolyte. Test conditions were as follows:

1. Au thin wire was wound around Au thin film for electrical conduction and the thin film was fully immersed in 1M $HClO_4$.

2. NPG being fully immersed and wetted in 1M $HClO_4$ (electrolyte used for tensile tests) in a glass beaker.
3. After this the NPG specimen was cleaned with de-ionized water, dried in air and then glued on the vise stages and wetted as in Figure 2.14.

The result obtained from test 2 gave the current potential behavior for fully wetted NPG specimens. Both test 1on NPG and test 2 on Au thin film gave the reference to detect whether NPG sample on vise is fully wetted or not. Test 3 was to verify that NPG specimens were fully imbibed using the method shown in Figure 2.14.

The designed Teflon cell is 1cm wide and has the same height and length of the vise stage. Due to the extra width of the cell, the length of the tensile test specimens was increased from 1cm (in air test) to 2 cm. AgAu specimen dimension (except length), notch dimension, pretreatment, dealloying and post treatment of nanoporous gold were the same as those used in tensile tests in air. The electrochemical setup for this study was a three electrode system with the NPG sample as the working electrode, a platinum wire as counter electrode and a hydrogen loaded palladium electrode as reference electrode. 1M $HClO_4$ as electrolyte was made from reagent level of 70% $HClO_4$ and de-ionized water. 0.05" diameter palladium wire was first cleaned as other experiments, then was loaded with hydrogen in 0.1M $H_2SO_4$ in a three electrode cell, in which the Pd wire served as the working electrode with a Pt wire works counter

electrode and MSE as reference electrode. Around 1.5 cm of Pd wire length was loaded with hydrogen. Hydrogen loading (*84*) was done at constant current density (-0.03 mA/cm$^2$) for 40mins and then unloaded at 0.03 mA/cm$^2$ for 250 seconds. The Pd/H electrode was held in electrolyte for over 8 hours until its potential became stable and varied within less than 0.5 mV per hour. Then this electrode was then rinsed with nanopure water and put into the Teflon cell. To prevent free corrosion of the steel vise loading device, the top and side surfaces of the vise stages were sealed with black tape. Half filled and with reference and counter electrodes inside, the Teflon cell was held tightly in between the vise stages. A dry NPG specimen was then epoxy-glued on to the tape fixed to the stages with EDM notch centered in the Teflon cell. After the epoxy hardened, a narrow 0.005" thick Au foil for electrical connection of NPG was attached by taping both its ends with double-sided carbon tape (as shown in Figure 2.15). After the position of vise and light source were adjusted to obtain the best imaging conditions, the Teflon cell was filled with electrolyte until the top surface of NPG was covered by electrolyte (as shown in Figure 2.14). After ~ 30 minutes wetting, a prescribed potential was applied to the sample and then the sample was loaded following the same protocols as that used for the air tests. The corresponding camera speeds and test potentials used are listed in Table 2.3. For all these tests, post trigger images were set to 1. The side surfaces and fracture surfaces

of the test specimens were selectively examined with SEM. Crack propagation speed was also calculated based on equation 2.1.

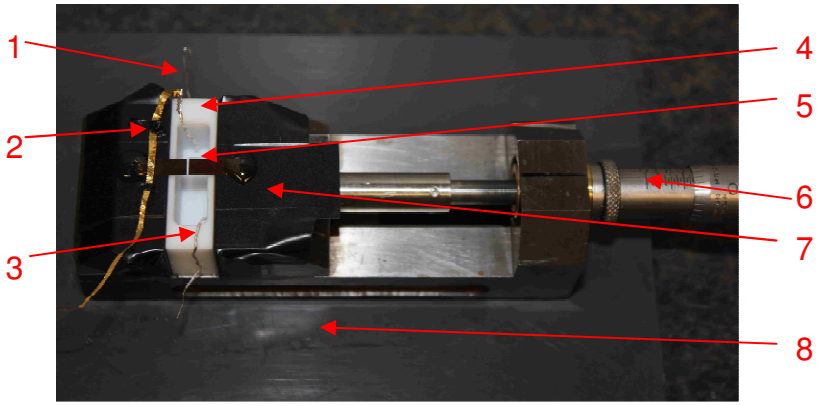


Figure 2.15. Photograph of vise setup for tensile tests in electrolyte. 1: Pt wire as counter electrode. 2: Au foil for electrical conduction of NPG. 3: Pd/h electrode as reference electrode. 4: Teflon cell as electrochemical cell. 5: NPG specimen glued on the stages. 6: Micrometer. 7: Carbon black tape sealed stages. 8: Plastic holder with a slot to hold the vise

Table 2.3 Camera parameter and potential applied on NPG specimens for tensile tests in electrolyte.

| Test No | Potential applied on NPG V(vs NHE) | Camera Resolution | Camera Speed |
|---|---|---|---|
| 1 | 1.4 | 208×48 | 3.45 |
| 2 | 1.2 | 208×64 | 4.34 |
| 3 | 1.0 | 208×48 | 3.45 |
| 4 | 0.7 | 208×64 | 4.34 |
| 5 | 0.5 | 208×64 | 4.34 |

# Chapter 3

# RESULTS AND DISCUSSION

The following is a presentation of the results for crack injection experiments on pre-dealloyed Ag-31at %Au alloys in 0.1M $AgNO_3$ electrolyte by dynamic tensile loading and hand bending methods. The degree of crack penetration across the dealloyed layer into undealloyed bulk was measured with high resolution SEM for both methods. The transition of composition from dealloyed layer to undealloyed bulk along crack walls has been quantified with EDX. Dynamic fracture of monolithic NPG both by 3-point bending and tensile loading methods has been studied and velocity measurements were made on the specimens in air and in electrolyte with potential control. Mechanical stress to fracture NPG samples in air was measured by Tytron tensile test device.

## 3.1 Crack Injection Experiments

### 3.1.1 Electrochemical Dealloying

Potententiodynamic scans were performed on Ag-31at%Au in air saturated 0.1M $AgNO_3$ solution with Mercury/Mercurous Sulfate reference electrode and a platinum wire as a counter electrode. Specimens were heat treated at 900 $^0$C for 24 hours prior to testing. Two scans were conducted and the detailed polarization behavior is shown in Figure 3.1. All potentials have been reset to the standard hydrogen electrode (NHE).

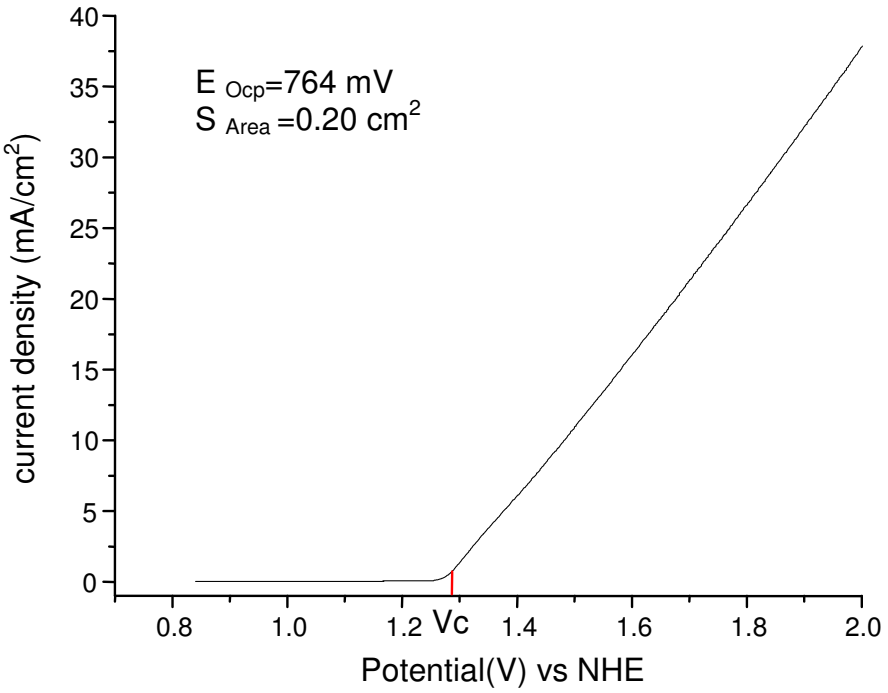


Figure 3.1. Potentiodynamic scan of Ag-31at%Au in 0.1M $AgNO_3$. Vc is the critical potential of the sample dealloyed in 0.1M$AgNO_3$. Here we use the current density of 1 mA/cm$^2$ to define Vc. Scan rate was 10 mV/s

The critical potential, above which a sharp current increase occurs signaling the initiation of bulk dealloying, is defined here as the potential with the current density of 1 mA/cm$^2$ and is approximately 1.28 V vs NHE. Based on the polarization curve, the dealloying potential for stress corrosion cracking tests was chosen at 1.8 V vs SHE. At such a high potential, very fine porosity can be produced and was more favorable for crack injection into un-dealloyed bulk materials during tensile loading and bending tests.

### 3.1.2 Crack Injection

#### 3.1.2.1 Dynamic Tensile Loading

For this set of tests, dealloying and fracture of samples were in the same teflon cell (as shown in Figure 3.1). The initial protocol was to dealloy specimens to a prescribed depth and then fracture them in the electrolyte after removal of applied potential for various period of time in the cell. In these tensile tests, three out of six samples fractured before the prescribed dealloying time was reached. A small tensile load of around 13 MPa (clip +cell +rod +solution) was on the sample during the dealloying process because the side screws on both clips were too loose. One sample ruptured after 20 seconds while being dealloyed, one after 34 seconds and another at 90 seconds. All the fracture surfaces were intergranular (as shown in Figure 3.2A). The sample that fractured at 20 seconds was FIB milled on some cracks close to the fracture surfaces and crack penetration was detected through the dealloyed layer into the bulk alloy (Figure 3.2B). The bulk dealloying depth was around 200-300 nm and the dealloying penetration along the grain boundary (GB) was within 2-3 times that of the bulk dealloying depth. The crack penetration into the undealloyed region was over 10 times that of grain boundary dealloyed depth.

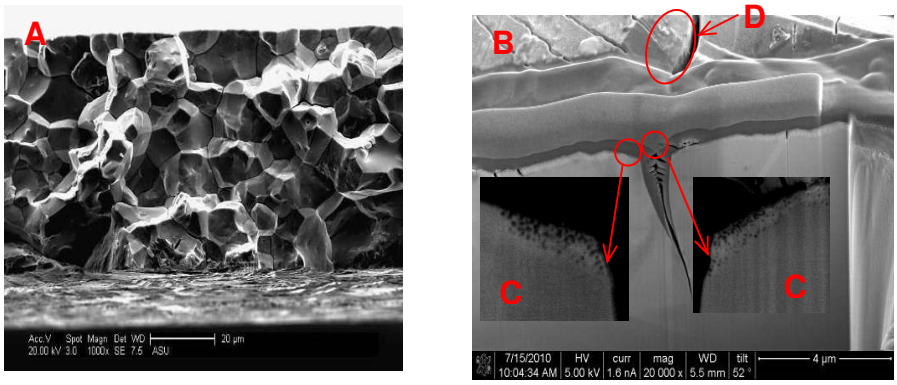


Figure 3.2. Fracture surface and milled crack cross-section of the sample that ruptured at 20 seconds during dealloying in the tensile cell. A- SEM image of the intergranular fracture surface. B-Full view of FIB milled cross section of one crack close to the fracture surface. C- Magnification of dealloyed regions close to crack walls, showing clear separation between the dealloyed layer and un-dealloyed bulk as well as crack penetration across the dealloyed layer. D- Top view of the milled crack.

The other three samples were fractured as predesigned in the experimental protocol, i.e. samples were dealloyed for prescribed time (20 s and 40 s), then were aged in the teflon cell for 5 s to 90 s and impact fractured by a 1-kg weight. One sample was dealloyed for 20 s and aged for 5 s in electrolyte. The fracture surfaces show intergranular fracture at both edges and ductile fracture in the middle of the sample. The other two samples were dealloyed for 40 s and one was aged for 15 s and the other one for 90 s. The fracture surfaces of the sample aged for 15s were intergranular, while for the sample aged for 90 s, fracture surfaces displayed intergranular at the edges and ductile failure in the middle. The FIB result on the sample that was dealloyed for 40 s and aged for 90 s shows that the bulk dealloying depth was around 400 nm and dealloying

along GB was within 2-3 times of bulk dealloying depth. No dealloying penetration across the dealloyed layer into un-dealloyed bulk (Figure 3.3) was observed on the selected two cracks for FIB milling.

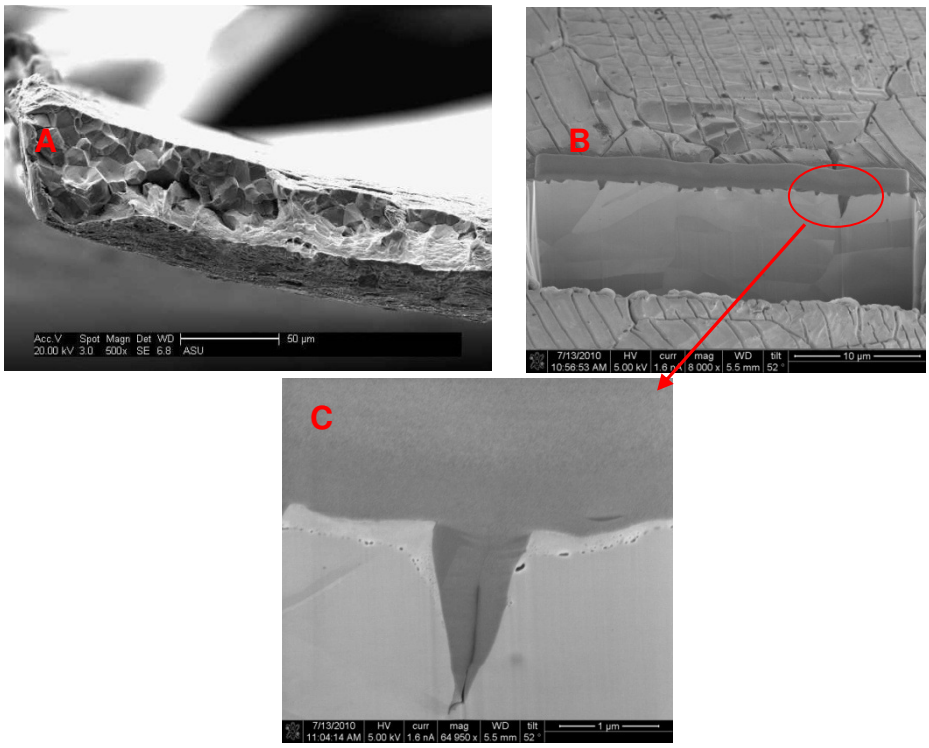


Figure 3.3. Fracture surface and milled crack cross-section of the sample dealloyed for 40 seconds and impact fractured after being aged for 90s in the teflon cell under no potential control. A- SEM image of fracture surface showing intergranular fracture at one end and ductile fracture in the middle. B-Full view of FIB milled cross section of cracks close to the fracture surface. C- High magnification of crack cross section shown in image B, showing no obvious crack penetration across deallloyed layer along GB into bulk.

In summary, 4 out of 6 experiments using the tensile loading method displayed intergranular fracture surfaces. Although one of the two FIB milled crack cross sections indicates no crack penetration, only one FIB

milling was conducted for that sample and more cracks should be carefully selected for further analysis.

Due to inflexible aging time of dealloyed sample and failure of decoupling of stress and dealloying in the dynamic tensile loading experiments, bending tests by hand was chosen to be an alternate method for crack injection.

3.1.2.2 Hand Bending

Five experiments with different coarsening times in different environments were tried to study the ability of the fine nanoporous structure to inject cracks. After bending, all samples were rinsed with DI water, dried in air and annealed at 200 $^{0}$C for 10 minutes in air to allow for coarsening to facilitate the identification of dealloyed layers around cracks. The detailed dealloying and aging parameters are listed in Table 3.1

Table 3.1 Dealloying and aging parameters for hand bending tests

| Test # | $E_{Dealloying}$ (V vs NHE) | Dealloying time (second) | Film thickness (um) | Aging Environment | Aging time |
|---|---|---|---|---|---|
| 1 | 1.8 | 80 | ~0.8-2.2 | Electrolyte at OCP | 60s |
| 2 | 1.8 | 55 | ~1.4-2.1 | Electrolyte at OCP | 130s |
| 3 | 1.8 | 45 | ~1.5-1.9 | DI water | 5minutes |
| 4 | 1.8 | 40 | ~0.6-1.1 | Air | 15minutes |
| 5 | 1.8 | 50 | ~0.9-1.2 | DI water and Air | 1.5hours |

OCP: open circuit potential

For all the test samples, the FIB milling results showed that the dealloyed layer thickness was not completely uniform and preferential dealloying occurred along grain boundaries, which may be caused by silver segregation.

In test 1and 2, samples were aged in the electrolyte after being dealloyed. For test 1, three open intergranular cracks (from plane view SEM, Figure 3.4) were chosen for FIB milling. The dealloyed porous layer showed obvious different contrast from the substrate. The cross section images at high magnification demonstrated clearly that the three cracks initiated in the dealloyed porous region penetrated through the dealloyed layer along grain boundaries deeply into the un-dealloyed parent phase and then arrested. The penetration depth was around 6 times that of the dealloyed layer.

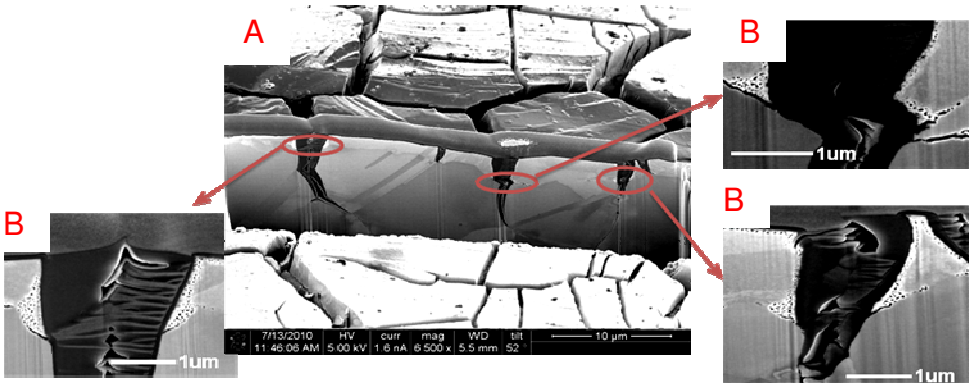


Figure 3.4. Cracked Ag-31 at%Au by hand after being dealloyed at 1.8 V vs NHE in 0.1M $AgNO_3$ for 80 seconds and aged in solution for 60 seconds at OCP. Cracks penetrated into un-dealloyed bulk alloy ~ 6 times the dealloyed depth. A-FIB milled cracks cross section. B- Magnified dealloyed regions close to crack walls, showing clear separation between the dealloyed layer and un-dealloyed bulk and crack penetration across the dealloyed layer.

In test 2, the specimen was aged in dealloying solution at open circuit potential for 130 seconds**.** Film induced cracking was also observed on the milled crack, which penetrated into the un-dealloyed bulk ~ 8 times the dealloyed depth (Figure 3.5).

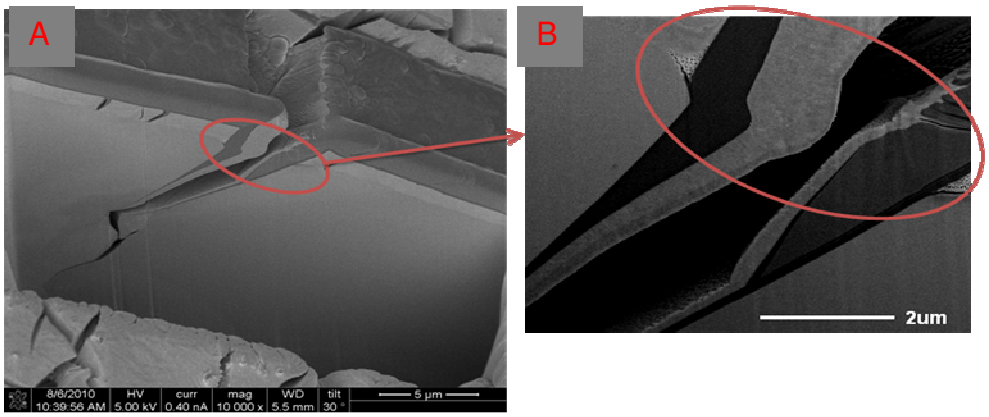


Figure 3.5. Stress cracked Ag-31 at%Au by hand after being dealloyed at 1.8 V vs NHE in 0.1M $AgNO_3$ for 55 seconds and aged in solution for 130 seconds at OCP. Cracks penetrated into undealloyed bulk alloy as high as around 8 times of dealloyed depth. A-FIB milled cracks cross section. B-Magnified dealloyed regions close to crack walls, showing clear separation between the dealloyed layer and undealloyed bulk and crack penetration across the dealloyed layer.

In test 3 and test 4, the specimens were aged out of the electrolyte. One was aged in DI water for 5 minutes and test result is shown in Figure 6.6. Cracks penetrated into un-dealloyed bulk alloy ~ 3 times the GB dealloyed depth. The aging environment for test 4 was in air for 15 minutes. Figure 3.7 shows the FIB analysis result. Cracks penetrated into the un-dealloyed bulk alloy at ~6.5 times that of the GB dealloyed depth. Aging in DI water and air completely excludes the possibility of stress assisted cracking by completely removing the sample from the dealloying electrolyte.

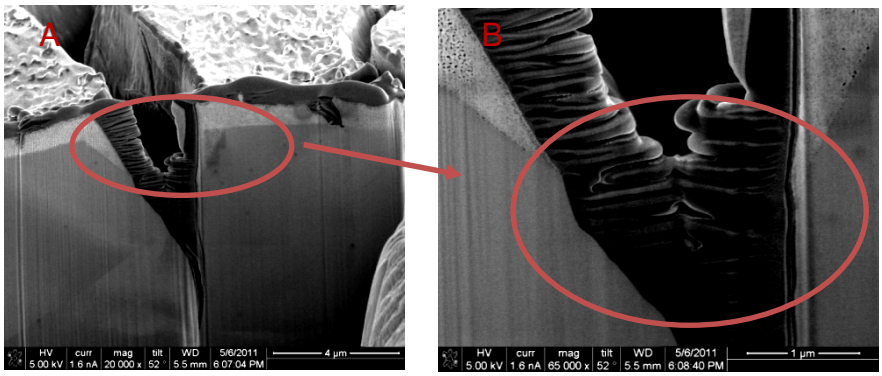


Figure 3.6. Stress cracked Ag-31 at%Au by hand after being dealloyed at 1.8 V vs NHE in 0.1M $AgNO_3$ for 45 seconds and aged in deionized water for 5 minutes. Cracks penetrated into undealloyed bulk alloy as high as around 3 times of GB dealloyed depth. A-FIB milled cracks cross section. B- Magnified dealloyed regions close to crack walls, showing clear separation between the dealloyed layer and undealloyed bulk and crack penetration across the dealloyed layer.

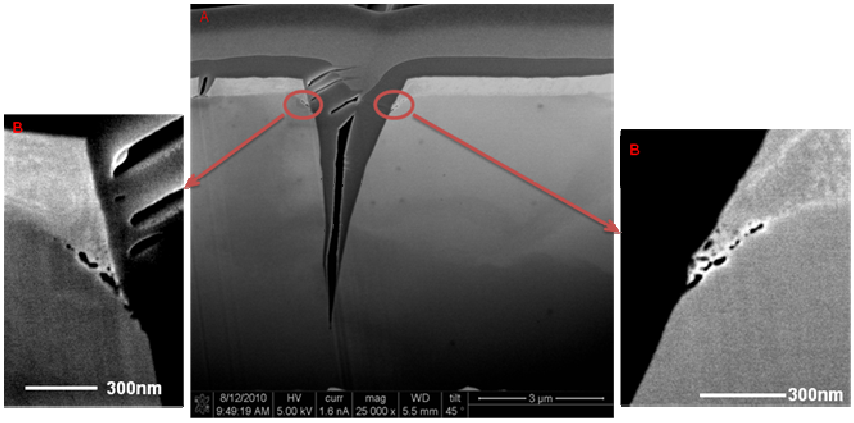


Figure 3.7. Stress cracked Ag-31 at%Au by hand after being dealloyed at 1.8 V vs NHE in 0.1M $AgNO_3$ for 40 seconds and aged in air for 15 minutes. Cracks penetrated into undealloyed bulk alloy as high as around 6.5 times of GB dealloyed depth. A-FIB milled cracks cross section. B-Magnified dealloyed regions close to crack walls, showing clear separation between the dealloyed layer and undealloyed bulk and crack penetration across the dealloyed layer.

In test 5, the specimen was aged out of electrolyte in DI water for 30 minutes and then in air for 1 hour prior to hand bending. Several cracks were FIB milled and one of the FIB milling results is shown in Figure 3.8. Due to such a long time aging in air, the dealloyed layer lost the ability to inject cracks into the undealloyed layer and cracks arrested within or close to the dealloyed/un-dealloyed boundary along grain boundaries.

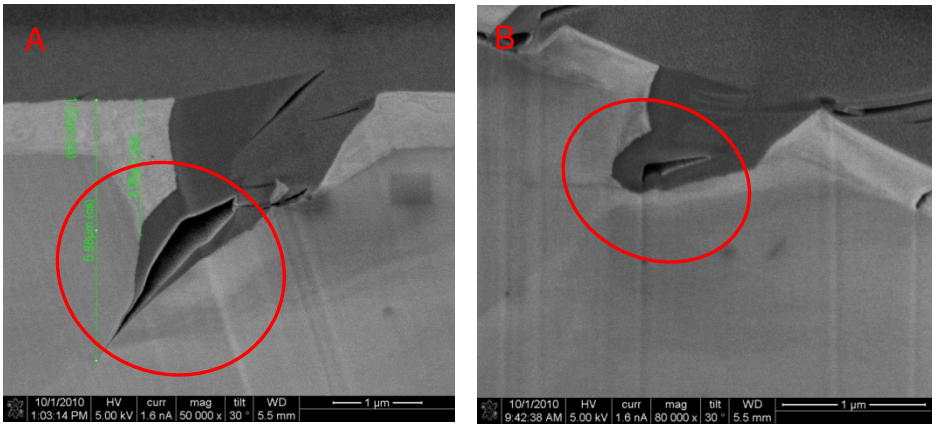


Figure 3.8. Stress cracked Ag-31 at%Au by hand after being dealloyed at 1.8 V vs NHE in 0.1M $AgNO_3$ for 50 seconds and aged in DI water for 30minutes and in air for 1 hour. Cracks stayed within the dealloyed layer along grain boundaries. A-FIB milled cross section for crack a. B- FIB milled cross section for another wide open crack. Both milled crack cross sections show that crack stayed close to the dealloyed layer along grain boundaries.

A summary of the above tensile loading and five bending experiments is given in Table 3.2:

Table 3.2 Detailed experimental parameters for tensile loading and hand bending experiments which proved film induced cracking phenomenon

| Test # | Crack injection method | Aging method | Film thickness (um) | GB dealloying depth (um) | Crack arrest distance in bulk(um) |
|---|---|---|---|---|---|
| 1 | Constant loading | Fractured as being dealloyed for 20s | ~0.2-0.3 | ~0.4 | ~4 |
| 2 | Bending | 60s in electrolyte at OCP | ~0.8-2.2 | ~1.3-2.5 | ~3.8-10.3 |
| 3 | Bending | 130s in electrolyte at OCP | ~1.4-2.1 | ~2.3-5.2 | ~8.4-15.6 |
| 4 | Bending | 5mins in DI water | ~1.0-1.9 | ~2.9-5.3 | ~4.5-13 |
| 5 | Bending | 15mins in air | ~0.6-1.1 | ~1-2.3 | ~6.6-7.1 |
| 6 | Bending | 30mins in DI water and 1 hour in air | 0.9-1.2 | ~1.5-4 | ~2-5.5 |

Under both conditions that stress and dealloying process is coupled or decoupled, we observed that a thin layer of nanoporous layer can inject cracks into the un-dealloyed ductile parent phase. Several previous studies were also aimed at demonstrating crack injection into the parent phase f.c.c alloy from a nanoporous layer (*21*, *22*, *27–29*, *85*). Most of these studies were performed on polycrystalline alloys and crack injections were reported to be predominantly intergranular. In most of these studies, while crack injection was demonstrated, there is still an important lingering issue related to GB dealloying penetration. How can we exclude that the cracks travel through already dealloyed GB? One answer to this question is that crack injection into the parent phase is not observed after the sample was held to coarsen nanoporous layer for too long a time (over 30 minutes). In our experiments, high magnification images of crack penetration into parent alloy was provided for samples

with dealloying and stress being decoupled for less than 20 minutes. Long enough aging times resulted in the inability of the dealloyed layer to inject the crack. This should not be the case if crack injection was occurring only through weakened dealloyed grain boundaries in the parent phase. Measurements of the depth of GB dealloying and crack injection distances have provided important new direct evidence for this process. The inability of the long hold-time tests to inject cracks is a direct result of the coarsening process in the nanoporous gold layer. The ligaments coarsen during hold and if the ligaments get too large the layer is no longer brittle enough to inject a crack (*49*).

There are limitations to both the tensile and bending tests. The design of the tensile cell apparatus was not totally successful in decoupling stress and dealloying. The small level of stress resulted in the occurrence of a real stress-corrosion cracking process. In the bending experiments, test samples experienced tensile stress on the top side surface and compressive stress on the bottom side surface. The dynamic crack experiences deceleration entering the compressive side of the sample thus affecting crack penetration distance. We would expect much deeper crack penetrations under tensile loading .To successfully conduct such tests the design of the apparatus should be changed. A cell similar to that used for the dynamic fracture of monolithic NPG under potential control would be recommended for future experiments. As silver is deposited on counter electrode during dealloying of AgAu alloy samples, the Teflon cell

should be designed to ~ twice or three times longer than the one used for dynamic fracture of NPG samples. Also to ensure the sample is fully immersed in electrolyte, the top part of the Teflon cell should be designed to be the shape as shown in Figure 3.9. The central flat part is as high as the vise stage and samples will be glued on the vise across the flat portion of the cell. Owing to capillary effects, the sample across the cell will be fully covered by electrolyte. After samples are dealloyed for a prescribed time, they can be aged within the electrolyte at open circuit potential or in DI water or in air for different times to study aging effect of nanoporous layer on crack injection.

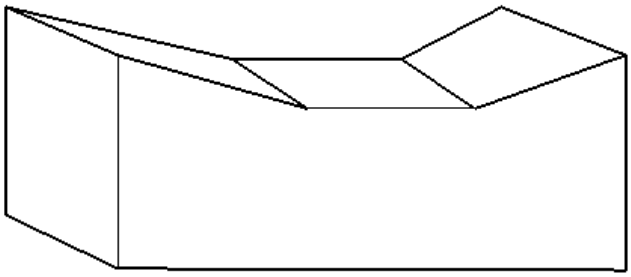

Figure 3.9. Sketch of Teflon cell for future crack injection experiments with micrometer controlled vise. The length of the cell can be twice or three times of the previously designed cell for dynamic fracture of NPG. The height of central flat part and width of the cell is the same as the previously used cell.

3.1.3.3 Composition analysis along crack walls using the analytical microscopy

The FIB milling results have shown that intergranular cracks penetrated across the dealloyed layer into un-dealloyed bulk both by tensile loading and in hand bending. In order to give more solid support to the crack injection phenomenon, the samples, which were aged in electrolyte for 130 seconds, in DI water for 5 minutes and in air for 15 minutes, were conducted energy dispersive X-ray analysis with the function of line scan analysis along the side crack walls.

For the sample that was aged in electrolyte for 130 seconds, EDX composition analysis (shown in Figure 3.10) was conducted on the same FIB milled crack and showed good consistency with the milling result. One of the milled crack cross-sections showed that the dealloying depth within grains was around 2 um and dealloying penetration depth at GB was around 5 um. For the same intergranular crack which was widened by dynamic loading, the EDX line analysis along one of the crack walls showed that the bulk dealloyed layer is enriched in Au. Sharp composition transition, corresponding to the beginning of GB dealloying penetration, starts from around 2 um and stops at around 4.5 um. The dealloying penetration depth varies at different positions of grain boundaries. The deviation of dealloying penetration depth of EDX analysis and FIB milling results may be due to this reason. Across the composition transition, the

EDX analysis result shows the composition along the line is around 65-70 at% Ag, which is very close to un-dealloyed bulk composition (69 at% Ag).

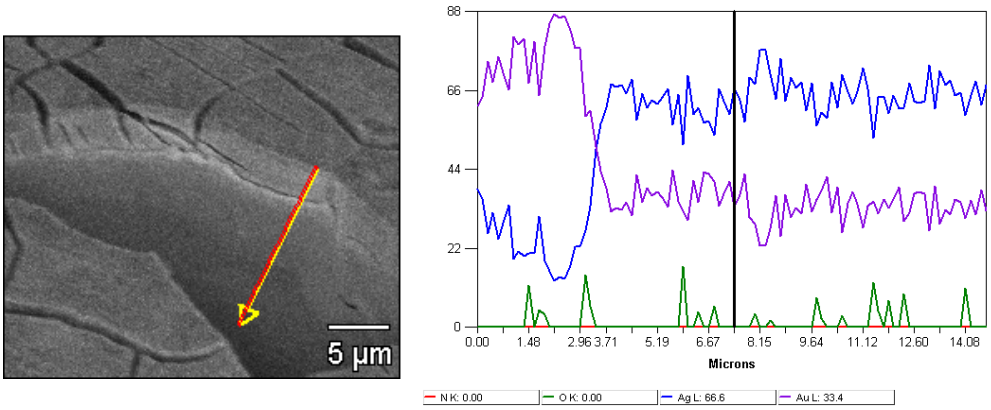


Figure 3.10. Energy dispersive X-ray line analysis of a specimen of Ag-31 at% Au that was dealloyed under stress-free conditions in 0.1M $AgNO_3$ at 1.8 V for 55 seconds, aged in electrolyte for 130 seconds without potential control and then bent by hand. The left image is the scanning electron micrograph of the crack, which was FIB milled firstly to detect crack penetration, then loaded to be more open. The arrowed line shows the EDX analysis path. The plot on the right represents the atomic composition along the line in the left SEM image. The purple curve gives the Au composition and blue gives the Ag composition. The top dealloyed layer is Au enriched. The composition given at the bottom of the right figure corresponds to the position marked by the black vertical line in the figure.

For the sample that was aged in DI water for 5 minutes, the position of the crack for EDX analysis is very close to the FIB milled position. The EDX composition analysis (shown in Figure 3.11) also showed good consistency with the FIB milling result, which indicated the bulk dealloyed layer was around 1um and the GB dealloying penetration was around 3um. In the EDX analysis result, the top dealloyed layer is Au rich and sharp

composition transition starts from around 1um and stops at around 2.5 um. The composition of the intergranular crack walls across the transition (around 67-70 at %Ag) is very close to the un-dealloyed bulk alloy (69 at %Ag).

When we conducted EDX analysis on the sample that was aged in air for 15 minutes after being dealloyed, the crack chosen for the EDX analysis (Figure 3.12) was not the initial milled crack, which did not widen to enough of an extent to alloy for EDX analysis. The FIB milling result on one crack was that the bulk dealloyed layer was 0.6 um and the GB dealloying penetration was around 1 um deep. The EDX analysis result on another wide open crack showed a sharp composition transition starting from 1.3 um to around 2.7 um. The composition of the intergranular crack walls across the transition region is also close to that of undealloyed alloy

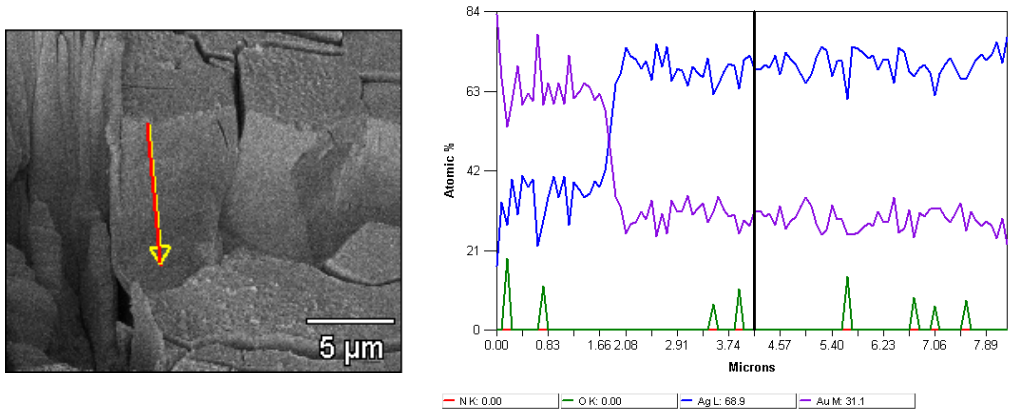


Figure 3.11. Energy dispersive X-ray analysis of a specimen of Ag-31 at% Au that was dealloyed under stress-free conditions in 0.1M $AgNO_3$ at 1.8 V for 45 seconds, aged in deionized water for 5 minutes and then bent by hand. The left image is the scanning electron micrograph of the crack, which was FIB milled firstly to detect crack penetration, then loaded to be opened. The arrowed line shows the EDX analysis path. The graph on the right shows the atomic composition along the line in the left SEM image. Purple curve gives the Au composition and blue curve gives the Ag composition. The top dealloyed layer is Au riched. The composition given at the bottom of the right figure corresponds to the position marked by the black vertical line in the figure.

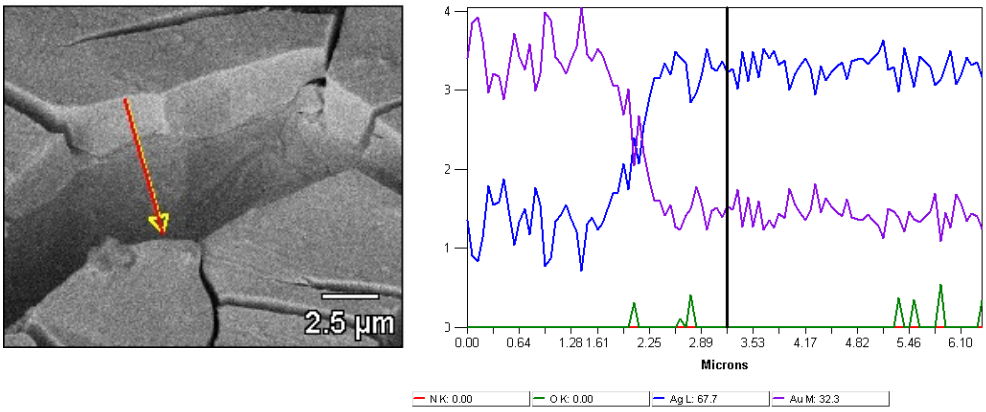


Figure 3.12. Energy dispersive X-ray line analysis of a specimen of Ag-31 at% Au that was stress free dealloyed in 0.1M $AgNO_3$ at 1.8 V for 40 seconds, aged in air for 15 minutes and then bent by hand. The left image is the scanning electron micrograph of the crack, which was further opened by dynamic loading and used for EDX analysis. The arrowed line shows the EDX analysis path. The right figure represents the atomic composition along the line in the left SEM image. Purple curve gives the Au composition and blue curve gives the Ag composition. The top dealloyed layer is Au enriched. The composition given at the bottom of the right figure corresponds to the position marked by the black vertical line in the figure.

The above EDX analysis on hand bent samples displayed a compositional transition along opened crack walls. However, one limitation of the above experiments is that side crack walls were only partially opened and EDX analysis was not conducted completely down to the bottom of the opened cracks. One solution to the above limitation is to use dual beam FIB to section samples for compositional GB analysis by scanning transmission electron microscopy (STEM). Orientation-imaging microscopy (OIM) can be used to identify the boundary types that may be particularly susceptible to crack injection and FIB sectioning can be used to prepare un-dealloyed samples for subsequent EDX analysis by STEM.

The GB compositions of virgin samples will be used as a control for comparison to similar sections cut from cracked boundaries following crack injection experiments. Additionally, 50 – 100 nm thick cross sections of cracked grain boundaries could be milled and the fracture surfaces examined using the JEOL ARM 200 aberration-corrected STEM for high-resolution compositional analysis of GB dealloying.

FIB techniques have been used by several researchers for preparing electron transparent cross-sections of SCC crack tips (*86*)**.** Among available established methods, the “lift out” technique seems most suitable for our proposed work. Figure 3.13 briefly describes this technique and shows how we can characterize GB dealloying with STEM in a crack injection event. The dissolution front penetrates down a GB, meanwhile dealloying also evolves along directions normal to the boundary into the matrix. As shown in Figure 3.13b, there will be a concentration gradient of Ag (Au) in to the matrix adjacent to either side of the boundary with qualitative features (compare to Figure 3.7). Such an important feature of GB dealloying will allow us to precisely determine the GB dealloying depth and compare it to the depth of crack injection. This behavior is analogous to that occurring in GB diffusion; however, no solid-state mass transport process operation is involved in this dealloying situation. Z-contrast high angle annular dark field imaging (Figure 3.13b, black arrow) will be used to fully visualize the interfacial structure immediately adjacent to the opened (crack-injected) and unopened GB. EDX with nm-scale resolution

will be used to characterize the composition gradients normal to the opened (cracked) boundary more precisely and the analysis result will be compared to similar characterization along the un-opened boundary immediately ahead of the arrested crack.

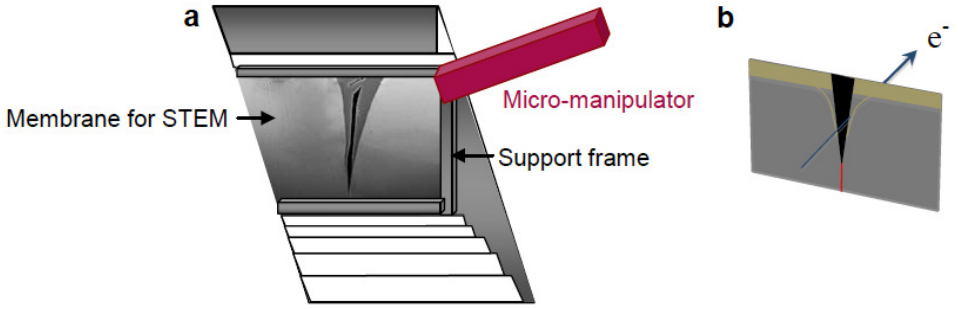


Figure 3.13. a FIB-milled preparation of cross-section of intergranular crack penetration for STEM examination; crack injection distance~10um; Step trenches are milled on both sides of the ~100 nm-thick electron transparent membrane cross-section. A thick support frame structure is maintained in order to prevent deformation of the membrane during lift out and subsequent handling. A micro-manipulator is Pt-'welded" to the membrane and the membrane section is finally FIB-cut to be fully detached. b. FIB-sectioned electron transparent membrane (~50-100 nm thick) containing the cracked GB for aberration corrected STEM analysis and showing a rendering of surface and GB dealloying. The gold line profiles from both grain boundaries indicate the degree of dealloying that has penetrated from dealloyed GB layer to the grain interior. EDX will be used to map out the AgAu concentration profiles along atomic columns on either side of the opened boundary as well as the un-cracked region of the boundary (red line).

## 3.2 Dynamic Fracture in Monolithic NPG

### 3.2.1 Preparation of Crack Free NPG

Preparation of crack free monolithic NPG samples was performed by dealloying Ag-28 at% Au alloys in 1M $HNO_3$ using a chronoamperometry method. Polarization behavior of Ag-28 at% Au alloys was evaluated to obtain the critical dealloying potential for preparation of crack free NPG. The surfaces of the as prepared NPG samples were examined with SEM to check for cracks in the nanoporous structure. EDX analysis was also employed on these NPG samples to measure the composition and determine the degree of dealloying in these samples.

As mentioned in the experimental section 2.2.1, Ag-28 at% Au samples were heat treated prior to the potential dynamic scans. As shown in Figure 3.14, the critical potential was1.16V versus NHE. Based on the obtained polarization curve, 1.16V and 1.2V were examined in chronoamperometry for preparation of crack-free NPG. Very thin gold wires were wound around the samples (1.0 cm ×0.2 cm×0.06 mm) fixed to a Au thin film substrate in order to insure good electrical contact while presenting any spurious loading of the sample. The dealloying current density was initially stable at values tested in the polarization scan and as the dealloying process continued the current density decayed. Obvious current drop signaled dealloying penetration of bulk thickness and current dropping to a few microamperes indicated fully dealloyed samples. The top surface of the dried NPG samples was examined with SEM. Both

dealloying potentials gave porous structures and pore sizes i~30-40 nm after 24 hours aging in air. SEM images of NPG samples dealloyed at 1.2 V are shown in Figure 3.15. Compositional analysis using energy dispersive X-ray spectroscopy (EDX) shows a silver composition, of less than 5 at%. Dealloying alloy samples at 1.2 V shortens dealloying time from 53 hours (at 1.16 V) to 43 hours. Therefore, preparation of crack free NPG was chosen at 1.2 V for dynamic fracture tests on NPG samples.

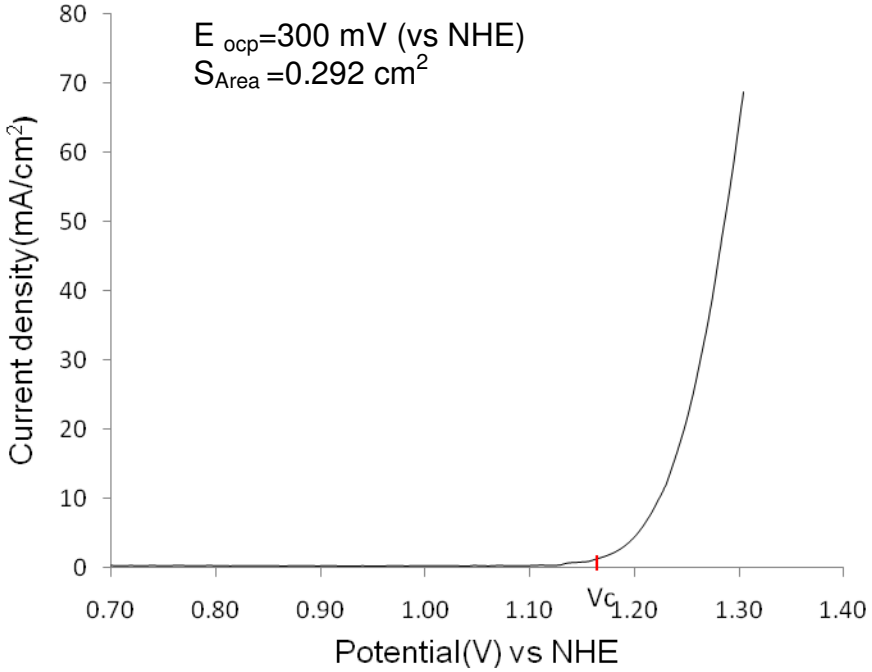


Figure 3.14. Potential dynamic scan of Ag-28 at %Au in 1M $HNO_3$. Vc - the critical potential of the sample dealloyed in 1M$HNO_3$. Here we use the current density of 1 mA/cm$^2$ to define Vc. Scan rate was 5 mV/s.

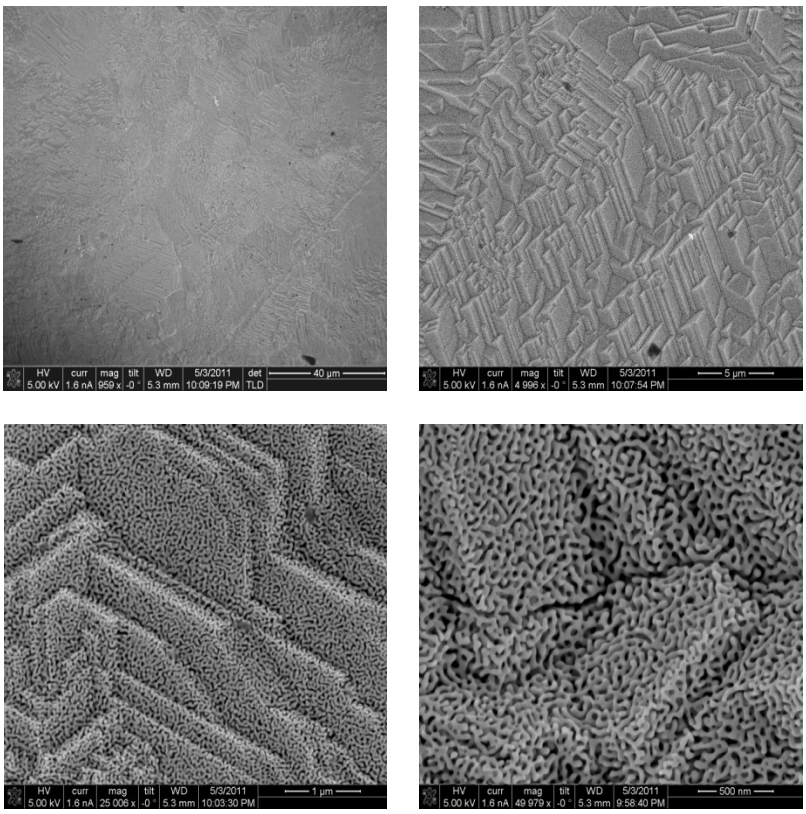

Figure 3.15. Top surface of NPG sample dealloyed at 1.2 V vs NHE for around 47 hours in 1M $HNO_3$ and aged in air for 24 hours. No obvious cracks were found along grain boundaries.

Owing to the special design of the Teflon cell for bend tests, the samples were dealloyed in a detachable Teflon cell with dimension of 3 mm (width) x 1.2 cm (length) x 256 um (thickness) and both sides of dealloyed samples were equally exposed to electrolyte. During dealloying, samples were held vertically in the Teflon cell and barely in contact with a Au wire.

In tensile tests in electrolyte, the sample length was twice that of samples used for the tensile tests in air. During dealloying of these longer

samples both ends of samples were observed to gradually tilt up (warp) in the middle of dealloying process and gradually went back to ~flat as samples were dealloyed through the whole depth. For dealloying of shorter (around 1 cm long) samples on Au thin film, tilting of both ends was not observed. Tilting of longer samples indicated small amount of stress existing in the as-dealloyed samples. All the samples for tensile tests in electrolyte were dealloyed at a constant potential of 1.2 V and the current density dropped from around 1 $mA/cm^2$ to a few $uA/cm^2$. To avoid tilting of longer samples during dealloying process, one solution may be galvanostatic dealloying with dealloying current density below a few hundreds $uA/cm^2$. Much lower dealloying speed would help prevent residual stress forming during dealloying process with much slower dissolution rate of silver.

3.2.2 Dynamic Fracture in Air

3.2.2.1 Bending Tests in air

The feasibility of monitoring dynamic fracture in monolithic NPG samples has been firstly examined by performing 3-pt bending tests in air in the specially designed Teflon cell, which is compatible with an inverted optical microscope configured with the high speed digital camera (phantom V12.1). NPG samples with dimensions 3 mm (width) x 1.2 cm (length) x 256 um (thickness) were dried in air for 24 hours before the tests. Fracture surfaces were examined with SEM to study the fracture mode. Several tests were repeated under the same conditions to obtain

reliable terminal velocity. The detailed bending tests on monolithic NPG samples were performed as outlined in the experimental section 2.2.2.1.

Monolithic NPG samples were observed to support dynamic fracture for the bending tests in air. Figure 3.16 shows results from one of the bending experiments in air. In this test, cracks were all initiated at one edge of end milled notch. The crack propagation process from the bottom surface was recorded in 6 successive images at a camera rate of 4.34 us/frame. The lens for the inverted microscope was set at 4X therefore the crack length in each frame was calculated from the following equation:

$$L = \frac{\sqrt{P_x^{\,2} + P_y^{\,2}} \times p}{M} \qquad (3.1)$$

where L is the crack length within each frame; $P_x$, the pixel number along x; $P_y$, the pixel number along y; p the real dimension, and $M$ the magnification of the lens used in microscope. The error in calculating the crack length results form an ambiguity in determining the extent of the crack in each image. Because of the high frame rates used accurate crack propagation distances and accordingly crack speeds within each frame could be determined. The crack propagation speed was calculated as equation 2.2.

Generally for these experiments, the crack attained an apparent terminal velocity of 7-10m/s (sample to sample variation) to a crack length of ~160 um or about 0.8 of the sample thickness. The final fracture of the sample occurred at higher velocities, in the range of 30-50 m/s (shown in

image e to f). The results of crack propagation during bending tests are shown in Table 3.3 and corresponding crack length and crack velocity behavior is plotted in Figure 3.17.

The fracture surfaces examined with SEM are shown in Figure 3.18. The ligament size of monolithic NPG after 24 hours drying is usually around 40 nm. Often the crack plane remained planar and the fracture path transgranular. However, in several experiments instances of intergranular fractures were observed. In those experiments post mortem analysis indicated that crack initiation did not occur uniformly across the 3 mm width of the sample. This resulted in a mode III component to the loading that seemed to favor intergranular separation.

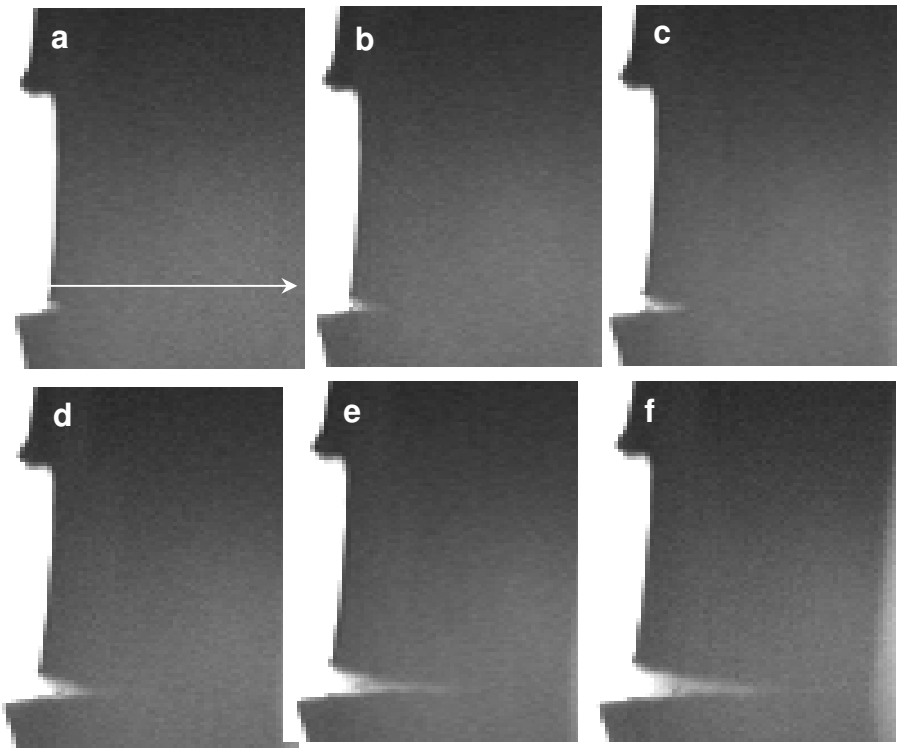


Figure 3.16. Dynamic fracture of dry NPG (0.74 volume fraction of porosity) in pure bending. Sample was dealloyed in1M $HNO_3$ at 1.2 V and dried in air for 24 hours. a – f were obtained at a rate of 4.34 us/frame. Length of white arrow in image 'a' corresponds to the 200 um specimen thickness. The notch width is also ~200 um.

Table 3.3. Results of dynamic fracture of dry NPG in pure bending. Frame number corresponds to those shown in Figure 3.16

| Frame # | Crack propagation along X (pixels #) | Crack propagation along Y (pixels #) | Crack length (um) | Velocity (m/s) | Crack Length Error(um) | Velocity error (m/s) |
|---|---|---|---|---|---|---|
| a | 2 | 0 | 10 | 2.3 | 0 | 0 |
| b | 3 | 0 | 25 | 3.5 | ±5 | ±1.15 |
| c | 4 | 1 | 45 | 4.8 | ±5 | ±1.15 |
| d | 4 | 2 | 65 | 5.2 | ±5 | ±1.15 |
| e | 5 | 1 | 90 | 5.9 | ±10 | ±2.30 |
| f | 7 | 0 | 125 | 8.1 | ±10 | ±2.30 |

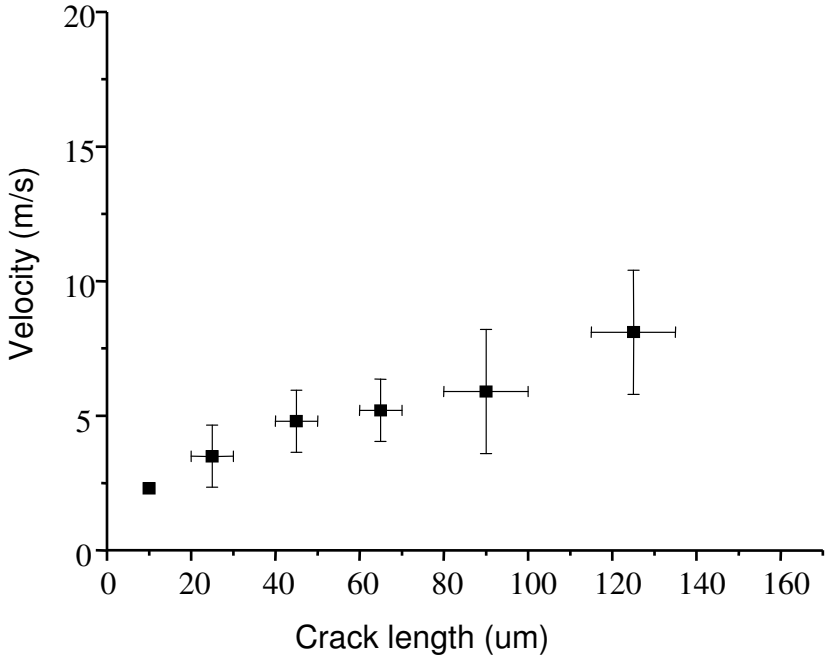


Figure 3.17. Results of dynamic fracture of dry NPG in pure bending. Crack velocity-crack length behavior indicates an apparent terminal velocity of ~ 7-10 m/s.

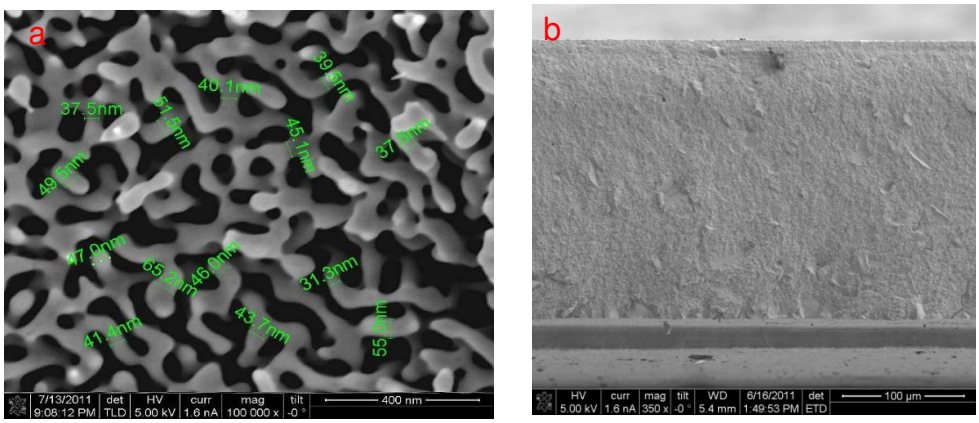


Figure 3.18. a. Nanoporous morphology of the dry NPG in pure bending showing the ligament size around 40nm. b. Fracture surface of dry NPG after pure bending test.

Previously published results have shown that the macroscopic sample behavior with large enough gold ligament size (>~100 nm) becomes ductile and unstable dynamic fracture does not occur**.** A theoretical terminal crack velocity in monolithic NPG samples can be estimated as follows. There have been several measurements of the Young's modulus of NPG similar to that used in the experiments discussed above and a reasonable value seems to be of order of 10 GPa. The density of NPG used in our experiments is estimated around 0.25 that of pure gold. Longitudinal sound velocity of NPG, $v_L$, which is equal to $(2\pi E/\rho)^{1/2}$, is therefore of about 1400 m/s. A corresponding Raleigh velocity, $v_R$, is equal to about 0.6 $v_L$ or around 800 m/s. The shear wave velocity would be 1.05 $v_R$. In conventional dynamic fracture theory, the limiting crack velocity in an elastic solid is equal to $v_R$ (*69*)**.** As the gold ligament diameter decreases, the terminal crack velocity we measure is believed to increase

dramatically because deformation to fracture becomes dominantly elastic. The above analysis is an estimation of terminal velocity in NPG by tensile loading, which is very often used in conventional dynamic fracture study. Pure bending tests were not studied as widely as tensile tests as test samples would experience compressive stress at the end of cracks. In the past, dynamic fracture of an elastic beam or plate in bending has been examined theoretically by Freund and co-workers (*87*, *88*). In their study, crack accelerates quickly to a characteristic terminal velocity for the material and decelerates in the final stages of fracture by compressive stress. The "terminal velocity" was found to be about $0.2v_L$, which would in the case of the NPG we examined correspond to about 280 m/s. While the terminal velocities measured in the above bending experiments in air are below this value, it seems likely that 40 nm length scale NPG displays too much ductility to be compared with predictions based on purely elastic constitutive behavior. The following bending tests in electrolyte under potential control gives terminal velocity of NPG at much smaller ligaments size by quench ligament coarsening with potential control shortly after dealloying.

3.2.2.2 Tensile Tests in air

Tensile loading tests in air were performed to achieve much broader dynamic fracture range of monolithic NPG samples. In addition to high speed digital camera, a top view microscope and tensile loading system based on a vise were employed for these tests. The sample was carefully

epoxied to the ends of the vise and the top polished surface with around one 800 um long notch was used for crack propagation process. Ancillary epoxy glued NPG samples were examined with SEM and only minor cracks were observed close to the epoxy glue margin area (shown in Figure 3.19). This region was not past of the sample “gage length”. Cracks propagated along sample width direction, which is perpendicular to the loading direction.

Tensile tests in air also show monolithic NPG samples support dynamic fracture process. After a crack was initiated as described in experimental part, the high speed digital camera was triggered and crack propagation process recorded. Figure 3.20 shows results of two tensile tests in air with good repeatability. At the camera rate employed for these two tests, 4.34 us/frame, crack propagation process was captured in 5 frames and rather precise crack propagation speed was obtained. Cracks were all initiated at EDM notches and followed a single path. The red arrows in each image indicate crack length. The same method as in as bending was used to calculate crack length and propagation speed.

In the tensile tests, the crack attained a much higher terminal velocity of ~150-160 m/s to crack length of 1.2 mm to 1.6 mm (sample to sample variation) or about 0.4-0.6 of the sample thickness. The final fracture of the sample at boundaries occurred at slightly lower velocities, in the range of 140 m/s (shown in images d and e). The detailed results of crack

propagation during tensile tests are shown in Table 3.4 and corresponding crack length and crack velocity behavior is plotted in Figure 3.21.

The fracture surfaces were also examined with SEM, as shown in Figure 3.22. The ligament size of NPG sample from both tests is around 35-40 nm. The crack plane also remained planar and the fracture path transgranular. The post mortem analysis indicated that crack initiation started from the EDM notch and propagated linearly across the sample width. This indicated a mode I loading. For test 2, the reason that crack propagation path is not completely parallel to EDM notch is that EDM notch on the sample was not perfectly aligned perpendicular to the loading direction.

Under pure tensile loading, NPG samples with 40 nm ligament size reach much higher constant velocity, but which is still lower than the estimated limiting crack velocity in elastic solid, which is estimated to be ~ 800 m/s. This corresponds well with the analysis of bending tests in air, i.e. 40 nm length-scale NPG displaying too much ductility to be compared with predictions based on purely elastic constitutive behavior.

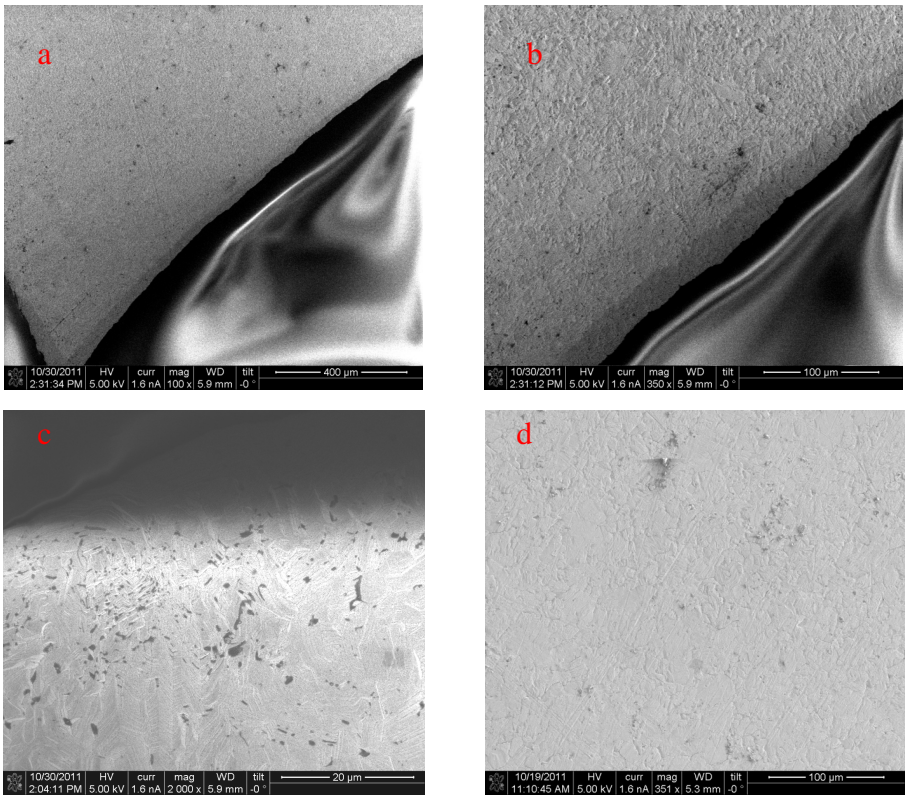


Figure 3.19. NPG surface with cured epoxy glue. Image a to c shows NPG surfaces less than 0.5 mm away from epoxy glue. Image d shows surface is over 0.5 mm away from epoxy glue. No obvious cracks formed around epoxy glue area.

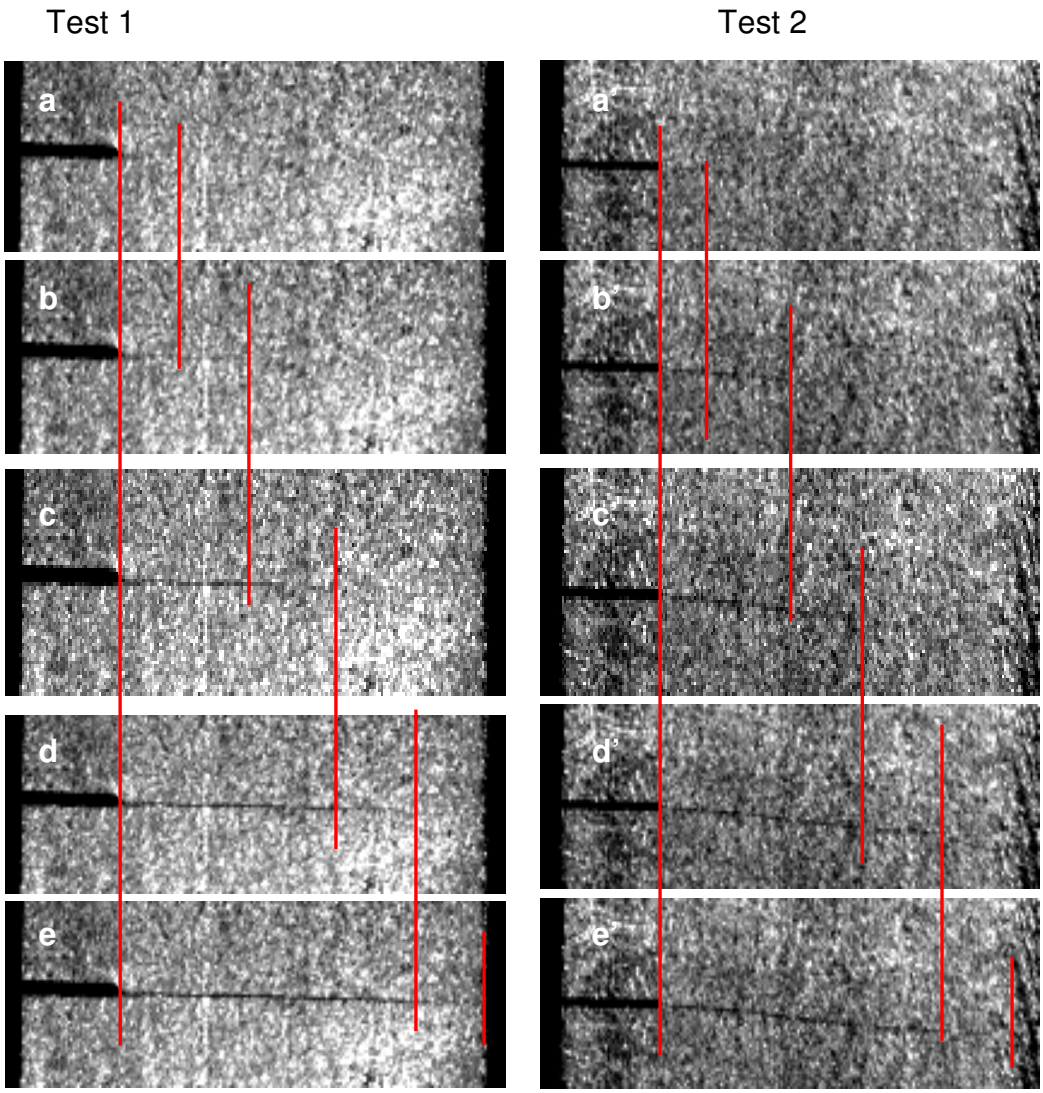


Figure 3.20. Dynamic fracture of dry NPG (0.74 volume fraction of porosity) by tensile loading. Two tests were conducted and samples were dealloyed in1M $HNO_3$ at 1.2 V and dried in air for 24 hours. Left a – e and right a'-e' were obtained at a rate of 4.34 us/frame. Pre-notch is around 800 um long and 30-50 um wide. Length of red arrow in each image corresponds to crack length. The sample width including notch is ~4 mm.

Table 3.4 Results of dynamic fracture of dry NPG by tensile loading. Frame number corresponds to those shown in Figure 3.20.

| Frame# | Crack propagation along X (pixels #) | Crack propagation along Y (pixels #) | Crack length (um) | Velocity (m/s) | Crack Length Error(um) | Velocity error (m/s) |
|---|---|---|---|---|---|---|
| a | 24 | 0 | 480 | 110.6 | ±40 | ±9.22 |
| b | 30 | 0 | 1080 | 138.2 | ±40 | ±9.22 |
| c | 36 | 0 | 1800 | 165.9 | ±40 | ±9.22 |
| d | 32 | 4 | 2440 | 148.6 | ±20 | ±4.61 |
| e | 30 | 2 | 3040 | 138.6 | ±20 | ±4.61 |
| a’ | 25 | 0 | 500 | 115.2 | ±40 | ±9.22 |
| b’ | 35 | 2 | 1200 | 161.3 | ±40 | ±9.22 |
| c’ | 31 | 2 | 1820 | 143.2 | ±20 | ±4.61 |
| d’ | 31 | 2 | 2440 | 143.2 | ±20 | ±4.61 |
| e’ | 32 | 3 | 3080 | 148.1 | ±20 | ±4.61 |

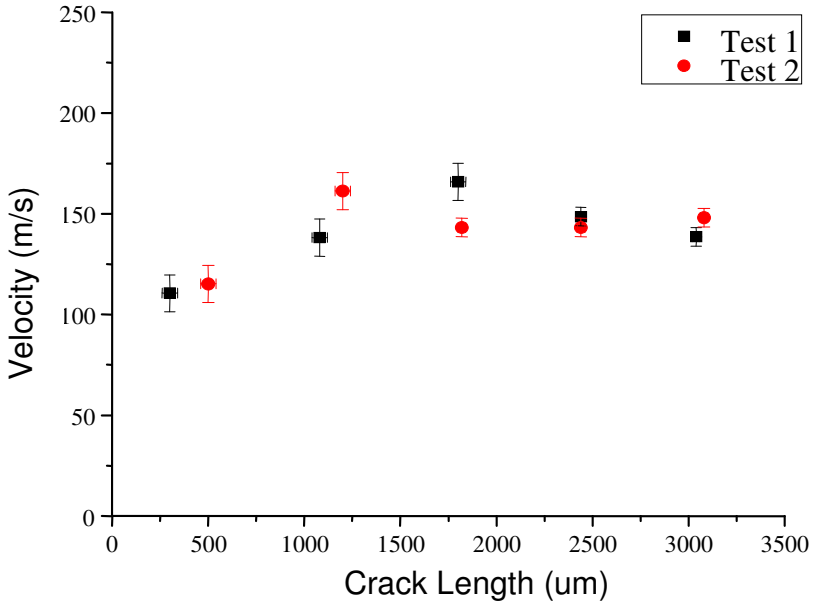


Figure 3.21. Results of dynamic fracture of dry NPG by tensile loading. Crack velocity-crack length behavior from both tests indicates an apparent terminal velocity of ~ 150-160 m/s.

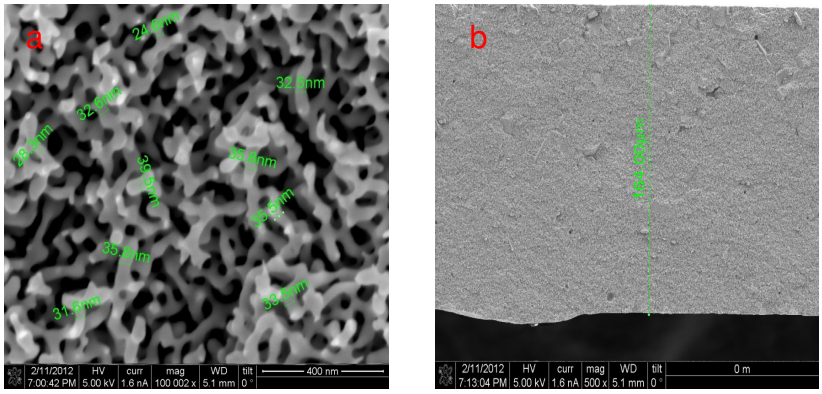


Figure 3.22. a. Nanoporous morphology of dry NPG after tensile loading (test 1) shows the ligament size around 35-40 nm b. Fracture surface of dry NPG after tensile loading test.

### 3.2.3 Dynamic Fracture in Electrolyte

#### 3.2.3.1 Bending Tests in Electrolyte

To examine dynamic fracture in monolithic NPG bending tests in electrolyte were conducted under potential control. A Gamry electrochemical station as well as the same experimental setup for bending tests in air was used to apply potential control on NPG samples during bending tests in electrolyte. A mercury lamp was used to replace x-cite gooseneck light source to obtain much more intense lighting conditions. Around a 30-50 um wide and EDM deep notch was put in AgAu alloy samples replacing the end milled notch to decrease field of view of the camera and therefore provide for increased camera rates. During tests, NPG samples were maintained in 1M $HClO_4$ at 1.20 V (vs NHE) after being fully dealloyed and transferred to main cell body. After recording the crack propagation process, the fracture surfaces were examined with SEM to measure pore size and assess the fracture mode.

The whole crack propagation process for one of the bending tests in electrolyte is shown in Figure 3.23. The crack was initiated in the middle of EDM notch in image b, accelerated in image c and decelerated in images, d to f. The same methods as bending and tensile tests in air were used to calculate crack length and crack propagation speed. The test results show that the dynamic fracture process occurred at much faster speed than in air. At the frame rate used in the tests, 1.91 us/frame, only 2 useful data points were obtained within the acceleration regime as the entire fracture

event occurred within 3.82 μs. The sample attained an apparent terminal crack velocity of 45 $ms^{-1}$. The crack decelerated very quickly after it reached close to the end of path due to compressive stress. The detailed results of crack propagation during tensile tests are shown in Table 3.5 and corresponding crack length and crack velocity behavior is plotted in Figure 3.24.

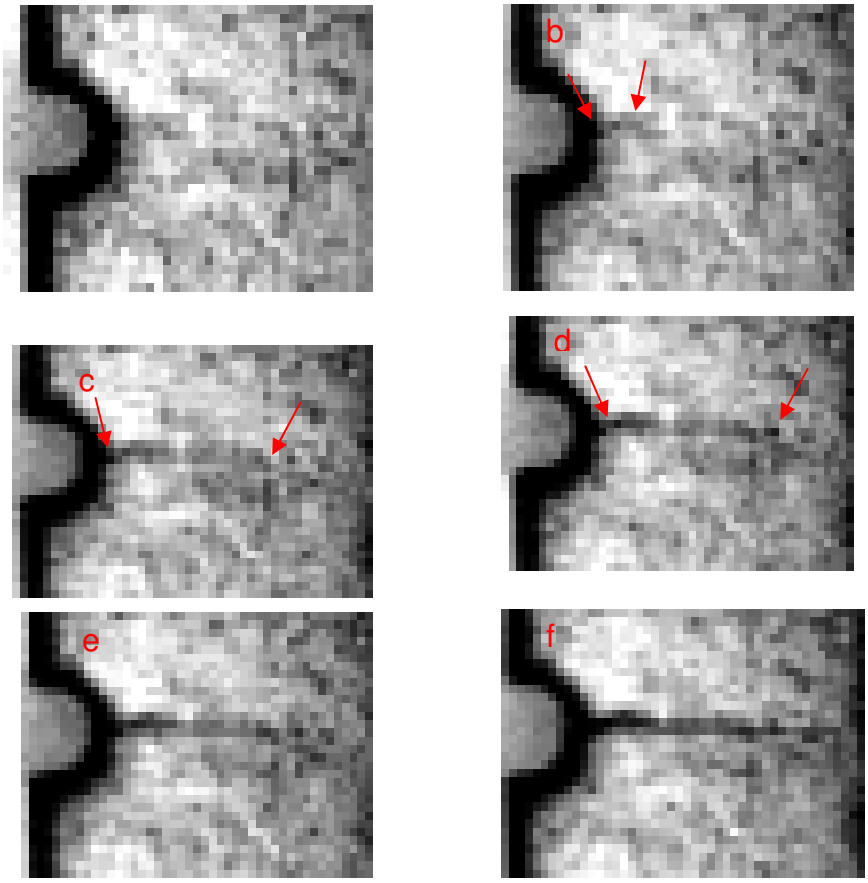


Figure 3.23. Dynamic fracture of NPG (0.74 volume fraction of porosity) containing an average ligament size of ~ 20 nm and under potential control at 1.20 V vs NHE in 1M $HClO_4$ in pure bending. a-f Consecutive images obtained at a frame rate of 1.91 us/frame. The red arrows serve to highlight the location of the propagating crack. The sample thickness is 220 um. The notch radius and depth is 35 um. The lighting conditions were more intense for the electrolyte experiments than that during bending test in air (shown in Figure 3.16).

Table 3.5 Results of dynamic fracture of NPG under potential control at 1.20 V vs NHE in 1M $HClO_4$ through pure bending. Frame number corresponds to those shown in Figure 3.23.

| Frame# | Crack propagation along X (pixels #) | Crack propagation along Y (pixels #) | Crack length (um) | Velocity (m/s) | Crack Length Error(um) | Velocity error (m/s) |
|---|---|---|---|---|---|---|
| a | 0 | 0 | 0 | 0 | 0 | 0 |
| b | 3 | 0 | 15 | 7.85 | ±5 | ±2.62 |
| c | 17 | 1 | 100.15 | 44.56 | ±5 | ±2.62 |
| d | 4 | 0 | 120.15 | 10.47 | ±5 | ±2.62 |
| e | 3 | 0 | 135.15 | 7.85 | ±5 | ±2.62 |
| f | 0 | 0 | 135.15 | 0 | 0 | 0 |

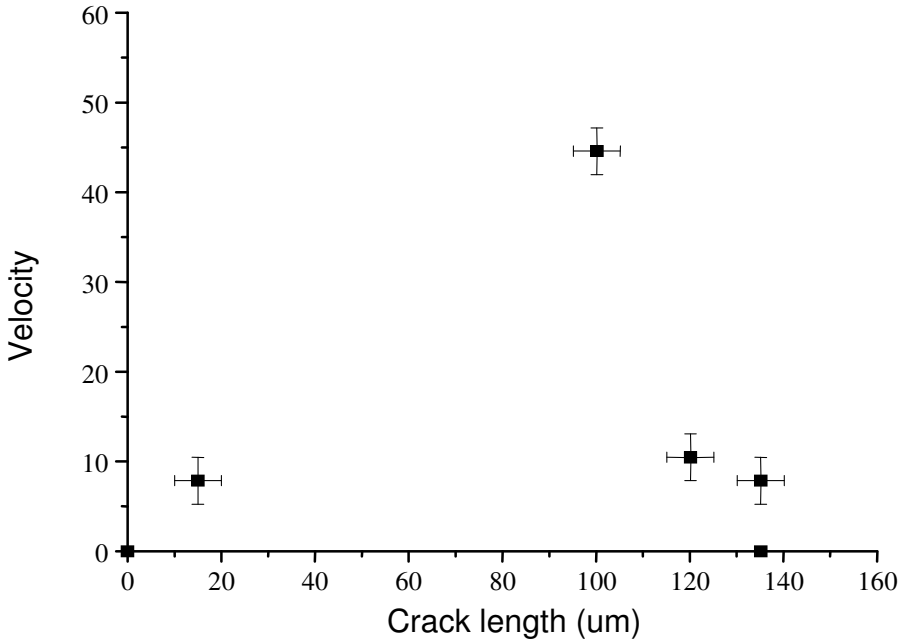


Figure 3.24. Results of dynamic fracture of NPG under potential control at 1.20 V vs NHE in 1M $HClO_4$ through pure bending. Crack velocity-crack length behavior indicates an apparent terminal velocity of ~ 45 m/s.

The fracture surfaces examined with SEM are shown in Figure 3. 25. The NPG sample only experienced around 0.5 hour coarsening in air before being fractured under potential control. The ligament size right after the fracture test was measured at 20 nm. The crack plane remained planar and the fracture path appeared to be generally transgranular. At crack initiation areas, instances of intergranular fracture were observed.

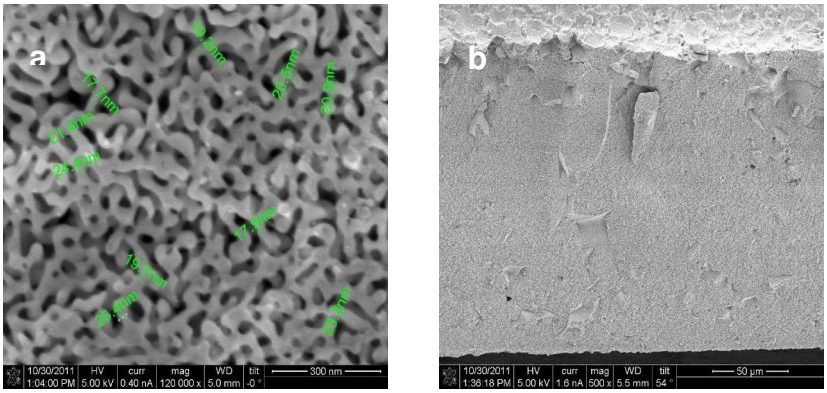


Figure 3.25. a. Nanoporous morphology of the NPG sample after bending test under potential control showing the ligament size around 20 nm. b. Fracture surface of the NPG after bending test.

The changes that occurred on a gold surface when an electrochemical potential was applied with $HClO_4$ as the electrolyte fell into three regimes *(67)*.Between 0 and 0.50 V (vs NHE), the surface builds up a negative charge like a capacitor. Between 0.5 and 1.2 V, the positive charge in the surface is compensated by an adsorbed layer of anions from the electrolyte. Between 1.20 and 1.50 V, a monolayer of oxidized gold is formed on the surface. The monolayer oxidation process begins with hydroxide ($OH^-$) adsorption into surface sites unoccupied by adsorbed $ClO4^-$; as the potential became more positive, more $OH^-$ is incorporated and correspondingly $ClO4^-$ desorbed. Finally, the surface undergoes a reconstruction in which the oxygen is incorporated on to the gold surface atoms to create a layer of gold oxide. Therefore, potential control at 1.2 V quenched coarsening to some degree in the NPG sample. By decreasing the ligament size from 40 nm to 20 nm, the macroscopic behavior is more

brittle and presumably more elastic, so it may be possible that 3-10 nm scale ligaments in NPG may yield terminal velocities more closely aligned with the predictions of Freund's analysis. To verify this possibility, a $Ag_{70}Au_{25}Pt_5$ alloy was fabricated with ligament size in the range of 3-10 nm. Snyder *(89)* has studied preparation of NPG with small and stable ligament size by dealloying this ternary alloy system. As explained in his study, Pt has much slower surface diffusion rate than Au, therefore during dissolution, Pt should accumulate and segregate to the edges of the growing vacancy island step edges, stabilizing edges and ultimately reducing the scale of porosity as well as leading to a Pt-rich shell (*89*). Some preliminary experiments on preparation of crack free nanoporous AuPt (NPAuPt) and tensile tests in air are included in Appendix A. Dealloying at constant potential of 1.34 V gave dealloying current density less than 0.7 $mA/cm^2$, however, cracks were still observed on the sample surface and these samples failed along grain boundaries. Galvanic dealloying with constant current density of ~100-200 $uA/cm^2$ is a possible solution to avoid cracks formation during dealloying in this system.

3.2.3.2 Dynamic Fracture in Tension in Electrolyte

A series of experiments on dynamic fracture of monolithic NPG through mechanical tensile loading as a function of electrochemical conditions was conducted to study the effect of surface chemistry on dynamic fracture. NPG samples were dealloyed and dried for 24 hours before being tested. The same micrometer controlled vise with a specially

designed Teflon cell held in between the micrometer stage was used to apply fixed displacement tensile loading during potential control on NPG samples. As described in experimental part 2.2.3.2, cyclic voltammetry between 0 V and 1.5 V (NHE) was run on NPG and Au thin film samples in order to confirm that the test protocols resulted in samples fully imbibed with electrolyte. Figure 3.26 and 3.27 shows the cyclic voltammetry curves for Au thin film and NPG samples, one of which was fully immersed in electrolyte and the other one was wetted on the tensile cell. As we have discussed above, between 1.20 and 1.50 V, a monolayer of oxidized gold is formed on both the Au thin film and NPG samples. From the obtained CV curves, clear oxidation peaks between 1.2 V and 1.5 V indicated the NPG tensile sample was fully imbibed. Due to the high surface area to volume ratio of NPG materials, we would expect charge required to oxidize the NPG samples with surface area around 0.88 $cm^2$ for top surfaces would be thousands of times larger than the corresponding flat Au thin film. By charge integration from 1.2 V to 1.5 V on the obtained CV curves, around 467 $uC/cm^2$ charge density was obtained for Au thin film in glass beaker, around 954 $mC/cm^2$ for NPG sample imbibed in electrolyte in glass beaker and around 705 $mC/cm^2$ for NPG sample wetted on tensile stage. The charge density of NPG sample wetted on vise is around 0.75 times that of the NPG sample fully immersed in electrolyte in a beaker. With this deviation, the edges of NPG sample on the vise stages would be estimated non- wetted without being directly in contact with electrolyte.

The center of NPG sample is right on top of Teflon cell and imbibed with electrolyte. This ensures the notch area is fully wetted and this is enough for our experiment as only the central part is studied for dynamic fracture experiments.

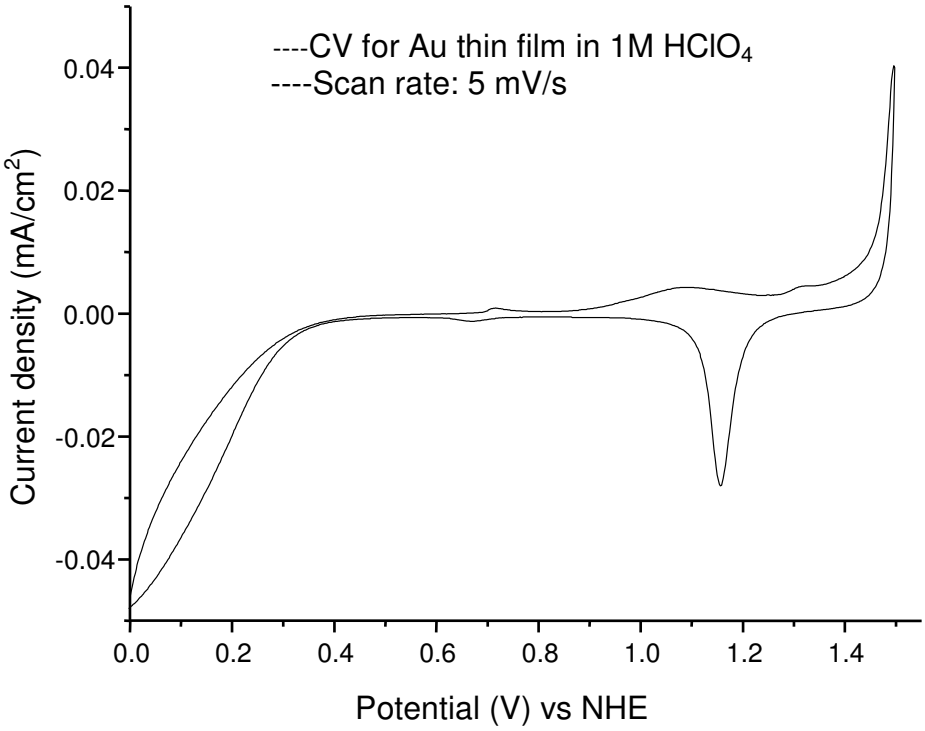


Figure 3.26. Cyclic voltammetry for Au thin film between 0 V and 1.5 V (NHE) in 1M $HClO_4$

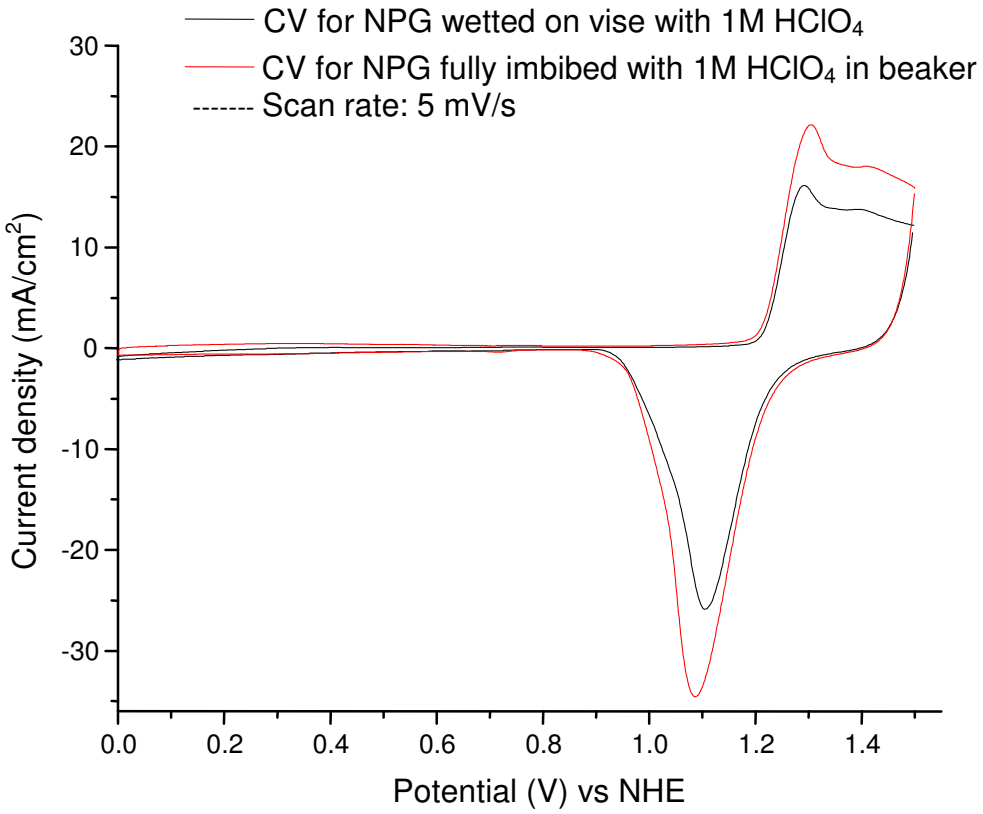


Figure 3.27. Cyclic voltammetry for NPG samples wetted on vise with 1M $HClO_4$ or fully imbibed with 1M $HClO_4$ in beaker between 0 V and 1.5 V (NHE).

Five potentials from 1.4 V to 0.5 V were examined as described in the experimental protocol. After samples were immersed in electrolyte and applied with potential control, samples were fractured quickly and crack propagation was recorded. The same methods used during bending and tensile tests in air were also used to calculate crack length and crack propagation speed for these tests under potential control. Detailed potential control and corresponding camera parameters are described in Table 2.2. Fracture surfaces from two potential tests were examined with

SEM to measure pore size and determine fracture mode. The results of dynamic fracture experiments will be discussed in the sequence from 1.4 V to 0.5 V (NHE).

Figure 3.28 shows one of the results obtained for one NPG sample applied with 1.4 V in 1M $HClO_4$. The crack was initiated in the middle of the EDM notch and the dynamic fracture process occurred at much faster speed than that in tensile test in air. At the frame rate used in the test, 3.45 us/frame, only 3 data points were obtained within the acceleration regime as the entire fracture event occurred within 3 frames or 10.35 us. The sample attained an apparent terminal crack velocity of 500 $ms^{-1}$. Crack paths in image a and b were very narrow and then in image c the crack opened and propagated to the end of the sample width. The detailed results of crack propagation during tensile tests are shown in Table 3.6 and corresponding crack length and crack velocity behavior is plotted in Figure 3.29.

In Figure 3.30, SEM examination on fracture surfaces shows that the ligament size of tested NPG samples after 24 hours drying in air was around 45 nm. Plastic deformation occurred at the tip of fractured ligaments and the fractured ligament tip size was around 10 nm. While individual ligaments fail by a shear process, the macroscopic behavior still showed “brittle” behavior and the fracture was planer and in a complete transgranular mode.

1.4 V

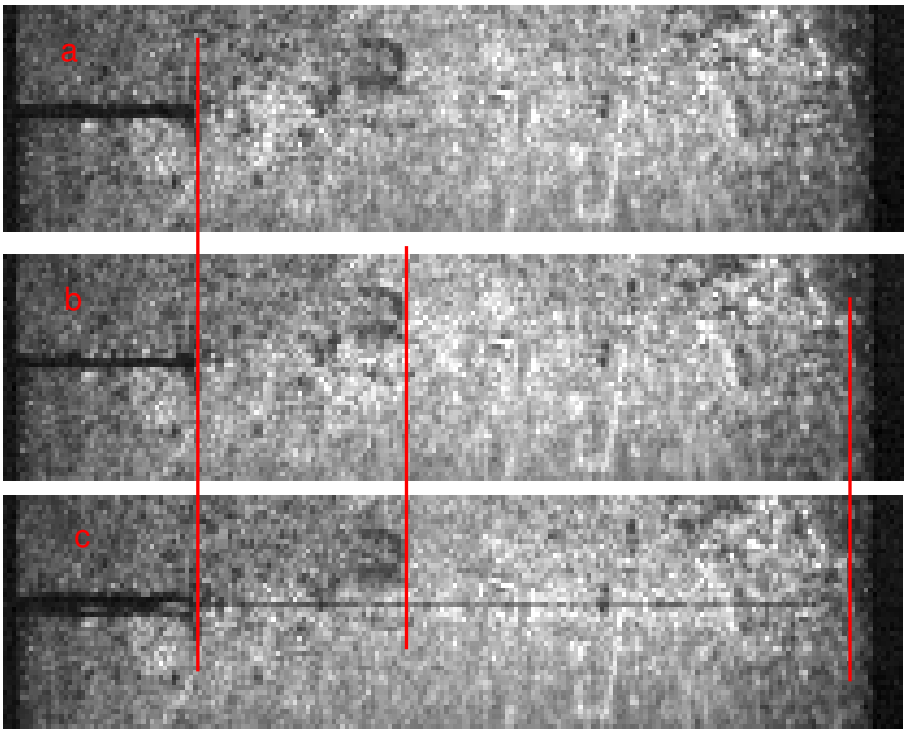


Figure 3.28. Dynamic tensile fracture of NPG (0.74 volume fraction of porosity) under potential control at 1.4 V vs NHE in 1M $HClO_4$. a – c were obtained at a rate of 3.45 us/frame. Notch is 800 um long and 30-50 um wide. Length of crack in each image is marked with red arrows. The sample width including notch is ~4 mm.

Table 3.6 Results of tensile dynamic fracture of NPG under potential control at 1.4 V vs NHE in 1M $HClO_4$. Frame number corresponds to those shown in Figure 3.28.

| Frame# | Crack propagation along X (pixels #) | Crack propagation along Y (pixels #) | Crack length (um) | Velocity (m/s) | Crack Length Error(um) | Velocity error (m/s) |
|---|---|---|---|---|---|---|
| a | 18 | 0 | 360 | 104.5 | ±100 | ±29 |
| b | 38 | 0 | 1120 | 220.5 | ±100 | ±29 |
| c | 87 | 0 | 2860 | 504.9 | ±60 | ±17.4 |

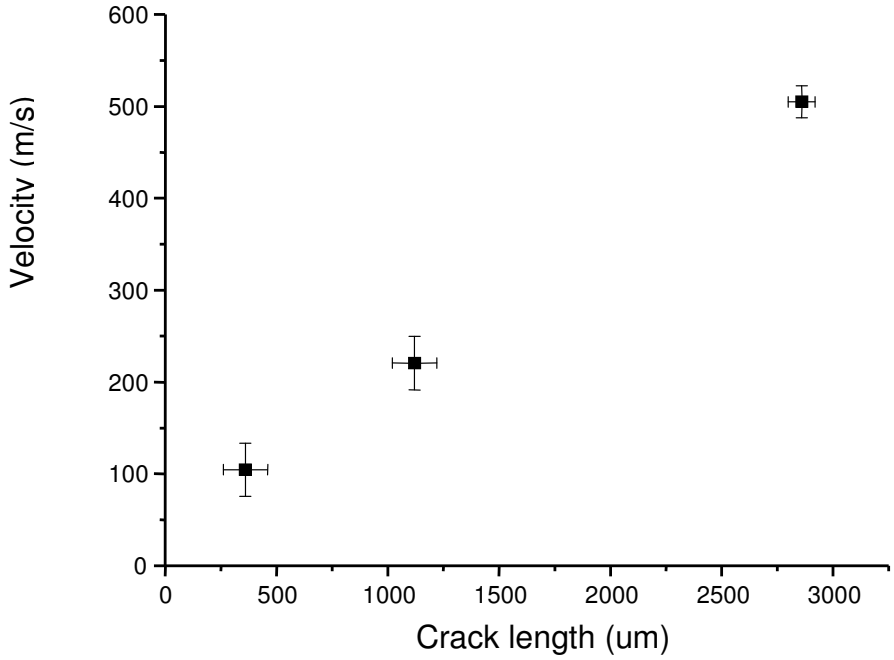


Figure 3.29. Results of dynamic fracture of NPG under potential control at 1.4 V vs NHE in 1M $HClO_4$ by tensile loading. Crack velocity-crack length behavior indicates an apparent terminal velocity of ~ 500 m/s.

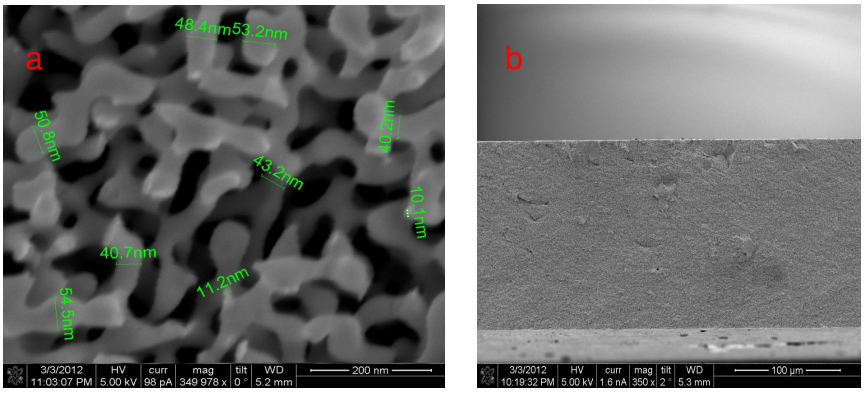


Figure 3.30. a. Morphology of the NPG sample after tensile loading test under potential control at 1.4 V showing the ligament size around 45 nm. b. Fracture surface of the NPG after tensile loading test.

The above test result show NPG sample becomes more brittle and crack propagates much faster under potential control at 1.4 V. However, one other experiment under nominally the same condition showed much slower crack propagation rate. The crack propagation process (shown in Figure 3.31) indicated slow crack initiation and then staying static at around 660 um crack length for 6.9 us before second crack initiation and propagation. As a result we only analyzed second stage of crack initiation and propagation process and obtained crack terminal velocity of around 90 m/s. The corresponding crack propagation data is included in Table 3.7 and crack length and crack velocity behavior is plotted in Figure 3.32.

In the dynamic fracture experiments, pre-existing cracks in test samples will lower Young's modulus of the sample and this would result in a lower crack velocity. The SEM images (Figure 3.33) of the tested NPG sample show only a few wide open cracks were found near the epoxy glue

areas and slightly cracked grain boundaries in the middle of NPG samples. This likely occurred during removal of the sample from the test fixture. Careful attention should also be paid during handling and applying epoxy glue to samples.

1.4 V

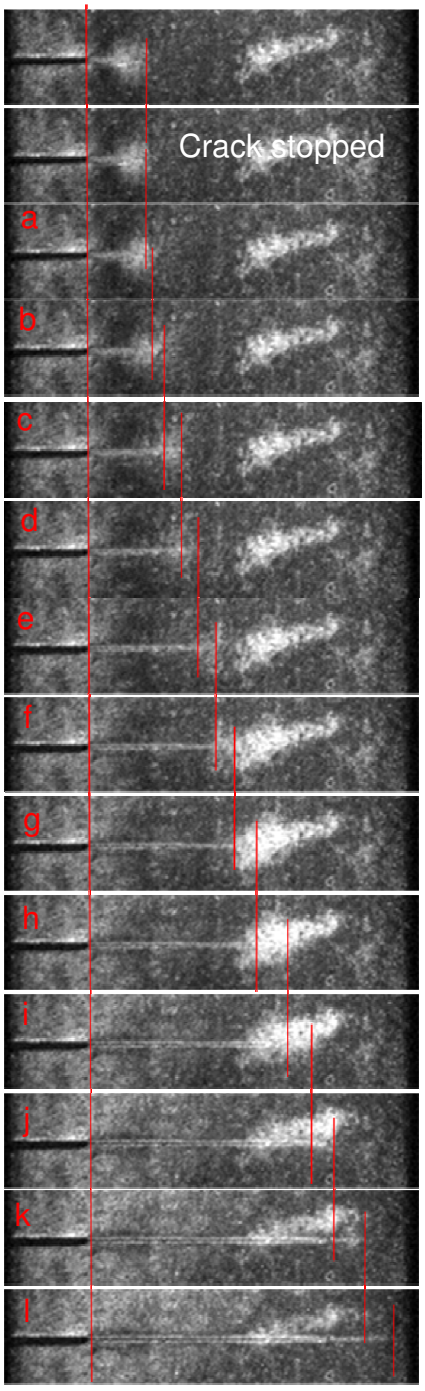


Figure 3.31. Second test of dynamic fracture of NPG sample under potential control at 1.4 V vs NHE in 1M $HClO_4$ by tensile loading. Length of crack in each image is indicated with red arrows.

Table 3.7 Results of second test of dynamic fracture of NPG under potential control at 1.4 V vs NHE in 1M $HClO_4$ by tensile loading. Frame number corresponds to those shown in Figure 3.31.

| Frame # | Crack propagation along X (pixels #) | Crack propagation along Y (pixels #) | Crack length (um) | Velocity (m/s) | Crack Length Error(um) | Velocity error (m/s) |
|---|---|---|---|---|---|---|
| a | 3 | 0 | 660 | 17.4 | ±60 | ±13.8 |
| b | 4 | 0 | 740 | 23.2 | ±100 | ±23.0 |
| c | 9 | 0 | 920 | 52.2 | ±100 | ±23.0 |
| d | 8 | 0 | 1080 | 46.4 | ±100 | ±23.0 |
| e | 8 | 0 | 1240 | 46.4 | ±80 | ±18.4 |
| f | 9 | 0 | 1420 | 52.2 | ±80 | ±18.4 |
| g | 13 | 0 | 1680 | 75.4 | ±80 | ±18.4 |
| h | 15 | 0 | 1980 | 87 | ±80 | ±18.4 |
| i | 15 | 0 | 2280 | 87 | ±80 | ±18.4 |
| j | 12 | 0 | 2520 | 69.6 | ±60 | ±13.8 |
| k | 16 | 0 | 2840 | 92.7 | ±60 | ±13.8 |
| l | 14 | 0 | 3120 | 81.1 | ±60 | ±13.8 |

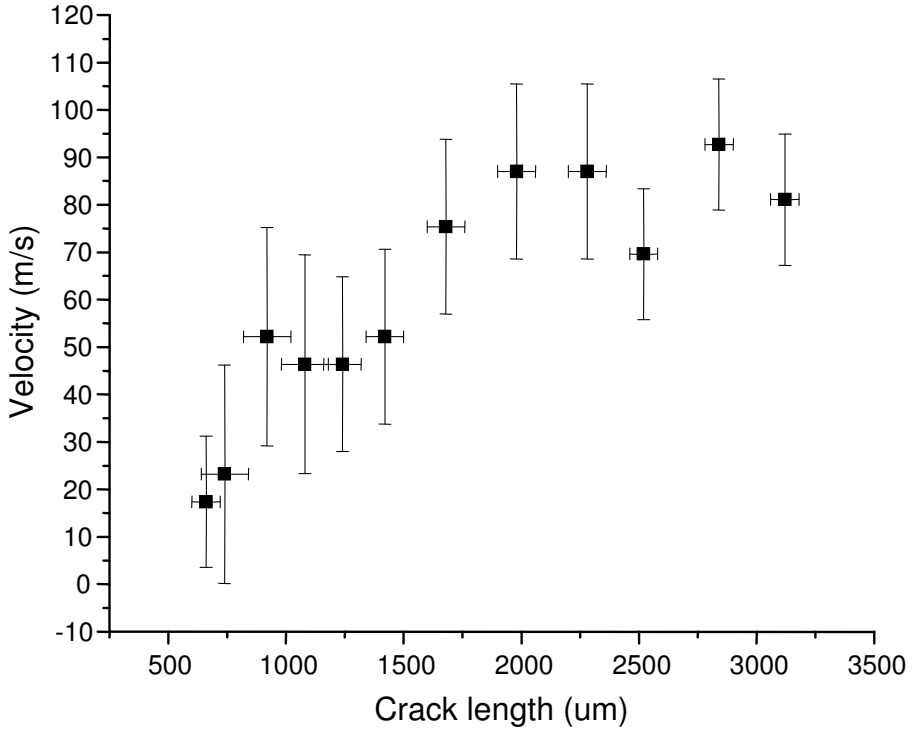


Figure 3.32. Results of second test of dynamic fracture of NPG under potential control at 1.4 V vs NHE in 1M $HClO_4$ by tensile loading. Crack velocity-crack length behavior indicates an apparent terminal velocity of ~ 90 m/s.

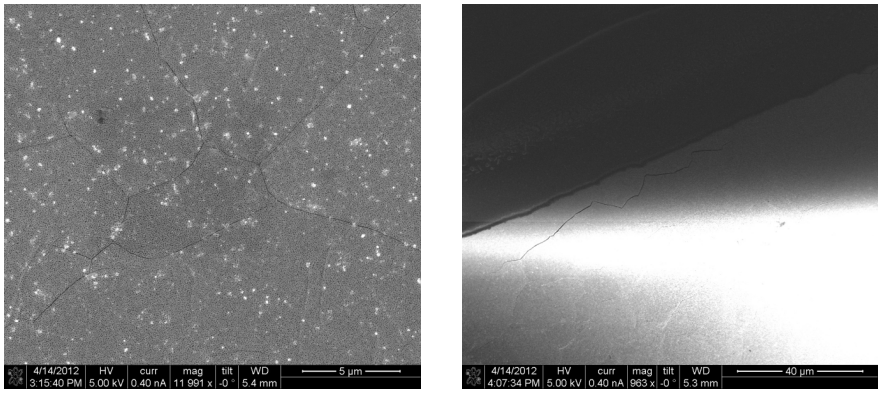


Figure 3.33. Top surface of NPG sample after dynamic fracture experiment under potential control at 1.4 V (illustrated in Figure 3.25). Only a few wide open cracks were found near epoxy glue and slightly cracked grain boundaries in the middle of NPG samples

Figure 3.34 gives two test tensile results for NPG samples at 1.2 V in 1M $HClO_4$. The same methods as above experiments were used to calculate crack length and crack propagation speed. Cracking initiated in the middle of EDM notches. However the fracture process occurred at much lower speed than the tensile test with potential control of 1.4 V vs NHE. At the frame rate used for both of the two tests, 4.34 us/frame, for test 1 shown on the left column total 17 frames were obtained for the whole crack propagation process, while for test 2 shown on the right column 15 frames obtained. Cracks did not appear to propagate continuously in both of the tests and in Figure 3.34 only consecutive propagation images are shown. This could be a manifestation of the difficulty in accessing the exact position of the crack tip in several of the captured frames. During test 1, crack stopped and reinitiated at crack

length of 736 um. While for test 2, initial crack propagation stage was smooth and crack stopped at a crack length of 1580 um. The detailed results for crack propagation images shown in Figure 3.34 are shown in Table 3.8 and the corresponding crack length and crack velocity behavior for both tests are plotted in the same Figure 3.35. The apparent terminal velocity obtained during these two tests is around 90-100 m/s.

1.2 V Test 1. Test 2

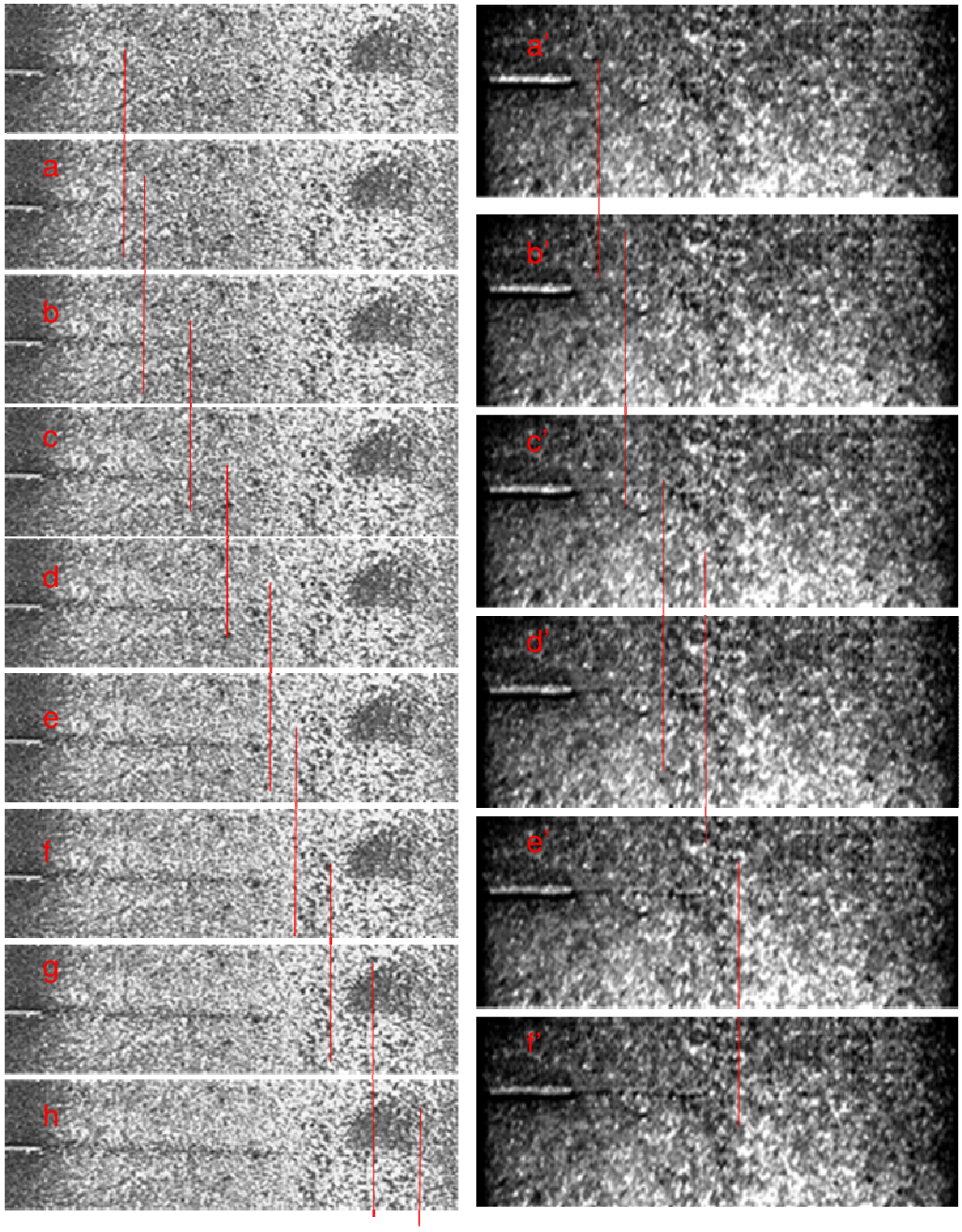


Figure 3.34. Dynamic fracture of NPG under potential control at 1.2 V vs NHE in 1M $HClO_4$ by tensile loading. a – h and a'-f' were obtained at a rate of 4.34 us/frame. Pre-notch is 800um long and 30-50 um wide. Length of crack in each image is indicated by red arrows. The sample width including notch is ~4 mm.

Table 3.8 Results of dynamic fracture of NPG under potential control at 1.2 V vs NHE in 1M $HClO_4$ by tensile loading. Frame number corresponds to those shown in Figure 3.34.

| Frame # | Crack propagation along X (pixels #) | Crack propagation along Y (pixels #) | Crack length (um) | Velocity (m/s) | Crack Length Error(um) | Velocity error (m/s) |
|---|---|---|---|---|---|---|
| a | 36 | 1 | 736 | 37.1 | ±80 | ±18.43 |
| b | 10 | 1 | 1024 | 66.4 | ±64 | ±14.75 |
| c | 18 | 0 | 1392 | 84.8 | ±64 | ±14.75 |
| d | 23 | 0 | 1696 | 70 | ±80 | ±18.43 |
| e | 19 | 0 | 1968 | 62.8 | ±80 | ±18.43 |
| f | 17 | 1 | 2288 | 73.7 | ±80 | ±18.43 |
| g | 20 | 0 | 2656 | 84.8 | ±64 | ±14.75 |
| h | 23 | 0 | 2944 | 66.8 | ±80 | ±18.43 |
| a’ | 11 | 0 | 220 | 50.7 | ±100 | ±23.04 |
| b’ | 14 | 0 | 500 | 64.5 | ±100 | ±23.04 |
| c’ | 15 | 0 | 800 | 69.1 | ±100 | ±23.04 |
| d’ | 21 | 0 | 1220 | 96.8 | ±100 | ±23.04 |
| e’ | 18 | 0 | 1580 | 82.9 | ±100 | ±23.04 |

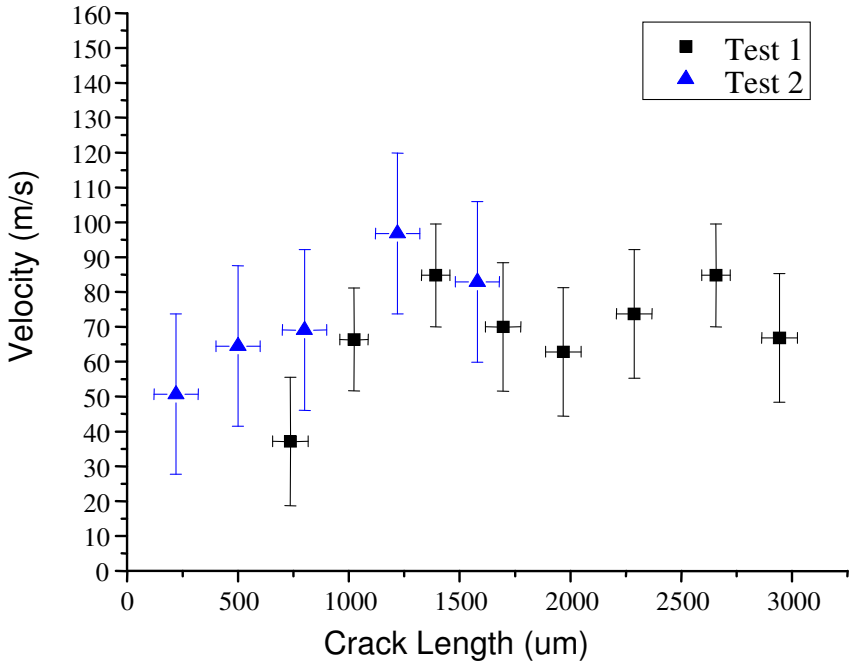


Figure 3.35. Results of dynamic fracture of NPG under potential control at 1.2 V vs NHE in 1M $HClO_4$ by tensile loading. Crack velocity-crack length behavior indicating an apparent terminal velocity of ~ 90 m/s.

Figure 3.36 shows one of the results obtained for NPG samples applied with 1.0 V in 1M $HClO_4$. Crack propagation initiated from the center of the EDM notch and the fracture process occurred consecutively. During the whole crack propagation process, the crack stayed very narrow. At the frame rate used in the tests, 3.45 us/frame, 7 data points were obtained within the acceleration regime as the entire fracture event occurred within 7 frames or 24.15 us. The sample attained an apparent terminal crack velocity of 140-150 $ms^{-1}$, which is close to the terminal velocity measured in air. The initial crack acceleration in this test is slower in comparison to that in air. The detailed results of crack propagation are

shown in Table 3.9 and corresponding crack length and crack velocity behavior is plotted in Figure 3.37.

Figure 3.38 gives that the ligament size of tested NPG samples was 40 nm. Plastic deformation was also observed at the tip of the fractured gold ligaments and the tip size was around 10 nm. While the individual ligaments fail by a shear process, the 40 nm ligament size still can support brittle failure macroscopically and fracture plane was planar and transgranular.

1.0 V

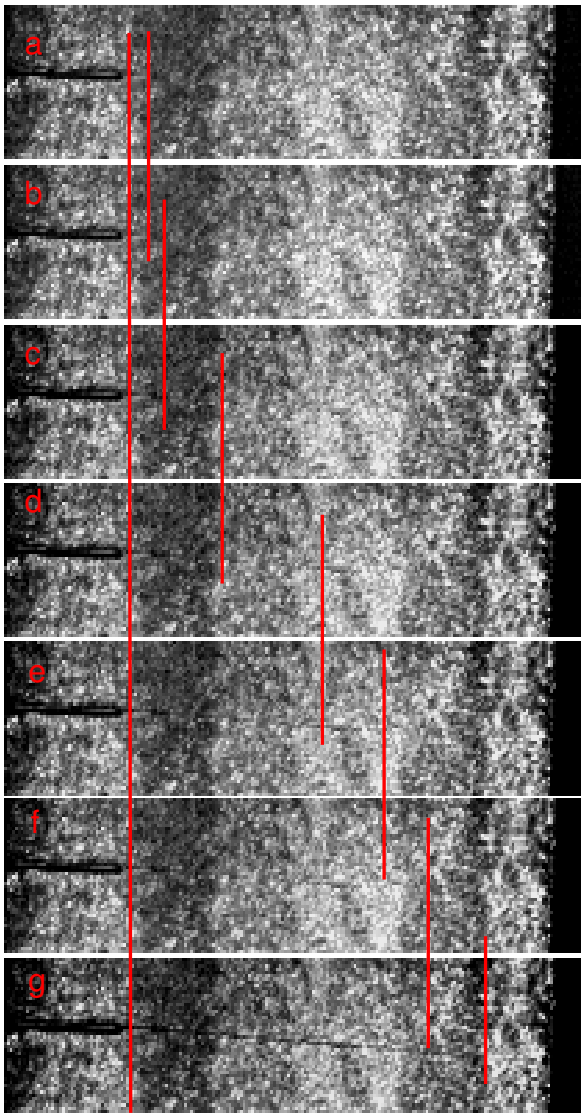


Figure 3.36. Dynamic fracture of NPG (0.74 volume fraction of porosity) under potential control at 1.0 V vs NHE in 1M $HClO_4$ by tensile loading. Samples was dealloyed in1M $HNO_3$ at 1.2 V vs NHE and dried in air for 24 hours before test. a – g were obtained at a rate of 3.45 us/frame. Pre-notch is around 800 um long and 30-50 um wide. Length of crack in each image is indicated by red arrows. The sample width including notch is ~4 mm.

Table 3.9 Results of dynamic fracture of NPG under potential control at 1.0V vs NHE in 1M $HClO_4$ by tensile loading. Frame number corresponds to those shown in Figure 3.36.

| Frame# | Crack propagation along X (pixels #) | Crack propagation along Y (pixels #) | Crack length (um) | Velocity (m/s) | Crack Length Error(um) | Velocity error (m/s) |
|---|---|---|---|---|---|---|
| a | 11 | 0 | 220 | 63.8 | ±100 | ±29 |
| b | 15 | 0 | 520 | 87.1 | ±100 | ±29 |
| c | 25 | 0 | 1020 | 145.1 | ±120 | ±29 |
| d | 28 | 5 | 1580 | 165.1 | ±80 | ±23.2 |
| e | 16 | 2 | 1900 | 93.6 | ±80 | ±23.2 |
| f | 19 | 2 | 2280 | 110.9 | ±60 | ±23.2 |
| g | 16 | 2 | 2600 | 93.6 | ±60 | ±17.4 |

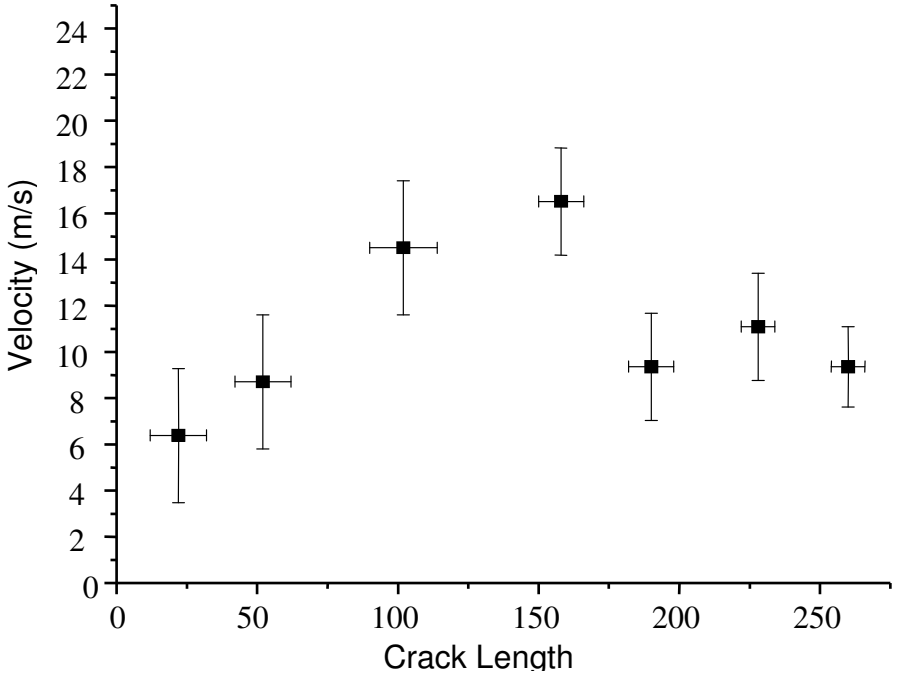


Figure 3.37. Results of dynamic fracture of NPG under potential control at 1.0 V vs NHE in 1M $HClO_4$ by tensile loading. Crack velocity-crack length behavior indicates an apparent terminal velocity of ~ 140-150 m/s.

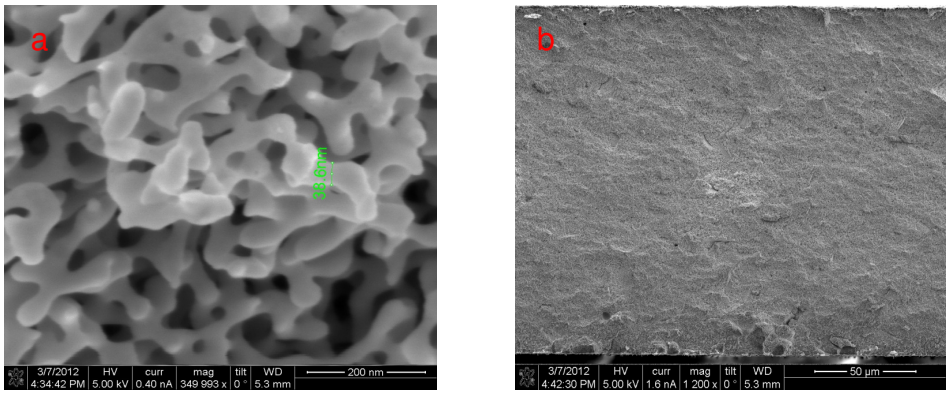


Figure 3.38. a. Nanoporous morphology of the NPG sample after tensile loading test under potential control at 1.0 V vs NHE showing the ligament size around 40 nm. b. Fracture surface of the NPG after tensile loading test.

The crack propagation process for one NPG sample controlled at 0.7 V is shown in Figure 3.39. For this set of experiment, crack propagated continuously at the initial stage, then stayed static for 13.02 us (3 images) and then experienced crack re-initiation and continuous propagation process. In the following crack length and crack speed calculation, only the second stage crack propagation was analyzed. At the frame rate used in the test, 4.34 us/frame, 5 data points were obtained within the second crack propagation regime. The detailed results of crack propagation are shown in Table 3.10. Crack velocity-crack length behavior plotted in Figure 3.40 indicated an apparent terminal velocity of ~ 110 m/s, which is a little slower than the terminal velocity for tensile test in air.

0.7 V

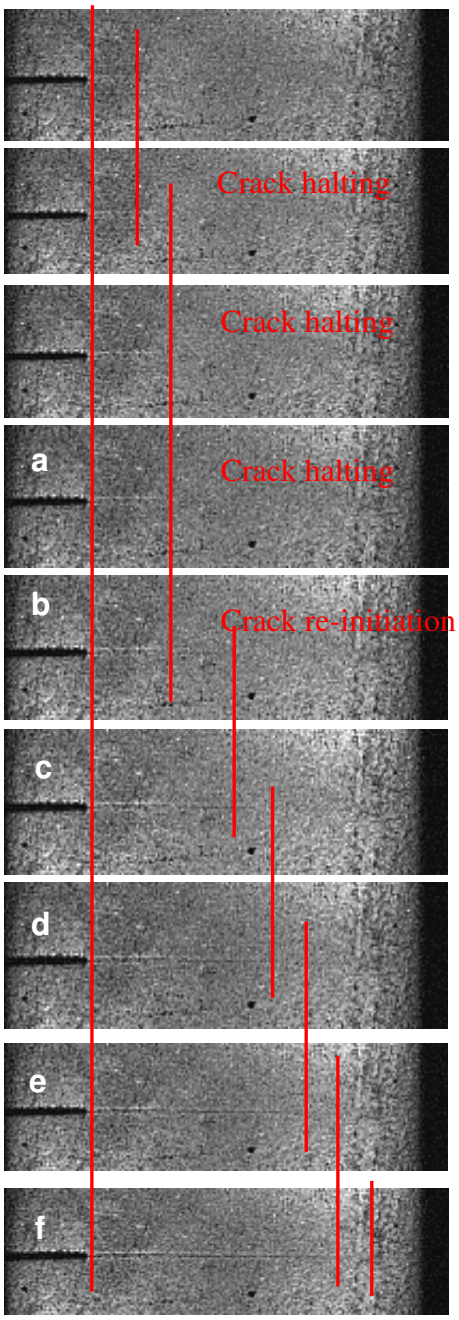


Figure 3.39. Dynamic fracture of NPG (0.74 volume fraction of porosity) under potential control at 0.7 V vs NHE in 1M $HClO_4$ by tensile loading. a – f were obtained at a rate of 4.34 us/frame. Pre-notch is around 800um long and 30-50 um wide. Length of crack in each image is indicated by red arrows. The sample width including notch is ~4 mm.

Table 3.10 Results of dynamic fracture of NPG under potential control at 0.7 V vs NHE in 1M $HClO_4$ by tensile loading. Frame number corresponds to those shown in Figure 3.39

| Frame# | Crack propagation along X (pixels #) | Crack propagation along Y (pixels #) | Crack length (um) | Velocity (m/s) | Crack Length Error(um) | Velocity error (m/s) |
|---|---|---|---|---|---|---|
| a | 0 | 0 | 600 | 0 | ±0 | ± 0 |
| b | 24 | 2 | 1080 | 110.9 | ±100 | ±23.04 |
| c | 21 | 0 | 1500 | 96.8 | ±60 | ±13.82 |
| d | 17 | 0 | 1840 | 78.3 | ±60 | ±13.82 |
| e | 17 | 0 | 2180 | 78.3 | ±60 | ±13.82 |
| f | 19 | 0 | 2560 | 87.6 | ±40 | ±9.22 |

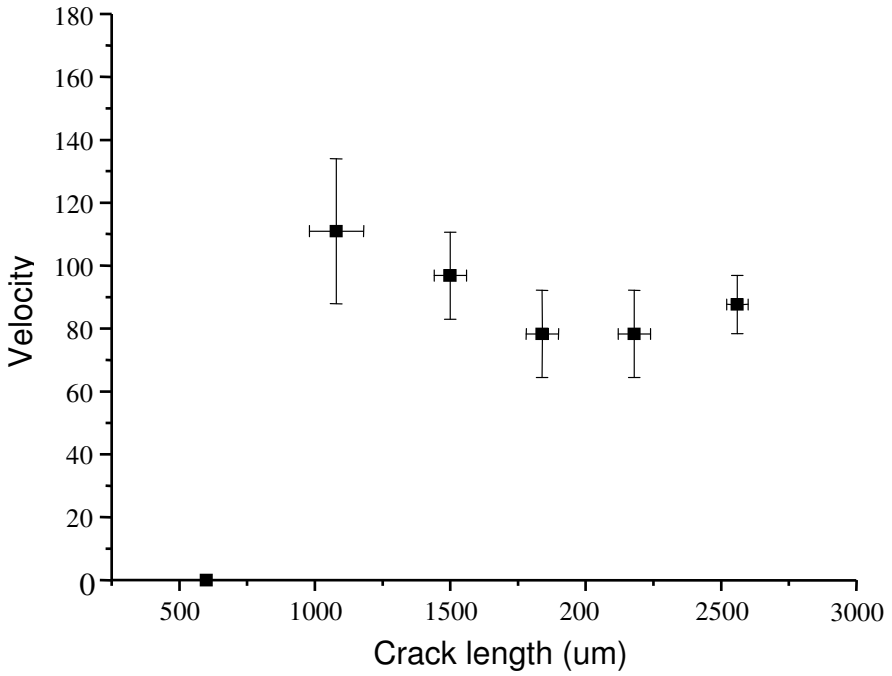


Figure 3.40. Results of dynamic fracture of NPG under potential control at 0.7 V vs NHE in 1M $HClO_4$ by tensile loading. Crack velocity-crack length behavior indicates an apparent terminal velocity of ~ 110 m/s.

Figure 3.41 shows the dynamic fracture process for NPG sample controlled at close to potential of zero charge, 0.5 V. During this set of experiments, crack propagated continuously all across the sample width. At the frame rate of 4.34 us/frame, total 14 data points were obtained within the crack acceleration regime. Crack propagation took 8 frames within the initial 1mm crack length regime. The detailed results of crack propagation are shown in Table 3.11. The crack velocity-crack length behavior plotted in Figure 3.42 indicated an apparent terminal velocity of ~ 100-110 m/s.

0.5 V

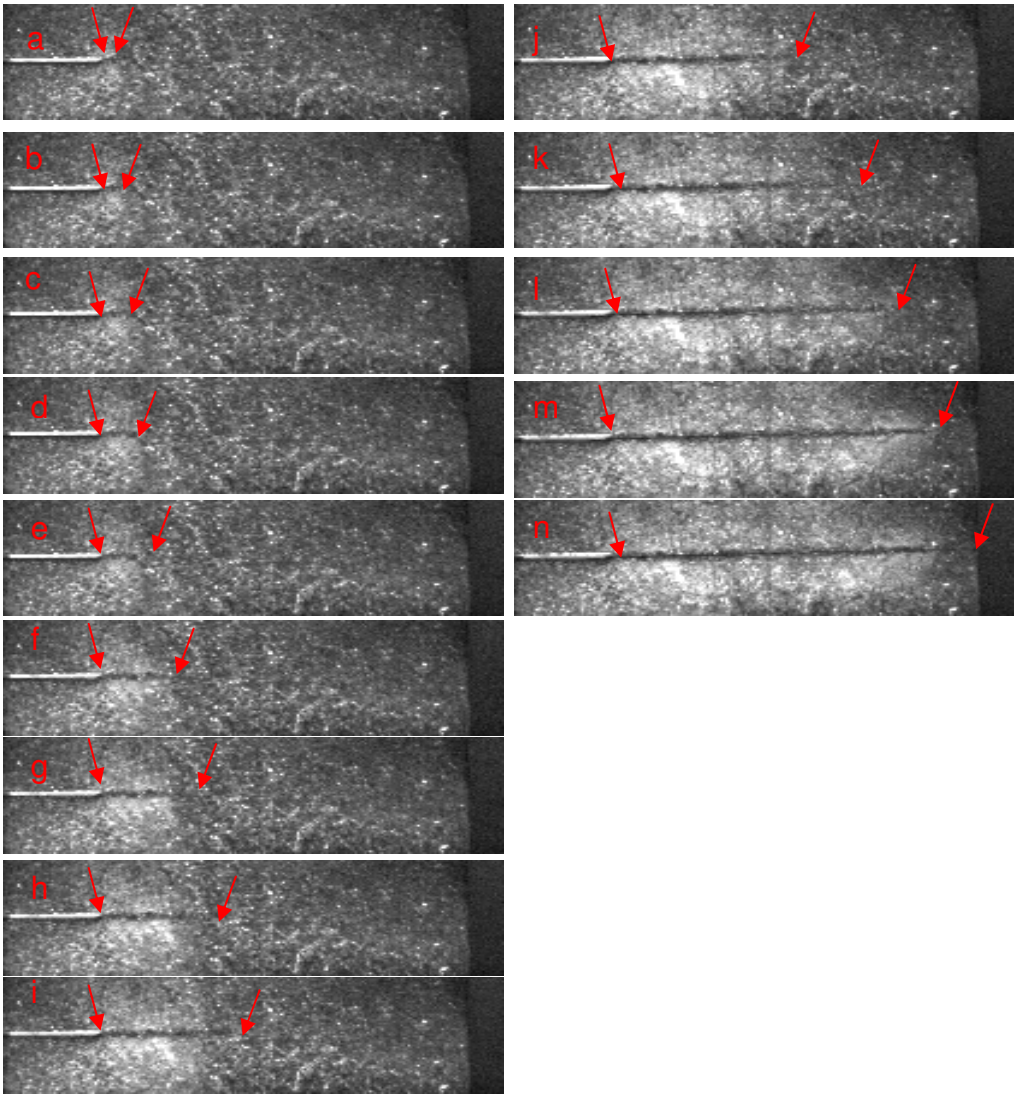


Figure 3.41. Dynamic fracture of NPG (0.74 volume fraction of porosity) under potential control at 0.5 V vs NHE in 1M $HClO_4$ by tensile loading. a – n were obtained at a rate of 4.34 us/frame. Pre-notch is around 800 um long and 30-50 um wide. Length of crack in each image is indicated by red arrows. The sample width including notch is ~4 mm.

Table 3.11 Results of dynamic fracture of NPG under potential control at 0.5 V vs NHE in 1M $HClO_4$ by tensile loading. Frame number corresponds to those shown in Figure 3.41.

| Frame# | Crack propagation along X (pixels #) | Crack propagation along Y (pixels #) | Crack length (um) | Velocity (m/s) | Crack Length Error(um) | Velocity error (m/s) |
|---|---|---|---|---|---|---|
| a | 4 | 0 | 80 | 18.4 | ±60 | ±13.8 |
| b | 3 | 0 | 140 | 13.8 | ±40 | ±9.2 |
| c | 3 | 2 | 200 | 16.6 | ±60 | ±13.8 |
| d | 5 | 0 | 300 | 23 | ±60 | ±13.8 |
| e | 6 | 1 | 420 | 28 | ±60 | ±13.8 |
| f | 7 | 2 | 560 | 33.5 | ±80 | ±18.4 |
| g | 5 | 2 | 660 | 24.8 | ±80 | ±18.4 |
| h | 7 | 0 | 800 | 32.3 | ±80 | ±18.4 |
| i | 14 | 2 | 1080 | 65.2 | ±80 | ±18.4 |
| j | 20 | 3 | 1480 | 93.2 | ±60 | ±13.8 |
| k | 20 | 2 | 1880 | 92.6 | ±60 | ±13.8 |
| l | 25 | 2 | 2380 | 115.6 | ±60 | ±13.8 |
| m | 15 | 3 | 2680 | 70.5 | ±40 | ±9.2 |
| n | 18 | 0 | 3040 | 82.9 | ±40 | ±9.2 |

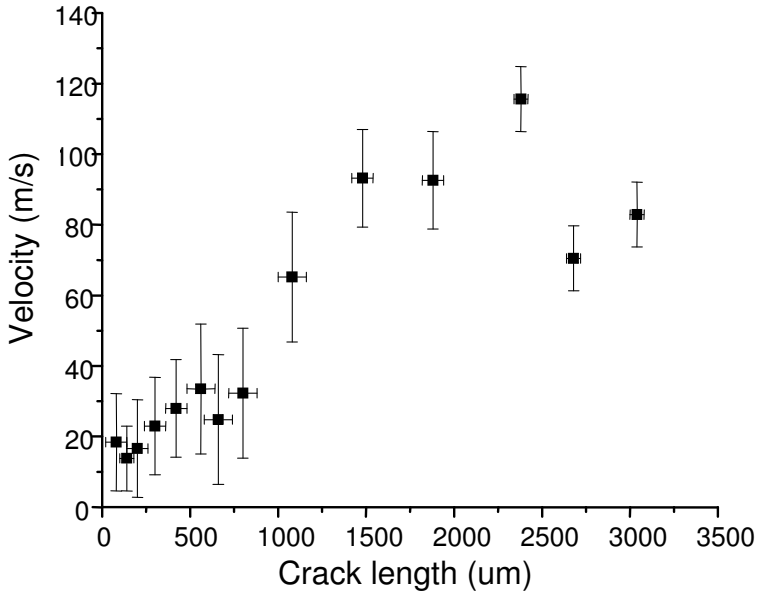


Figure 3.42. Results of dynamic fracture of NPG under potential control at 0.5 V vs NHE in 1M $HClO_4$ by tensile loading. Crack velocity-crack length behavior indicating an apparent terminal velocity of ~ 100-110 m/s.

Conventional dynamic fracture theory predicts the limiting crack velocity in an elastic solid is proportional to $(E/\rho)^{1/2}$. More plasticity in the material would decrease material's brittleness and therefore result in a lower terminal crack velocity. We would expect this behavior for samples under applied potentials from 0 V to 1.5 V. As movement of dislocations at potentials from 0 V to 1.2 V is similar to samples in dry state, we would expect terminal velocity of NPG close to that in dry state. At around 0.5 V, which corresponds to potential of zero charge for NPG in 1M $HClO_4$, the terminal velocity of NPG should be mostly close to as that in air. From around 1.2 V, crack terminal velocity increases with formation of surface oxide layer, which can reduce surface mobility of dislocations by pinning it

at the surface or act as a barrier to impede a dislocation from escaping from the surface.

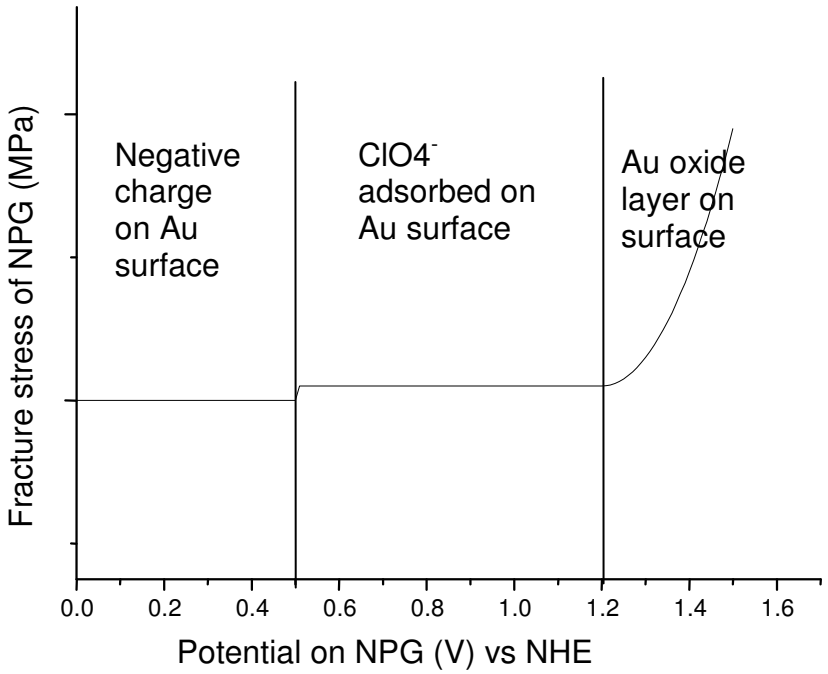


Figure 3.43. Sketch of fracture stress of NPG under different applied potentials from 0 V to 1.5 V vs NHE. Fracture stress varies with NPG surface chemistry which corresponds to three regimes: free surface with negative charge between 0-0.5 V; adsorption with $ClO4^-$ ions between 0.5-1.2 V and oxidation regime between 1.2-1.5 V.

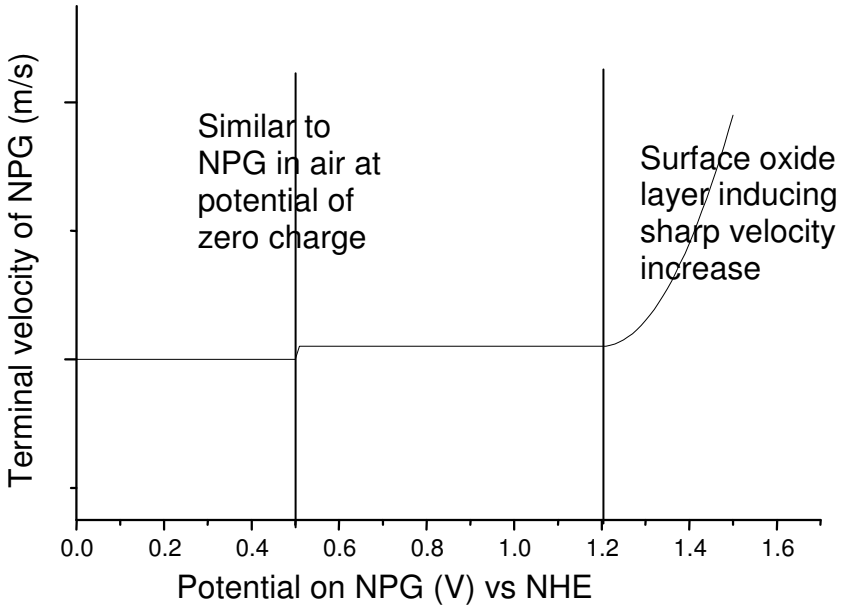


Figure 3.44. Sketch of terminal velocity of NPG under different applied potentials from 0 to 1.5 V vs NHE. From 0 to 1.2 V, terminal velocity being close to that in air; from 1.2 to 1.5 V, terminal velocity increases dramatically due to surface oxide layer.

The crack terminal velocities in our dynamic fracture tests are summarized in Table 3.12 and plotted in Figure 3.45. The test results occur in the same trend predicted by the above analysis. The terminal velocity at 1.4 V (NHE) in our tests is around 500 m/s and lower than what is expected for a purely elastic nanoporous gold structure. As from around 1.2 V(NHE), NPG surface is covered surface oxide layer and material turns to be more brittle, tensile tests within this area should be explored more carefully and many more experiments should be conducted to get larger data sets. The crack velocities of NPG under potential control at 0.5 V, 0.7 V and 1.2 V are lower than that in air test. One possible reason to

be considered is that cracks were formed in NPG samples during dealloying or handling process

Table 3.12 Summary of terminal velocities of NPG with ligament size around 40 nm in 1M $HClO_4$ at five different potentials by tensile loading

| Applied potential(V vs NHE) | Velocity (m/s) | Velocity error (m/s) |
|---|---|---|
| 0.5 | 115.6 | ± 13.8 |
| 0.5(in air) | 161.3 | ± 9.22 |
| 0.7 | 110.9 | ±23.04 |
| 1.0 | 165.1 | ±23.2 |
| 1.2 | 96.8 | ±23.04 |
| 1.4 | 504.9 | ±17.4 |

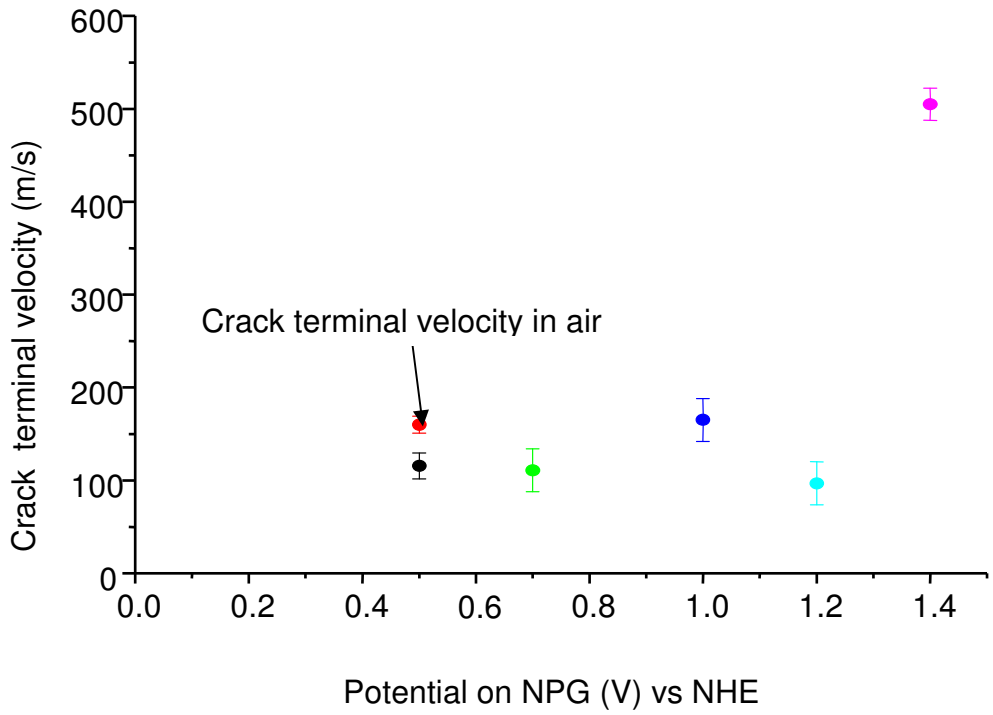


Figure 3.45. Crack terminal velocities of NPG during tensile tests in 1M $HClO_4$ under 5 different applied potentials.

# Chapter 4

## SUMMARY

This research examined the film-induced cleavage model of stress corrosion cracking. In this model, for alloy systems such as stainless steel and noble metal alloys such as silver-gold, the corrosion process induces the formation of a nanoporous brittle layer that serves to initiate a high-speed dynamic crack that is mechanically injected into the un-dealloyed parent phase. This crack injection occurs owing to the kinetic energy of the dynamic crack. There were two major overarching goals to the research described herein. One was to decouple the effects of stress and dealloying corrosion to determine the specific roles of these parameters in intergranular stress-corrosion cracking. The other was to measure the crack velocity in monolithic nanoporous gold which is the prototypical dealloyed morphology. In order to examine these issues crack injection experiments were performed under conditions where the stress and corrosion processes were de-coupled. Dynamic fracture experiments of monolithic nanoporous gold were performed in air and electrolyte under potential control and a high speed 1 million frame/second camera was used to measure the crack velocity.

In comparison with dealloying in acidic electrolyte, dealloying of AgAu alloys in neutral electrolyte at high potential provides stable nanoporous structures with silver oxide covering the gold ligaments. Focused ion-beam cross-section milling of dealloyed samples indicated ~ 3-5 times

greater dealloying penetration down grain boundaries versus the grain interior. Successful crack injection experiments into undealloyed bulk were achieved under both tensile loading and hand bending. Cross-sectional focused ion-beam milling of intergranular cracks showed crack penetration occurred significantly beyond the depth of grain boundary dealloying. In the hand bending experiments, decoupling of stress and dealloying was achieved successfully on all tested samples. Film induced cleavage was observed on samples aged in electrolyte or air over time scales of 1-15 minutes. This was observed both for de-ionized water and air aging completely excludes any stress assisted corrosion process. For longer aging times crack injection was not observed which also excludes the possibility of deep grain boundary dealloying crack penetration. Compositional analysis along side crack walls showed good consistency with the milling result and further verified crack injection phenomenon. The limitation of the hand bending experiments for crack injection is that the sample experiences a reduced crack injection distance in bending since there is a compressive stress on the side of the sample into which the crack is injected. Accordingly future work should be performed in tension in an apparatus designed so that there is a zero stress level on the sample during dealloying.

Crack-free monolithic nanoporous gold samples for the dynamic fracture experiments were fabricated under fixed potentiostatic (1.2 V NHE) condition. Galvanostatic dealloying at current densities of ~100-200

$uA/cm^2$ is suggested to lower dealloying rate and reduce volume contraction caused by high rate.

Both bending and tensile tests on monolithic nanoporous gold support the notion that rapid dynamic fracture. The dynamic fracture experiments yielded the first precise measurements of crack propagation velocity in nanoporous structures. For these tests conducted in bending, the compression stress limited the terminal velocity of the crack in air to ~ 7 m/s for 40 nm ligament size nanoporous gold. For bending tests in electrolyte a terminal velocity of ~ 40 m/s was observed. Tensile tests of nanoporous gold samples in air showed terminal velocities of ~ 160 m/s. The tensile stress and larger effective sample size allowed cracks to experience full “acceleration” and correspondingly higher terminal velocities. At 1.4 V, a monolayer of gold oxide is formed which reduces mobility of dislocation by pinning them at the surface or create surface barriers to impede dislocations from escaping. Samples tested at these potentials yielded terminal velocities ~ 500 m/s.

Some success has been achieved in both crack injection experiments and study of dynamic fracture of NPG samples. With respect to limitations of hand bending crack injection experiments, tensile loading using micrometer controlled vise is suggested for future experiments to allow cracks to experience full “acceleration”. One solution to the limitation in crack wall composition analysis is to use dual beam FIB to section samples for compositional GB analysis by scanning transmission electron

microscopy (STEM). In the study of dynamic fracture of NPG samples, galvanostatic dealloying of AgAu samples with dealloying current density below a few hundreds uA/cm$^2$ would be suggested to solve sample warping issues during dealloying of more than 1 cm long samples. Fracture stress and Young's modulus of monolithic NPG samples should be tested with micro tensile testing instrument both in air and electrolyte.

REFERENCES


1. H. Lechtman, Pre-Columbian Surface Metallurgy, *Scientific American* **250**, 56–63 (1984).

2. K.Sieradzki and R.C. Newman, Brittle Behavior of Ductile Metals during Stress-Corrosion Cracking, *Philosophical Magazine a-physics of Condensed Matter Structure Defects and Mechanical Properties* **51**, 95–132 (1985).

3. D. E. Williams, R. C. Newman, Q. Song, R. G. Kelly, Passivity breakdown and pitting corrosion of binary alloys, *Nature* **350**, 216–219 (1991).

4. H. W. Pickering, Characteris Feature of Alloy Polarization Curves, **23** (1983).

5. ASM handbook Alloy Phase Diagrams**3**, 2.25 (1992).

6. K.Sieradzki and R.C. Newman, Stress-corrosion cracking, *Journal of physics and chemistry of solids* **48**, 1101–1113 (1987).

7. K. Sieradzki, The Relationship Between Dealloying and Transgranular Stress-Corrosion Cracking of Cu-Zn and Cu-Al Alloys, *Journal of The Electrochemical Society* **134**, 1635 (1987).

8. K. Sieradzki et.al., Computer-Simulations of Corrosion-Selective Dissolution of Binary-Alloys, *Philosophical magazine. A, Physics of condensed matter. Defects and mechanical properties* **59**, 713–746 (1989).

9. D. Stauffer, *Introduction to Percolation Theory* (London,Taylor and Francis, 1985).

10. K. Wagner, S. R. Brankovic, N. Dimitrov, K. Sieradzki, Dealloying below the Critical Potential, *Journal of The Electrochemical Society* **144**, 3545 (1997).

11. K. Sieradzki, Curvature Effects in Alloy Dissolution, *Journal of The Electrochemical Society* **140**, 2868 (1993).

12. K. Sieradzki *et al.*, The Dealloying Critical Potential, *Journal of The Electrochemical Society* **149**, B370 (2002).

13. J. Rugolo, J. Erlebacher, K. Sieradzki, Length scales in alloy dissolution and measurement of absolute interfacial free energy., *Nature materials* **5**, 946–9 (2006).

14. W.W. Mullins, *Metal Surfaces: Structure, Energetics and Kinetics* (American Society of Metals, OH, 1963).

15. C. Wagner, Contribution to the Theory of Electropolishing, *Journal of The Electrochemical Society* **101**, 225 (1954).

16. H. W. Pickering, C. Wagner, Electrolytic Dissolution of Binary Alloys Containing a Noble Metal, *Journal of The Electrochemical Society* **114**, 698 (1967).

17. J. Erlebacher, M. J. Aziz, A. Karma, N. Dimitrov, K. Sieradzki, Evolution of nanoporosity in dealloying., *Nature* **410**, 450–3 (2001).

18. J. Erlebacher, https://jshare.johnshopkins.edu/jerleba1/public_html-/Technologies.htm.

19. B. K. Chakbavebty, Grain Size Distribution in Thin Films-1. Conservative Systems, **28**, 2401–2412 (1967).

20. Y. Ding, Y.-J. Kim, J. Erlebacher, Nanoporous Gold Leaf: “Ancient Technology”/Advanced Material, *Advanced Materials* **16**, 1897–1900 (2004).

21. R. G. Kelly, A. J. Frost, T. Shahrabi, R. C. Newman, Brittle Fracture of An AuAg Alloy Induced by a Surface Film, *Metallurgical Transacions a- Physical Metallurgy and Materials Science* **22A**, 531–541 (1991).

22. R. C. Newman, T. Shahrabi, K. Sieradzki, Film-Induced Cleavage of Alpha-Brass, *Scripta Metallurgica* **23**, 71–74 (1989).

23. C. Edeleanu and A.J. Forty, Some Observations on the Stress Corrosion Cracking of Brass and Similar Alloys, *Philosophical Magazine* **5**, 1029–1040 (1960).

24. T. B. Cassagne, W. F. Flanagan, B.D. Lichter, On the Mechasism of Chemically Embrittled Cu3Au Crystals, *Journal of Metals* **37**, A4 (1985).

25. M. Saito, G. S. Smith, R. C. Newman, Testing the Film-Induced Cleavage Model of Stress Corrosion Cracking, *Corrosion Science* **35**, 411–417 (1993).

26. J. S. Chen, T. M. Devine, M. Salmeron, Brittle Fracture of Cu-30 Au Induced by a Surface Layer, *Journal of The Electrochemical Society* **139**, 55–57 (1992).

27. J.S.Chen, M. Salmeron, T. M. Devine, Intergranular vs Transgranular Stress Corrosion Cracking of Cu 30-Au, *Corrosion Science* **34**, 2071–2097 (1993).

28. F. Friedersdorf, K. Sieradzki, Film-Induced Brittle Intergranular Cracking of Silver-Gold Alloys, *Corrosion* **52**, 331–336 (1996).

29. A. Barnes, N. a. Senior, R. C. Newman, Film-Induced Cleavage of Ag-Au Alloys, *Metallurgical and Materials Transactions A* **40**, 58–68 (2008).

30. H.L. Logan, Film-Rupture Mechanism of Stress Corrosion, *Journal of Research of the National Bureau of Standards* **48**, 99–105 (1952).

31. T. P. Hoar, J. M. West, Mechano-Chemical Anodic Dissolution, *Nature* **181**, 835 (1958).

32. R. N. Parkins, Predictive Approaches to Stress Corrosion Cracking Failure, *Corrosion Science* **20**, 19–21 (1980).

33. J. Yu, R. N. Parkins, Stress Corrosion Crack Propagation in a-Brass and Copper Exposed to Sodium Nitrite Solutions, **27**, 159–182 (1987).

34. R. C. Newman, Developments in the Slip-Dissolution Model of Stress-Corrosion Cracking, *Corrosion* **50**, 682–686 (1994).

35. E. N. Pugh, Progress toward Understanding the Stress-Corrosion Problem, *Corrosion* **41**, 517–526 (1985).

36. J. R. Galvele, A Stress Corrosion Cracking Mechanism Based on Surface Mobility, *Corrosion Science* **27**, 1–33 (1987).

37. J. R. Galvele, Surface Mobility Mechanism of Stress-Corrosion Cracking, *Corrosion* **35**, 419–434 (1993).

38. F. R. N. Nabarro, *Report of a Conference on the Strength of Solids* (London, 1948), p. 75.

39. K. Sieradzki, F. J. Friedersdorf, Notes on the Surface Mobility Mechanism of Stress-Corrosion Cracking, *Corrosion Science* **36**, 669–675 (1994).

40. J. E. Hack, S. P. Chen, D. J. Srolovitz, A kinetic criterion for quasi-brittle fracture, *Acta Metallurgica* **37**, 1957–1970 (1989).

41. T. Lin, A. G. Evans, R.O. Ritchie, Stochastic Modeling of the Independent Roles of Particle Size and Grain Size in Transgranular Cleavage Fracture, *Metallurgical Transacions* **18A**, 641–651 (1987).

42. L. Freund, J. Hutchinson, High Strain-Rate Crack Growth in Rate-Dependent Plastic Solids, *Journal of the Mechanics and Physics of Solids* **33**, 169–191 (1985).

43. J. Y. Zhang *et al.*, Length-scale-dependent Deformation and Fracture Behavior of Cu/X (X=Nb, Zr) Multilayers: The Constraining Effects of the Ductile Phase on the Brittle Phase, *Acta Materialia* **59**, 7368–7379 (2011).

44. A. K. Zurek, Brittle Cracks in Intrinsically Ductile Copper, *Scripta Metallurgica* **21**, 1619–1622 (1987).

45. S. A. J. Ricker R.E., Fink J.L., Harris J.S., Evidence for Film-induced Cleavage in Rhodium Plated Nickel, *Scripta Metallurgica* **26**, 1019–1023 (1992).

46. F. Yu *et al.*, Simultaneous excitation of propagating and localized surface plasmon resonance in nanoporous gold membranes., *Analytical chemistry* **78**, 7346–50 (2006).

47. C. Xu *et al.*, Low temperature CO oxidation over Unsupported Nanoporous Gold., *Journal of the American Chemical Society* **129**, 42–3 (2007).

48. J. Biener *et al.*, Surface-chemistry-driven Actuation in Nanoporous Gold., *Nature materials* **8**, 47–51 (2009).

49. R. Ling, K. Sieradzki, Ductile-Brittle Transition in Random Porous Au, *Physical Review Letters* **68**, 1168–1171 (1992).

50. J. Greer, W. Nix, Nanoscale Gold Pillars Strengthened through Dislocation Starvation, *Physical Review B* **73**, 1–6 (2006).

51. M. D. Uchic, D. M. Dimiduk, J. N. Florando, W. D. Nix, Sample Dimensions Influence Strength and Crystal Plasticity., *Science (New York, N.Y.)* **305**, 986–9 (2004).

52. C. a. Volkert, E. T. Lilleodden, Size Effects in the Deformation of Sub-Micron Au Columns, *Philosophical Magazine* **86**, 5567–5579 (2006).

53. J. Biener *et al.*, Size Effects on the Mechanical Behavior of Nanoporous Au., *Nano letters* **6**, 2379–82 (2006).

54. J. Biener, A. M. Hodge, A. V. Hamza, L. M. Hsiung, J. H. Satcher, Nanoporous Au: A High Yield Strength Material, *Journal of Applied Physics* **97**, 024301 (2005).

55. M. Hakamada, M. Mabuchi, Mechanical Strength of Nanoporous Gold Fabricated by Dealloying, *Scripta Materialia* **56**, 1003–1006 (2007).

56. A. M. Hodge *et al.*, Scaling Equation for Yield Strength of Nanoporous Open-cell Foams, *Acta Materialia* **55**, 1343–1349 (2007).

57. L. J. Gibson, M. F. Ashby, *Cellular Solids: Structure and Propertie* (Cambridge Univeristy Press, Cambridge, 1997).

58. C. A. Volkert, E. T. Lilleodden, D. Kramer, J. Weissmüller, Approaching the Theoretical Strength in Nanoporous Au, *Applied Physics Letters* **89**, 061920 (2006).

59. Y. Sun, T. J. Balk, A Multi-step Dealloying Method to Produce Nanoporous Gold with no Volume Change and Minimal Cracking, *Scripta Materialia* **58**, 727–730 (2008).

60. H. J. Jin *et al.*, Deforming Nanoporous Metal: Role of Lattice Coherency, *Acta Materialia* **57**, 2665–2672 (2009).

61. J. Biener, A. M. Hodge, A. V. Hamza, Microscopic Failure Behavior of Nanoporous Gold, *Applied Physics Letters* **87**, 121908 (2005).

62. B. Kahng, G. G. Batrouni, S. Redner, L. . D. Arcangelis, H. J. Herrmann, Electrical Breakdown in a Fuse Network with Random, Continuously Distributed Breaking Strengths.*Physical review. B, Condensed matter* **37**, 7625–7637 (1988).

63. D. Lee *et al.*, Microfabrication and Mechanical Properties of Nanoporous Gold at the Nanoscale, *Scripta Materialia* **56**, 437–440 (2007).

64. D. Lee *et al.*, Plastic Deformation in Nanoscale Gold Single Crystals and Open-celled Nanoporous Gold, *Modelling and Simulation in Materials Science and Engineering* **15**, S181–S192 (2007).

65. P. A. Rehbinder, E. D. Shchukin, Surface Phenomena in Solids During Deformation and Fracture Process, *Progress in Surface Science* **3**, 97–188 (1972).

66. H. Jin, J. Weissmüller, A Material with Electrically Tunable Strength and Flow Stress., *Science (New York, N.Y.)* **332**, 1179–82 (2011).

67. K. Sieradzki, Potential Solutions for Creating Responsive Materials., *Science* **332**, 1158–9 (2011).

68. J. Weissmüller, R. C. Newman, H. Jin, A. M. Hodge, J. W. Kysar, Nanoporous Metals by Alloy Corrosion : Formation and Mechanical Properties, **34**, 577–586 (2009).

69. L.B. Freund, *Dynamic Fracture Mechanics Cambridge Monographs on Mechanics and Applied Mathematics* (Cambridge Univeristy Press, New Yourk, 1990).

70. G. H.J., A Theory of Local Limiting Speed in Dynamic Fracture, *Journal of the Mechanics and Physics of Solids* **44**, 1453–1474 (1996).

71. T. Goldman, A. Livne, J. Fineberg, Acquisition of Inertia by a Moving Crack, *Physical Review Letters* **104**, 5–8 (2010).

72. J. D. Eshelby, The Elastic Field of A Crack Extending Non-Uniformly Under General Anti-Plane Loading, *Journal of the Mechanics and Physics of Solids* **17**, 177–199 (1969).

73. L. B. Freund, A. J. Rosakis, The Structure of the Near-tip Field During Transient Elastodynamic Crack Growth, *Journal of the Mechanics and Physics of Solids* **40**, 699–719 (1997).

74. N. F. Mott, No Title, *Engineering* **165** (1948).

75. D. K. Roberts, A. A. Wells, No Title, *Engineering* **178**, 820 (1954).

76. L. B. Freund, Crack Propagation In an Elastic Solid Subjected to General Loading-I .Constant Rate of Extension, *Journal of the Mechanics and Physics of Solids* **20**, 129–140 (1972).

77. L. B. Freund, Crack Propagation in an Elastic Solid Subjected to General Loading-II. Non-uniform Rate of Extension, *Journal of the Mechanics and Physics of Solids* **20**, 141–152 (1972).

78. L. B. Freund, Crack Propagation in an Elastic Solid Subjected to General Loading-III, Stress Wave Loading, *Journal of the Mechanics and Physics of Solids* **21**, 47–61 (1973).

79. T. Kobayashi, J. W. Dally, Fast Fracture and Crack Arrest, *The American Society of Testing and Materials* , 257 (1977).

80. J. Snyder, K. Livi, J. Erlebacher, Dealloying Silver/Gold Alloys in Neutral Silver Nitrate Solution: Porosity Evolution, Surface Composition, and Surface Oxides, *Journal of The Electrochemical Society* **155**, C464 (2008).

81. N. Yao, *Focused Ion Beam Systems: Basics and Applications.* (Cambridge Univeristy Press, 2007).

82. M. Hayles, *Nova nanolab user's manual* (FEI Company, ed. 3rd, 2004).

83. O. Okman, D. Y. Lee, J. W. Kysar, Fabrication of crack-free nanoporous gold blanket thin films by potentiostatic dealloying, *Scripta Materialia* **63**, 1005–1008 (2010).

84. L. D. Burke, L. C. Nagle, Anomalous electrochemical behaviour of palladium in aqueous solution, *Journal of Electroanalytical Chemistry* **461**, 52–64 (1999).

85. J. D. Fritz, B. W. Parks, P. H.W., Stress Corrosion Cracking of Cu-18%Au in 1N Na2SO4-0.01N H2SO4, *Scripta Metallurgica* **22**, 1063–1068 (1988).

86. S. Lozano-Perez, *A Guide on FIB Preparation of Samples Containing Stress Corrosion Crack tips for TEM and Atom-probe Analysis* (Micron, 2009), pp. 320–328.

87. L. B. Freund, G. Herrmann, Dynamic Fracture of a Beam or Plate in Plane Bending, 112–116 (1976).

88. G. Herrmann, Effect of Axial Force on Dynamic Fracture of a Beam or Plate in, 647–651 (1977).

89. J. Snyder, P. Asanithi, A. Dalton, J. Erlebacher, Stabilized Nanoporous Metals by Dealloying Ternary Alloy Precursors, *Advanced Materials* **20**, 4883–4886 (2008).

# APPENDIX A

## PRELIMINARY RESULTS OF TENSILE TEST ON NPAUPT IN AIR

$Ag_{70}Au_{25}Pt_5$ alloy was dealloyed to produce NP AuPt using the same methods as for the preparation of crack-free NPG in 1M $HNO_3$ for tensile tests in air. First, the polarization behavior of $Ag_{70}Au_{25}Pt_5$ alloy in 1M $HNO_3$ was examined by potential dynamic scan to determine appropriate dealloying potential. The specimens of 2 mm×2.5 mm×254 um were held in between two small quartz plates and annealed in Ar-filled quartz tube for 48 hours. The samples were prepared in the same way for potentiodynamic scans as the crack injection experiment. The dynamic scan was run at a scan rate of 5 mV/s in a standard three-electrode cell with platinum wire as counter electrode and mercury/mercurous sulfate as reference electrode. The obtained polarization curve is shown in Figure A.1, which shows critical potential with current density of 1 $mA/cm^2$ at around 1.38 V (NHE).

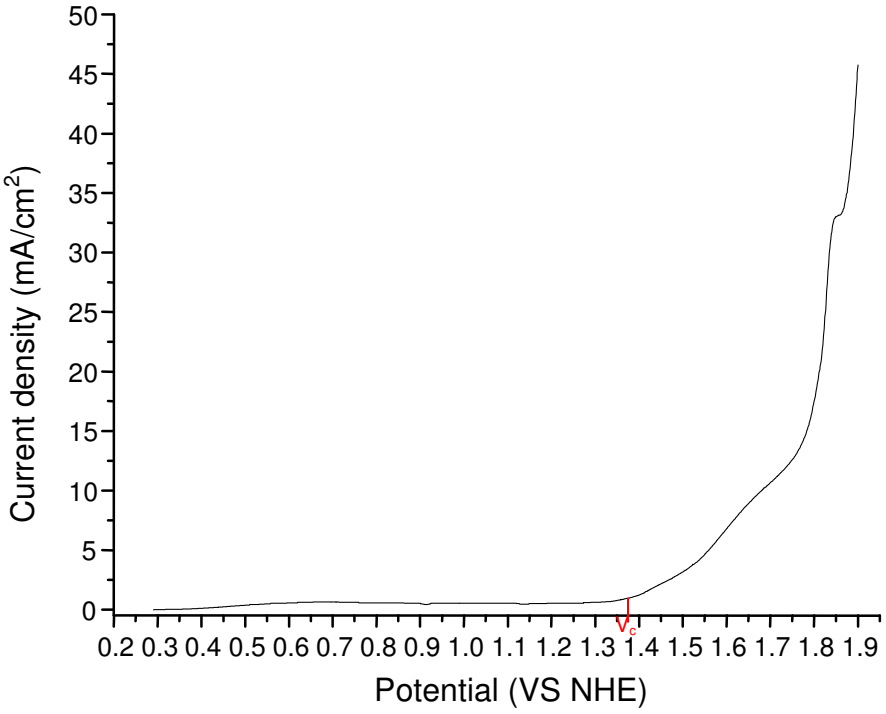


Figure A.1. Potential dynamic scan of $Ag_{70}Au_{25}Pt_5$ in 1M $HNO_3$. $V_c$ -the critical potential of the sample dealloyed in 1M$HNO_3$. Here we use the current density of 1 mA/cm$^2$ to define Vc. Scan rate was 5 mV/s.

Pretreatment of this alloy sample, size and location of EDM notch on test samples and method to polish and dealloy samples were same as that for tensile tests of NPG in air. Three potentials were tried to fabricate crack free NPAuPt, 1.38 V, 1.29 V and 1.34 V vs NHE. At 1.38 V, obvious cracks were observed along grain boundaries and dealloyed pore size was around 5 nm (as shown in Figure A.2).

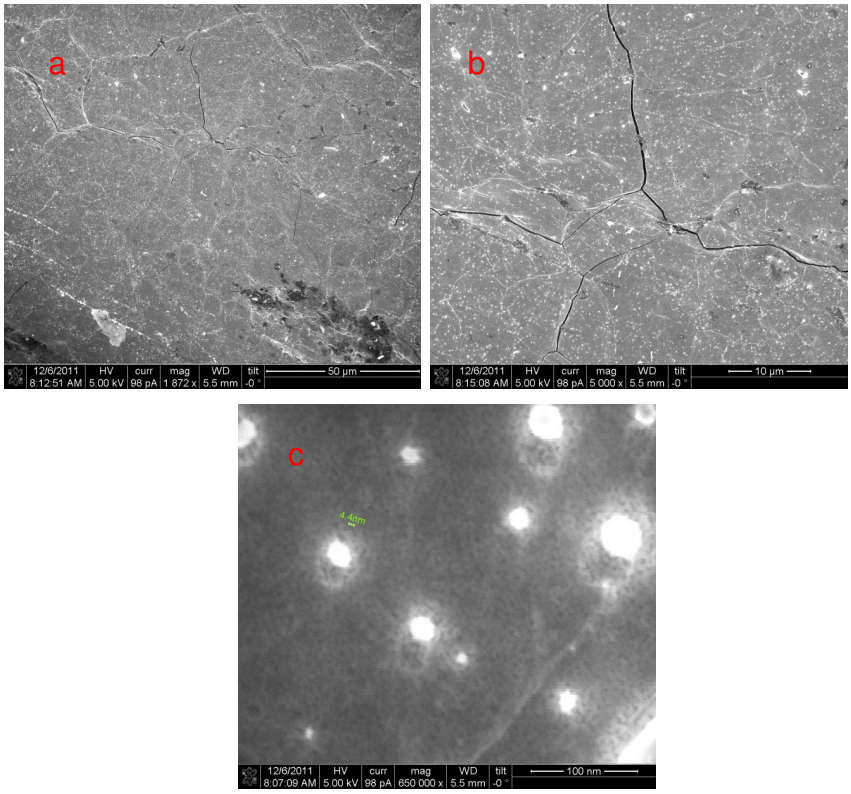


Figure A.2. Top surface of NPAuPt sample dealloyed at 1.38 V (NHE) for around 52 hours in 1M HNO3 and aged in air for 24 hours a & b: obvious cracks were observed along grain boundaries. c: Nanoporous morphology of the NPAuPt sample after staying in air for 24 hours, showing stable ligament size around 5 nm.

At 1.29 V, dealloying current quickly dropped below 10 uA and stayed at such a low current for a long time. In the ternary alloy, small amounts of Pt will accumulate on the surface, particularly at step edges. Much slower diffusion rate of Pt at this lower potential suppresses dealloying and therefore results in an increased current decay. To increase the dealloying rate to a reasonable value, 1.34 V was tried for 105 hours of dealloying time. The initial dealloying current density was around 0.6 mA/cm$^2$ and

gradually dropped below 0.5 mA/cm$^2$. As shown in Figure A.3, the degree and amount of cracks were obviously reduced compared to the sample dealloyed at 1.38 V. However there are still small cracks observed along some grain boundaries on dealloyed surface.

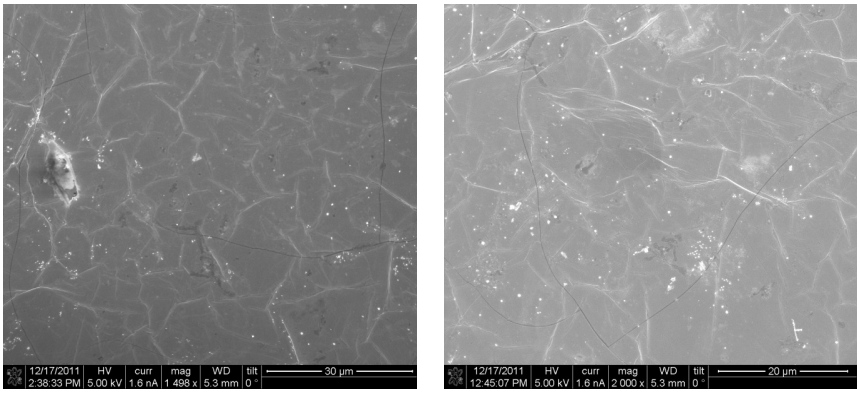


Figure A.3. Top surface of NPAuPt sample dealloyed at 1.34 V vs NHE for around 105 hours in 1M $HNO_3$ and aged in air for 24 hours. Cracks were still observed along some grain boundaries.

Two tensile tests in air were conducted with NPAuPt samples dealloyed at 1.34 V and dried in air after 24 hours. Figure A.4 shows cracked top surface and fracture surface of test samples after tensile test. During the tests, there was no obvious crack initiation from the notch and there was non-planar crack (Figure A.4 a). The fracture surface shows clear grains and indicates complete intergranular fracture of the sample in bending.

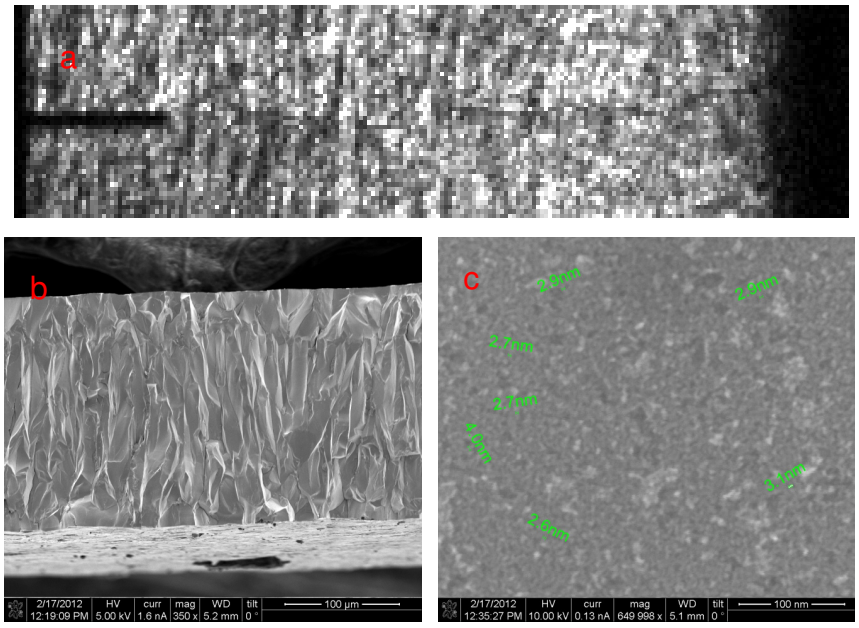


Figure A.4. a Top surface of test NPAuPt sample showing non-linear crack path after tensile tests in air. b. Fracture surface of NPAuPt after test, showing clear intergranular fracture mode. c. High magnification SEM image of fracture surface of NPAuPt, indicating around 3-4nm ligament size.

Tensile test results indicated that several of the as-dealloyed cracks in these samples may have penetrated across the sample.

# APPENDIX B

# FRACTURE STRESS MEASUREMENT DURING TENSILE TEST IN AIR

Mechanical tensile tests using micro-force testing systems were conducted on dry NPG specimens to precisely evaluate stress required to fracture NPG without and with notches. A Tytron 250 MTS testing system was employed for this set of experiments. This instrument provides low loads ranging from 0.001 N to 250 N and gives reliable and highly accurate “micro-force” testing with an advanced linear servomotor and high-speed digital control technology. It is composed of a load unit, FlexTest controller, amplifier and test software. In our tests, the load cell was 10N cell with resolution of 0.001 N.

Both 12 um thick Ag-30at%Au alloy foil and NPG samples were tested by micro-force testing systems. Loading stages on Tytron 250 were cleaned with acetone before tests. Ag-30at%Au alloy sample was 1.85 cm (length) ×0.55 cm (width) × 12 um (thickness). The alloy samples were taped on loading stages and stage gap was left with 1.3 cm. The samples were loaded under displacement control at a rate of 2 um/s. The alloy sample did not break into two parts as the black tape peeled off as the loading force reached around 4.9 N. NPG sample without a EDM notch was 1.5 cm (length) × 2 mm (width) ×127 um (thickness) and sample with EDM notch was 1.8 cm (length)× 4 mm( width) ×127 um (thickness) were tested. These alloy specimens were pretreated, dealloyed and post treated as described in section 2.2.1. Dried crack-free monolithic NPG samples were carefully transferred to the loading stage of the Tytron. For NPG samples without a notch, a1 cm gap between loading plates was left,

while for notched NPG, a 1.1 cm gap was left. Both ends of NPG were epoxy glued. Load was not applied until the epoxy hardened (~30 minutes). The samples were loaded under displacement control at a rate of 0.02 um/s. Both NPG specimens fractured in a brittle mode. The specimen without a notch fractured at the region within stage gap and specimen with notch fractured right at the notch. The stress-strain curve was derived from the test data and the fracture stress was determined. Young's modulus of NPG samples was derived by fitting the initial part of curve to a straight line.

The obtained stress-strain curve for Ag--30at%Au alloy foil is plotted as below in Figure B.1. Although carbon black tape peeled off before the alloy foil was fractured, Young's modulus can still be derived from initial part of stress-strain curve. Linear fitting of initial part of stress-strain curve yields relationship of y=5050x-1.07 for linear line in red shown in Figure B.1. The slope of the line corresponds to the young's modulus of Ag-30at%Au, which is around 5.05 GPa. This value is much lower than Young's modulus of silver (83 GPa) or gold (79 GPa). Accuracy of displacement measurement with the Tytron system is likely the cause for the large deviation of our measurement.

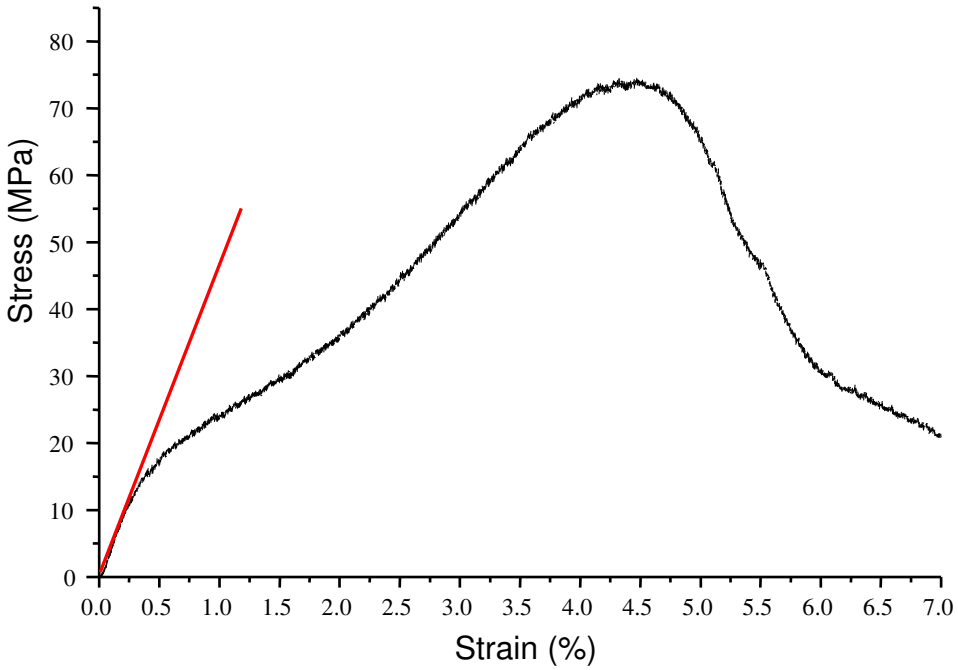


Figure B.1. Stress-strain curve of 12 um thick Ag-30at%Au foils without notch. The fitted red line indicating Young's modulus of NPG sample around 5.05 GPa.

During tensile tests on NPG samples, both types of samples fractured in a brittle mode. NPG samples without notch fractured within two loading stages and sample with notch fractured right at the EDM notch. Fracture surfaces for both kinds of samples are flat and transgranular. Displacement of sample during testing was obtained by simply from the cross-head position. The engineering strain then can be calculated by dividing displacement with sample free moving length without epoxy glue. For NPG without notch, the sample free moving length is 1cm. For NPG with notch, it is 1.1cm. The stress-strain behavior of NPG samples with and without notch is plotted in Figure 3.47. In this figure, the stress-strain

curve for NPG sample without notch is almost completely overlapped by curve for sample without notch. Both curves show linear within 0.2% strain and NPG sample with notch fractured before 0.2% strain. Linear fitting for this range of data gives relationship of y=908.88x+0.072 and linear line in red shown in Figure3.38. The slope of the line corresponds to the young's modulus of NPG samples with around 40 nm ligament size, which is around 0.91 GPa. The fracture stress for NPG sample without notch is around 11.51 MPa and for NPG sample with notch around 2.16MPa. As have been confirmed with tensile tests of Ag-30at%Au foils, the big deviation of young's modulus and fracture stress obtained in our experiment is mainly because of less precise strain measurement. More samples should be tested in air with more precise strain measurement system. The fracture stress of NPG in electrolyte under potential control can also be measured with sample loaded in the Teflon cell used for tensile tests in electrolyte.

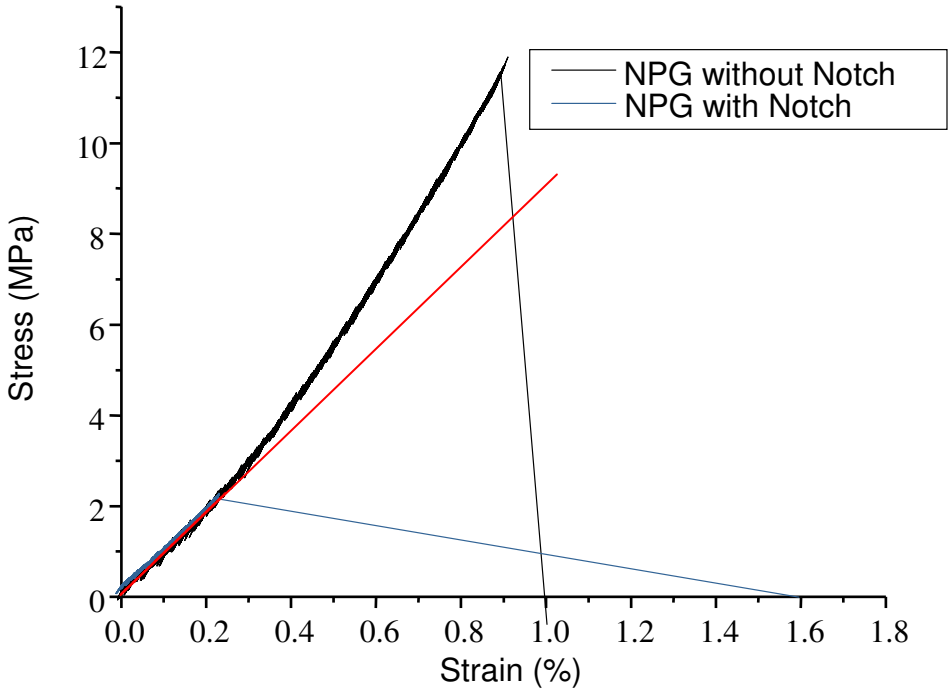


Figure B.2. Stress-strain curve of NPG samples with and without notch. NPG samples were dried in air for 24hours after being dealloyed in 1M $HNO_3$. Black curve refers to sample without notch and fracture stress of 11.51 MPa was obtained; Blue one refers to sample with notch and fracture stress of 2.16 MPa obtained. The fitted red line indicating young's modulus of NPG sample around 0.91GPa.